STUDY OF PHASE IN FERROMAGNETIC SPIN-TRIPLET JOSEPHSON JUNCTIONS

By

Yixing Wang

A DISSERTATION

Submitted to
Michigan State University
in partial fulfillment of the requirements
for the degree of

Physics - Doctor of Philosophy

2013

ABSTRACT

STUDY OF PHASE IN FERROMAGNETIC SPIN-TRIPLET JOSEPHSON JUNCTIONS

By

Yixing Wang

In conventional superconductors, the opposite-spin electrons are bound together to form Cooper pairs (spin-singlet), whereas the electrons in magnetic materials align parallel to each other in the same spin band. When a superconductor is placed in contact with a ferromagnet, researchers have learned that the two electrons from the spin-singlet Cooper pair enter different spin bands and rapidly lose phase coherence. The coherence length for the spin-singlet correlation in ferromagnetic materials is around a few . On the other hand, some theorists proposed that one could obtain long-ranged spin-triplet correlation in some well engineered superconductor/ferromagnet (S/F) hybrid structures, where the correlation length could be around a few .

Indeed, during the last few years, several groups around the world have confirmed the long-range spin-triplet correlation in different systems, including our group. In our case, we made Josephson junctions containing a ferromagnetic multilayer, which can carry spin-triplet supercurrent under certain conditions. At the same time, theorists predicted that the phase of these junctions can be controlled by the magnetizations of the magnetic layers. They predicted the existence of and junctions. Since our large-area junctions contain multiple domains, we expected to have a random distribution of 0 or coupling regions across the junction surface, whereas magnetized samples should have uniquely pi coupling everywhere according to theories. Indeed we observed the enhancement of the critical current of our Josephson junctions after magnetizing our samples, which indirectly indicated the mixture

of 0 and coupling in the virgin state. According to a random walk model, we would expect that the critical current in the as-grown state would be proportional to the square root of the area of the junction, whereas in magnetized samples it should be proportional to the area. We have measured the area dependence of the critical current in such junctions, and confirm that the critical current scales linearly with area in magnetized junctions. For as-grown (multi-domain) samples, the results are mixed. Samples grown on a thick Nb base exhibit critical currents that scale sub-linearly with area, while samples grown on a smoother Nb/Al multilayer base exhibit critical currents that scale linearly with area. The latter results are consistent with a theoretical picture due to Zyuzin and Spivak that predicts that the as-grown samples should have global coupling. We even attempted to test the Zyuzin-Spivak prediction by making spin-triplet superconducting quantum interference devices (SQUIDs). If the SQUID is made of the two -state junctions, we would expect the flux periodicity to be half compared with traditional SQUIDs. Yet, we have not observed any half quantum flux periodicity in our Nb/Al multilayer based SQUID. Further research will be needed to solve this mystery.Special comment: The integrity of the dissertation has been damaged during the submission to the graduate school by the Confer, Erica. I would not take any responsibility for this.

ACKNOWLEDGMENTS

First and foremost, I thank my dissertation adviser, Professor Norman O. Birge for many years of professional guidance. I respect your research integrity and your thirst for knowledge. Sometimes, I asked exactly the same questions many times due to my negligence in taking notes. Yet you showed me crazy patience. I also would like to thank Professor William P. Pratt Jr. for the invaluable input from you. I am so amazed by your extraordinary experimental abilities that I wish I have a small portion of your talent and dexterity.

Also, I would like to thank Professor Pawel Danielewicz, Professor Mark Dykman, Professor Jim Linnemann and Professor Stuart Tessmer for being my committee members. I still remember the encouragement and suggestions you gave to me whenever we bumped into each other.

Very special thanks go to Dr. Reza Loloee and Dr. Baokang Bi, who taught me hands-on operations on all kinds of equipment for my sample fabrication. I appreciate your dedication helping me and many other graduates in the basement. I remember that I tried to fill a liquid Dewar by opening the gas outlet side valve. Dr. Loloee gave me a hint and let me figure it out. I also remember that Dr. Bi gave me the simplest yet effective advice to determine whether one problem was caused by melting of the PR1813. These kinds of examples are numerous.

I would like to thank graduate secretary Debbie Barratt and CMP secretary Cathy Cords for taking time to figure out lots of paperwork for me. Also I would like to thank Tom Palazzolo, Thomas Hudson and the other members of the machine shop. Tom helped me overcome the fear of machining. Thomas spent time in double checking my designs over different subjects. I also like to thank Mr. Barry Tigner, who often gave me a hand on electronics problem.

Our group members also deserve thanks. Eric Gingrich, Trupti Khaire, Mazin Khasawneh and William Martinez, the time we spent together is always memorable. I always feel excited for Trupti and Mazin to make the big discovery. The trip to the bar I took with Eric Gingrich, William Martinez and Sean Wagner in Baltimore was really a big fun. Kevin Barry, Kurt Boden, Alex Cramer, Simon Diesch, Joseph Glick, Carolin Klose, Matthias Muenks, Bethany Niedzielski, Patrick Quarterman and Kevin Werner, I also enjoyed being accompanied by you. I was very happy that Bethany mastered the majority of things I was working on so quickly and smoothly. Also thank to Rakhi Acharyya, Michael Crosser, H.Nguyen and Josh Veazey.

Last but not least, I owe my family a big thank you! You always stand behind me.

TABLE OF CONTENTS

LIST OF TABLES

LIST OF FIGURES

Chapter 1

Introduction

1.1 Background and motivation

It is well known to people studying traditional metallic superconductors that the current in these superconductors is carried by Cooper pairs [19, 5]. The Cooper pairs are made of two s-wave electrons with opposite spins. According to the standard fermi-statistics, the Cooper pairs obey the fermionic antisymmetry because they have even orbital angular momentum(l =0) and have odd spin correlations(spin-singlet). On the other hand the spins of electrons in the majority band or minority of a ferromagnet tend to align with each other in the same direction due to the exchange field. Due to this incompatibility, people have not been able to discover any bulk compounds showing the coexistence of the spin-singlet superconductivity with strong ferromagnetism. However, people have been working with nano-structured multilayered superconductor/ferromagnet (S/F) systems for a very long time. Researchers studied the proximity effects between superconductivity and ferromagnetic order. And they found out that the spin-singlet pair correlations near the superconductor-ferromagnet interface are very different from the the spin-singlet pair correlations near the superconductor-normal interface [14, 15, 16]. The most obvious signature is that the superconducting coherence length in the ferromagnet is very short, around a few nm compared with superconductor/nonmagnetic normal metal system (S/N) [47, 21]. However several successful experiments came out during last few years and proved the existence of the long-ranged spin-triplet correlation in some S/F systems with magnetic inhomogeneity [34, 57, 62, 2]. It was truly amazing that some theories already predicted this long-ranged spin-triplet correlation more than 10 years ago [8, 9, 36]. The results of our Josephson junctions with a ferromagnetic multilayer sandwiched between two traditional superconductors showed several orders of magnitude higher critical current density compared with spin-singlet S/F/S junctions [34].

On the other hand, the critical current density is just the amplitude side of the story of the long-ranged spin-triplet correlation (LRSTC). There is also the phase side story of the LRSTC. The theories also predicted that the phase of these spin-triplet Josephson junctions are determined by the relative orientation of magnetizations of different magnetic layers [31, 9, 68]. And we must say that the phase is not unique to the spin-triplet Josephson junctions, because people working with traditional S/F/S Josephson junctions also observed the oscillatory nature of the short ranged spin-singlet correlation [54, 12, 58, 52, 55, 56]. These researchers observed the Josephson critical current oscillation in their system due to the oscillatory proximity effect. These spin-singlet ferromagnetic Josephson junctions show 0-state and π-state depending on the thickness of the magnetic layer [38]. Sometimes, the oscillation happens on a length scale around a few angstroms for a strong ferromagnet like Co [55], which presents a technical difficulty in controlling it. And at the same time, we also lack the means to control the phase of these traditional ferromagnetic junctions, after the device has been fabricated. However, the phase for spin-triplet Josephson junctions can be controlled by tuning the directions of the magnetizations of different magnetic layers with an external magnetic field. Our multilayered ferromagnetic Josephson junctions are really very good candidates for this phase control.

Since our junction size is much bigger than the magnetic domain size, we expect that 0 and π subjunctions randomly distribute across our junctions in the as-grown state. After magnetizing the samples, on the other other hand, we would expect that a single π-state would dominate across the whole junction according to the theories. Our work is dedicated to unveiling the phase side of the story of the long-ranged spin-triplet correlation.

1.2 Structure of the dissertation

The dissertation is organized as follows: In chapter 2, I will give an introduction to some aspects of ferromagnetism and superconductivity. Also a description of short-ranged and long-range proximity effects are given at the end of the chapter. The mechanisms to generate and to observe long-range spin-triplet correlation in S/F multilayer structure are presented. In chapter 3, the theory of the Josephson effect will be discussed, including the I-V characteristics of Josephson junctions and their response to an applied magnetic field. In chapter 4, I will give a brief discussion of the sample fabrication process and measurement setup. In chapter 5, I will review some previous results of ours and others to gain some idea about the 0 and π phase concept. In chapter 6, the most important results from our study of the area dependence of the critical current of our spin-triplet Josephson junctions will be discussed. Possible mechanisms for different area scaling are also proposed. In chapter 7, in order to test the possibility of the existence of the $\pi/2$ coupling Josephson junction, I will show our first attempt to measure a long-ranged spin-triplet SQUID. However we did not observe the half quantum-flux periodicity predicted for a SQUID containing $\pi/2$ junctions. In chapter 8, I will give a conclusion and future directions.

Chapter 2

Ferromagnetism and Superconductivity

When people talk about superconductors and ferromagnets, the first image might be a superconducting ferromagnetic levitation train. The working mechanism is based on the repulsion force between a superconductor and a permanent magnet. This gives us some idea that superconductors do not like magnetic fields, because the strong magnetic field will try to force the opposite spins of Cooper pairs into the same direction. And at the same time, it is also well known that ferromagnetism is incompatible with superconductivity; ferromagnetism strongly suppresses superconductivity. In superconductor/ferromagnet bilayered structures this suppression is caused mainly by the exchange interaction, which we can see in the following sections. This is the driving force of my work to understand superconductor-ferromagnet multilayered systems. In this chapter, we will learn the key aspects of superconductivity and ferromagnetism, and obtain the raw idea of the interplay between the two.

2.1 Ferromagnetism

2.1.1 Origin of Ferromagnetism

Humans rely on more and more magnetic materials from macroscopic applications to microscopic applications. These applications include electrical power generators and transformers, electric tooth brushes, hard-disks, Giant Magnetoresistance (GMR) readers, etc. Even though magnetic materials are involved heavily in our daily life, the nature of ferromagnetism is very complicated and governed by quantum physics, which is far beyond the scope of this section. Here we try to briefly explain the basic concept of ferromagnetism. Even though there were some researchers trying to explore the existence of magnetic monopoles from time to time in the past, it is a fact that there is no evidence for the existence of magnetic monopoles. Instead an ordered alignment of the atomic magnetic moments is the origin of the macroscopic magnetic properties of materials. There are two physical sources of the atomic magnetic moments, which correspond to orbital motion around the nucleus and spin angular momentum, as shown by Equation 2.1.

$$\overrightarrow{M} = -g\frac{e}{2m}\overrightarrow{J} \tag{2.1}$$

$\overrightarrow{J}$ could be the orbit momentum or spin momentum. The factor g is called the “gyromagnetic ratio”, correspondingly g=1 for orbital motion and g=2 for spin for a single electron. However, the orbital magnetic moment contribution is usually very small. And the quantum And Spin magnetic moments may be only in an “up” direction or in an antiparallel “down” direction.

In order to explain the spontaneous magnetization of ferromagnetic materials such as iron, cobalt, nickel, etc, Heisenberg [29] in 1928 proposed an exchange force model of quantum mechanical nature. According to his model, the potential energy between two atoms having spins Si and Sj is governed by

$$w_{ij} = -2J_{ex}\overrightarrow{Si} * \overrightarrow{Sj} \tag{2.2}$$

where J_{ex} is the exchange integral. If $J_{ex} > 0$, $\overrightarrow{Si}$ and $\overrightarrow{Sj}$ tend to align parallel to satisfy the least energy requirement; if $J_{ex} < 0$, the stable state corresponds to the anti-parallel spin configuration.The ground state for $J_{ex} > 0$ case corresponds to the ferromagnetic state, where all the spins align parallel in the same direction.

Stoner [64] and Slater [59] further proposed the band theory of ferromagnetism. On the basis of the knowledge of the density of states in the 3d shell and the exchange interaction acting between 3d electrons, they suggested that there could be slightly more electrons in the spin-up band compared to the spin-down band. These extra spin-up electrons contribute to the net magnetic moment.

2.1.2 Magnetic Domains

Most ferromagnetic materials at a temperature below the Curie temperature T_c are composed of small-volume regions in which all magnetic moments align in the same direction, as illustrated in Fig. 2.1. Weiss [76] in 1907 predicted the presence of the ferromagnetic domain structure. One piece of indirect evidence for domains is that we could demagnetize ferromagnetic samples by annealing at temperature higher than T_c or by an alternating magnetic field. After demagnetization, magnetic moments of domains could randomly point in any direction which results in a zero net magnetization of the whole sample. Another piece of

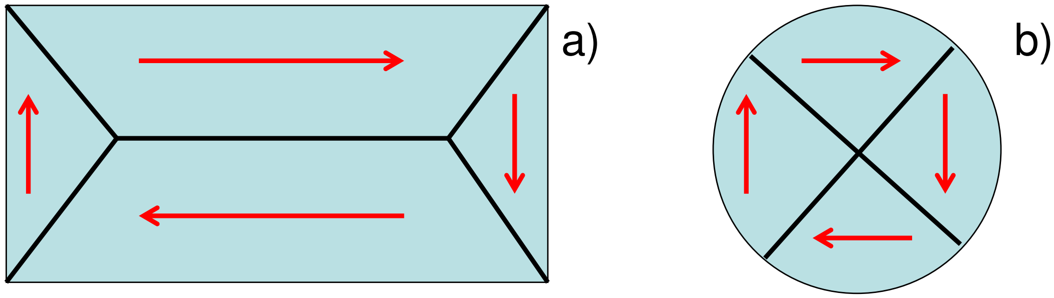

Figure 2.1: In (a) and (b),we show the schematic depiction of domains in ferromagnetic materials; arrows represent magnetic moments. The direction of magnetic moments varies from one domain to another.“For interpretation of the references to color in this and all other figures, the reader is referred to the electronic version of this dissertation.”

indirect evidence is the shape of the hysteresis loop as shown in Fig. 5.11.b). Magnetization M and field intensity H are typically not proportional for ferro-magnets. If the material is initially demagnetized, then M varies as a function of H as shown in Fig. 2.2 during the initial magnetization process. The curve begins at the origin, and as H is increased, M begins to increase slowly, then more rapidly, finally leveling off and becoming independent of H. This maximum value of M is the saturation magnetization.

Domain structures corresponding to any real magnetization process are much more complicated compared to the schematic brain-game shown in Fig. 2.2. But it does not mean that we do not have any clue about what is the driving force of domain evolution. It is related to the energy stored in the magnetic materials. For homogeneous ferromagnetic materials, several different types of energy contribute to the total energy, as listed below.

1. Crystal anisotropy energy which generally possesses the crystal symmetry of the material. For example, Uniaxial anisotropy is the simplest form of crystal anisotropy.

2. Inverse Magnetostrictive energy which shows up when a stress force is applied to a ferromagnetic body. Basically this is just the opposite effect of magnetostriction, wherein the shape of the a ferromagnetic sample changes during the process of magnetization.

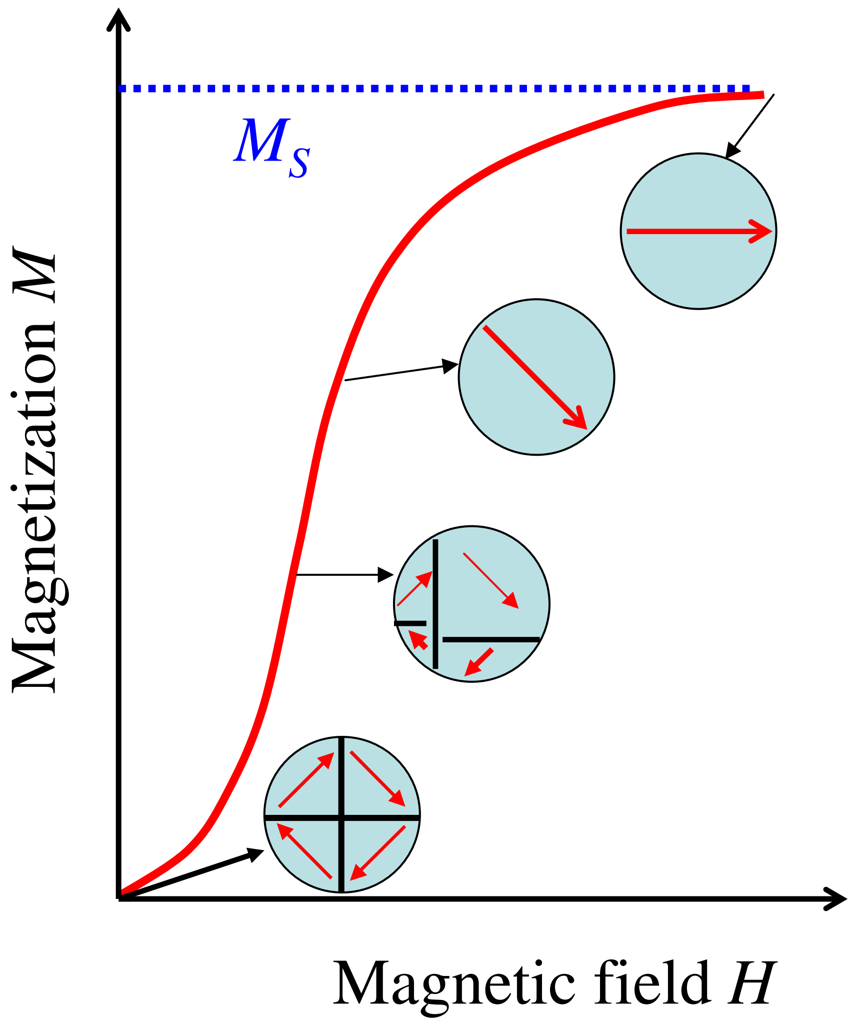

Figure 2.2: Schematic depiction of initial magnetization process; the red arrows represent magnetic moments.

3. Magnetostatic energy which mainly concerns the energy stored in the magnetic field generated by magnetization. This energy is most shape-dependent.

4. Zeeman energy which counts the effects exerted by the external magnetic field on ferromagnetic samples.

5. Domain-wall energy which basically lowers the exchange energy between different domains pointing in different directions. Within a domain wall, the direction of spins changes gradually from one domain to another in order to avoid an atomic-scale sharp boundary.

In inhomogeneous magnetic samples, the size and shape of domains are also affected by the inhomogeneity of the materials, such as voids, inclusions, precipitations, fluctuations in alloy compositions, crystal boundaries, internal stress, etc.

2.2 Superconductivity

Along the path human beings explore the world, physicists were and are always dedicated to pushing the boundaries of their view. One of these boundaries was the lowest resistivity of metals when being cooled down. Before 1911, physicists had been familiar with the idea that the resistance of metals would decrease when they were cooled down. But what would they finally obtain when temperature approached towards 0K? No one could nail it down with 100% certainty at that time. With the technical breakthrough in liquefying Helium, extremely low temperature experiments came to reality in 1908. Three years later, Heike Kamerlingh Onnes [37] discovered the superconducting state of mercury at liquid helium temperature. The most stunning part of the discovery was not just that the resistance of mercury came to zero, but that the disappearance of the resistance was so abrupt at about 4K.

As the name of “superconductor” indicates, various abnormal properties of the superconducting state intrigued many physicists to seek the origin of superconductivity. These properties include zero resistance, electronic specific heat, isotope effect, Meissner effect, etc. Even with clues from these unique superconducting properties, it still took theorists a long time to figure out the microscopic theory of superconductivity.

The first crucial attempt towards a microscopic theory of superconductivity was proposed by Leon Cooper [19], who showed that two electrons added above the Fermi level could form a bound state with energy less that $2\epsilon_f$ if there is an attraction between them. The important characteristic of Cooper pairs is that the two electrons in one pair have opposite spin and momenta, which corresponds to the spin-singlet state. Assisted with the Uncertainty Principle, the size of Cooper pairs can also be estimated to be around $10^{-4}cm$. Compared with the crystal lattice dimension, the space enclosed by one Cooper pair is so humongous that there are countless electrons inside. In other words, there definitely exist other Cooper pairs within the space of one Cooper pair. The superconducting state must be a multi-body problem.

After taking Cooper pairs into account, John Bardeen, Leon Cooper, and Robert Schrieffer [5]successfully developed the microscopic theory of superconductivity called BCS theory in 1957. They showed that the ground state of superconductivity takes the form

$$\Psi_{BCS} = \prod_k (u_k + v_k c^{\dagger}_{k,\uparrow} c^{\dagger}_{-k,\downarrow})|\phi_0\rangle \tag{2.3}$$

where $|\phi_0\rangle$ is the vacuum state. The creation operator $c^{\dagger}_{k,\uparrow}$ creates an electron of momentum

k and spin up $\uparrow$. Therefore we can see that $c^\dagger_{k,\uparrow}c^\dagger_{-k,\downarrow}$ creates one Cooper pair occupying the pair state $(k\uparrow,-k\downarrow)$. At the same time, $|v_k|^2$ shows the probability that the pair state $(k\uparrow,-k\downarrow)$ is occupied, and $|u_k|^2$ shows the probability that the pair state is unoccupied. Therefore, in our traditional superconductor, the current carriers are spin-singlet Cooper pairs.

2.3 Proximity effects

As we have learned from above, electrons in a ferromagnet (F) try to align their spins in the same direction, while paired electrons in Cooper pairs of a superconductor (S) have their spins in opposite directions. At the same time, it is well known that electrons in the normal metal (N) do not have any direction preference for their spins. Therefore, ferromagnets and superconductors are spin-ordered systems. On the other hand, the normal metal is a spin-disordered system.

So what will happen when we combine two different systems together? The most famous spin-valve system will jump into our mind, where people sandwich one normal metal thin film between two ferromagnetic leads. The spin information from one ferromagnetic layer of properly engineered F/N/F systems can be read out by the other F layer, which is analogous to the case of polarized optics. The logic behind this F/N/F structure is "ordered system"/"less ordered system"/ "ordered system". Following the same logic, we can construct the S-F-N triangle diagram as shown in Fig. 2.3. The other two nontrivial structures are S/N/S and S/F/S.

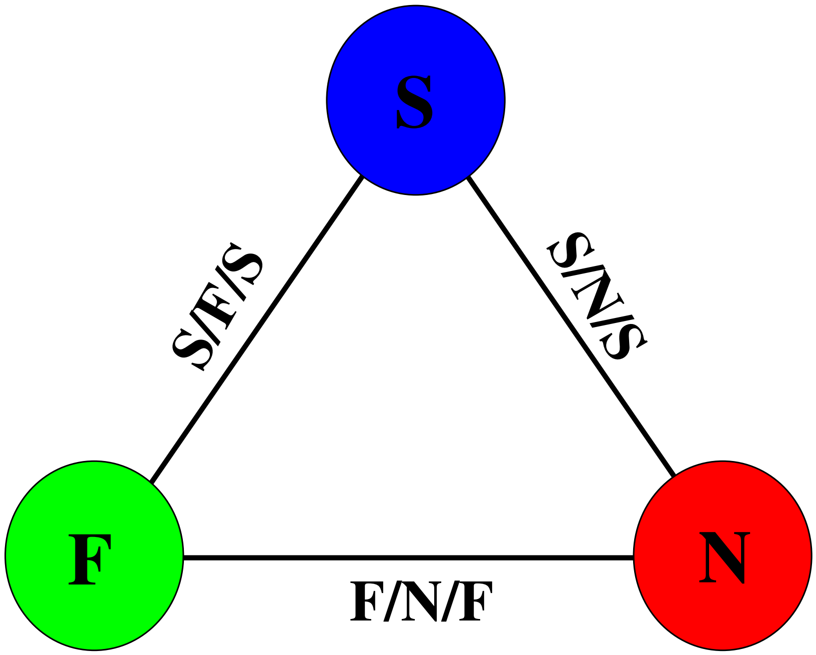

Figure 2.3: Superconductor-Ferromagnet-Normal metal triangle. Three nontrivial structures are shown here.

2.3.1 Traditional Proximity effects of S/N and S/F

So let us take a look at the case when one superconductor is placed next to a normal metal or a ferromagnet. The Cooper pairs leaking from the superconductor side can induce superconducting-like properties in the normal metal or ferromagnet and this phenomenon is usually called the proximity effect. At the same time, the weakening effect of superconductivity due to the leakage of Cooper pairs is called inverse proximity effect.

The microscopic theory behind the proximity effect is called Andreev reflection. The Andreev reflection process provides the channel to convert single-electron states of a normal metal into Cooper pairs, when electrons with energy below the superconducting gap approach the S/N interface from the normal metal side. Imagine there is an electron (ϵ,k,$\uparrow$) approaching the S/N interface from the N-side, where ϵ is the energy measured with respect to the Fermi level. If $\epsilon < \Delta$, where Δ is the superconducting gap parameter, then the

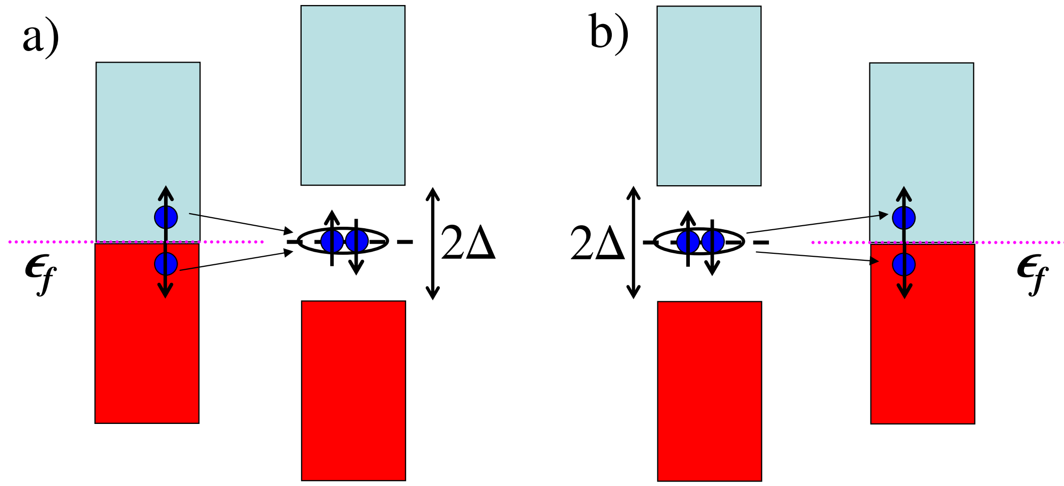

Figure 2.4: on energy level diagram, a) Andreev reflection process from normal metal to superconductor. b) Inverse Andreev reflection process from superconductor to normal metal.

electron can't be transferred into the superconductor because there are no single-particle states in S with $\epsilon < \Delta$. However if this electron can find another electron ($-\epsilon$,$-k$,$\downarrow$), then the two electrons can travel to the S-side of the S/N interface by forming a Cooper pair, as shown in Fig. 2.4.(a). The disappearance of the second electron left a hole with (ϵ,k,$\uparrow$) in the N-side. In the excitation diagram Fig. 2.5, this hole has a negative group velocity which is just opposite to the group velocity of the first electron. Therefore, this process is called a reflection process.

Correspondingly, the "leakage" of Cooper pairs into normal metal from S side can be viewed as inverse Andreev reflection. The two electrons in one Cooper pair enter the N side with roughly equal opposite momenta close to k_f. According to the uncertainty principle, the wave-functions of these two electrons remain in phase for a time-span around $\hbar/\epsilon$ in the N side. In the clean limit this time can be equated with one coherence length $\xi_N = \hbar v_f/\epsilon$, whereas it corresponds to $\sqrt{\hbar D/\epsilon}$ in the dirty limit (The clean and dirty limits refer to the mean free path being longer or shorter than ξ_N, respectively) . Here v_f is the Fermi velocity and D is the diffusion constant. Since the available range for energy ϵ is approximately

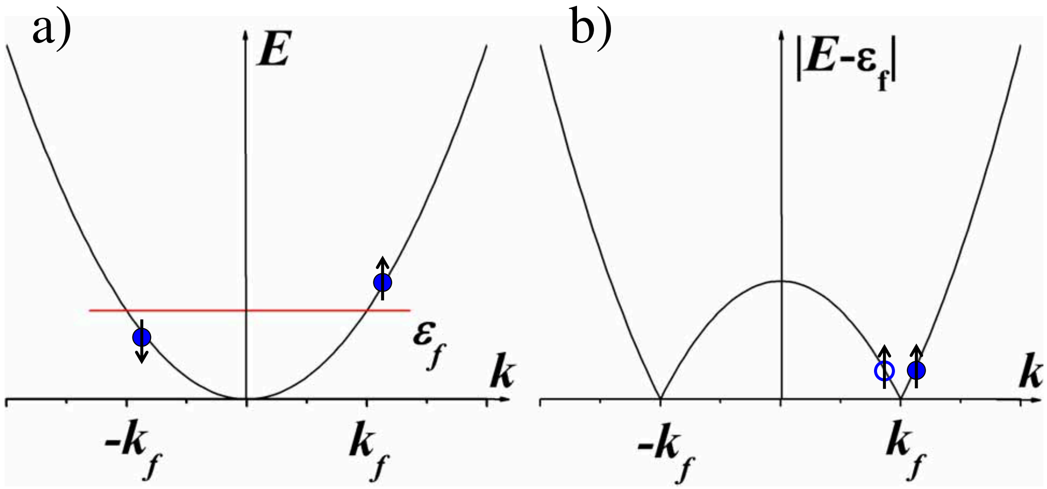

Figure 2.5: a)1-D free electron Dispersion relation in normal metal, showing two electrons with opposite momenta and spins bundle together to penetrate into S side. b) Same process shown in a excited dispersion spectrum, where the absence of the second electron is represented as a reflected hole.

$2\pi k_B T$ in the normal metal, we get these expressions for the "normal metal coherence length" $\xi_N = (\hbar v_f)/(2\pi k_B T)$ *Clean limit*; $\xi_N = \sqrt{(\hbar D)/(2\pi k_B T)}$ *Dirty limit.*

Similarly, Cooper pairs can also leak into a ferromagnetic layer when they are in electrically good contact. The main difference is that the energy dispersion spectrum in a ferromagnet is not as simple as in a normal metal. Spin-up electrons and spin-down electrons are in two different bands now, shifted by the exchange coupling energy $2E_{ex}$ shown in Fig. 2.6 . Therefore, the Fermi wave vectors for spin-up and spin-down bands are different. In order to obey the energy conservation, electrons have to adjust their kinetic energy, which in turn results in the shift of momentum by $\Delta P = 2E_{ex}/v_f$ [20]. This further leads to the shift of center-of-mass momentum for one pair of electrons with spin configuration $|\uparrow\downarrow>$ by $Q = 2E_{ex}/v_f$, while $|\downarrow\uparrow>$ electron pairs gain the center-of-mass momentum by $-Q$. Since we are considering spin-singlet Cooper pairs, the spin part wave function undergoes the following transformation,

$$\frac{1}{\sqrt{2}}[|\uparrow\downarrow> -|\downarrow\uparrow>] \Longrightarrow \frac{1}{\sqrt{2}}[\exp[iQx/\hbar] \mid\uparrow\downarrow> -\exp[-iQx/\hbar] \mid\downarrow\uparrow>] \tag{2.4}$$

after entering the ferromagnetic layer. After taking into account the fact that Cooper pairs are incident on the interface from all possible angles, the net gain of the center-of-mass momentum will be $Q/\cos\theta$ for each different incident angle θ. In the clean limit after averaging over all possible angles, we would get the pair correlation function proportional to $\sin(x/\xi_F)/(x/\xi_F)$ in F layer, where $\xi_F = \hbar v_f/2E_{ex}$. In the dirty limit, the pair correlation distribution in F layer is proportional to $\sin(x/\xi_F^*)\exp(-x/\xi_F^*)$ with $\xi_F^* = \sqrt{\hbar D/E_{ex}}$ after counting the presence of the strong disorder scattering into the consideration. The wave function of Cooper pairs not only decays away from the S/F interface as in the case of S/N interface, but also oscillates in space which is absent in the S/N case.

We show the schematic behavior of the superconducting pair correlations near the S/N and S/F interfaces in Fig. 2.7. Coherence lengths for clean and dirty limits are also summarized in the Table 2.1. The biggest difference here in going from S/N to S/F is that the thermal energy k_BT is replaced by the exchange energy E_{ex}. And For Fe, Co, Ni, the corresponding Curie temperature T_C is 1043K, 1388K and 627K. If we just esimate $E_{ex} \approx k_BT_C$ and assume $T_C = 1000K$ and $T = 4K$, then we can easily see $(E_{ex})/(k_BT) = 250$, which means that ξ_F would be much shorter compared with ξ_N. At low temperature ξ_N would be around one μm while ξ_F would be around a few nm.

	Clean limit	Dirty limit
Normal metal	$(\hbar v_f)/(2\pi k_BT)$	$\sqrt{(\hbar D)/(2\pi k_BT)}$
Ferromagnet	$(\hbar v_f)/(2E_{ex})$	$\sqrt{(\hbar D)/(E_{ex})}$

Table 2.1: Superconducting Coherence Lengths in ferromagnet and normal metal given both in clean limit and in dirty limit.

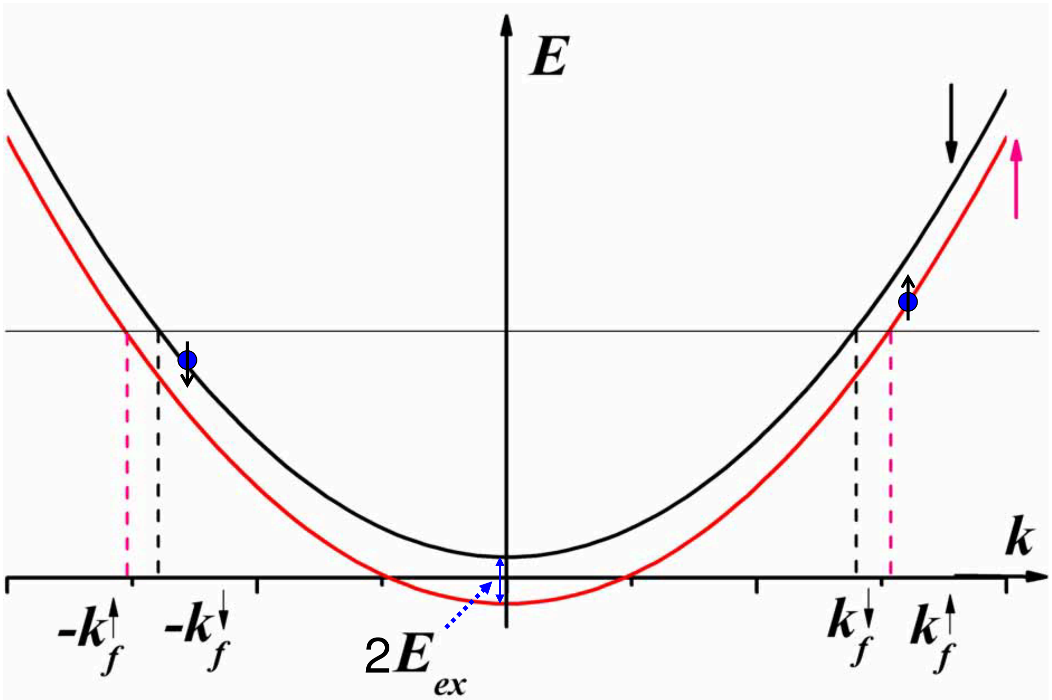

Figure 2.6: 1-D free electron Dispersion relation in Ferromagnet, showing that two electrons with opposite momenta and spins entering from S into F side. In this case there is an exchange energy gap between spin-up band and spin-down band, which results in a shift between wave vectors of the two electrons.

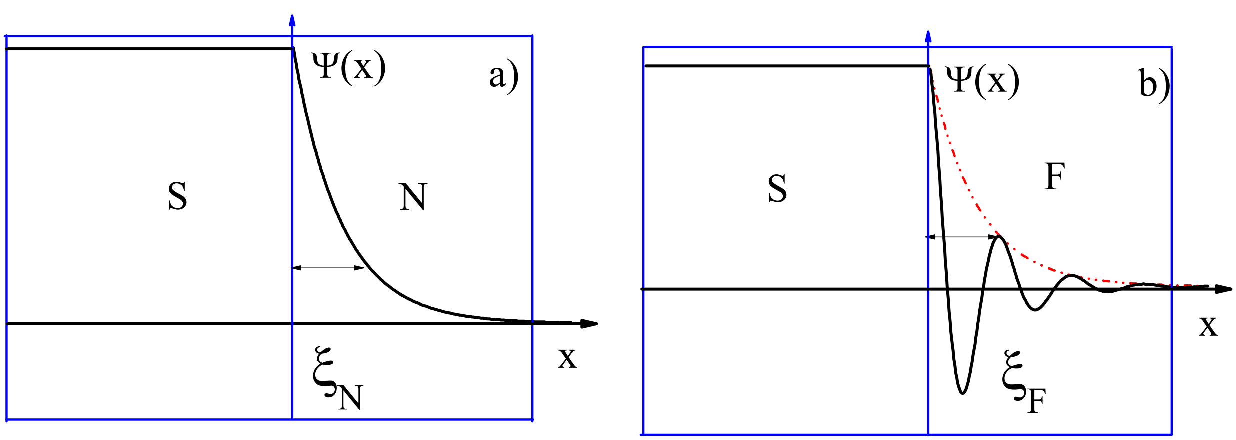

Figure 2.7: Schematic behavior of the superconducting pair correlations near the a) superconductor-normal metal interface and b) superconductor-ferromagnet interface.

Although the coherence length in ferromagnetic materials is very short, there is another side of story which is much more interesting. It is the oscillatory nature of this short ranged proximity effect as indicated in the Fig. 2.7.b). This oscillatory proximity effect leads to critical superconductivity temperature (T_c) oscillations in S/F bilayers [50, 65], Josephson critical current oscillation in S/F/S Josephson junctions [54, 12, 58, 52, 55, 56] and density-of-states oscillations in S/F bilayers [42, 13]. Since the short ranged proximity effect in S/F systems has been studied extensively, it will not be the main topic of my research.

2.3.2 Long range spin-triplet proximity effects in systems with non-collinear magnetization

As we already learned in the last section, the traditional spin-singlet correlation in S/F systems is really very short ranged. So we will ask whether this is the only case in S/F systems. More than ten years ago, theorists [8, 36] explored the possibility of a long-range proximity effect in S/F systems. They predicted that the presence of magnetic inhomogeneities in S/F systems could induce "odd-triplet superconductivity", which corresponds to electron pairs with $|\uparrow\uparrow>$ or $|\downarrow\downarrow>$. Since these electron pairs will enter into the same spin band of the ferromagnetic layer, they would not experience the exchange field any more, which in turn results in a long-range proximity effect with spin-triplet correlation.

Following the similar mechanism suggested in [8, 10], theorists proposed magnetic inhomogeneous S/F systems would generate a long-range spin-triplet correlation (LRSTC) as shown below:

1. Intrinsic inhomogeneity: Domain walls in the ferromagnet are very good candidates suggested by some theorists [25, 72]. The other way is through spiral magnetic order

in the ferromagnet [17, 71].

2. Extrinsic inhomogeneity: Engineered structures with multilayered F-layer of non-collinear magnetizations [70],where different F-layers have different directions of magnetization.

3. Spin active region: Here the generation of the long range spin-triplet correlation is through the spin-flip process at the S/F interface [23, 3].

There were two earlier experimental attempts [39, 60] that provided some evidence for spin-triplet correlations. Keizer et al. [39] studied NbTiN/CrO_2/NbTiN Josephson junctions using CrO_2 as the F-layer and NbTiN as the S-layer. Sosnin et al. [60] worked on a Holmium (Ho) wire attached to superconducting electrodes. At that time, there was not only difficulty to find new systems which could generate the long range spin-triplet correlation, but also it was difficult to reproduce the results. In 2010, several groups [62, 57, 2] around the world successfully provided significant evidence for this long-range spin-triplet correlation, including ours [34]. Especially our well-engineered structure [35, 73, 26] provides a very reproducible system to study the long range spin-triplet correlation.

Even though there are abundant theory papers on this topic, it is very hard to interpret them because they relied very heavily on the quasi-classical Green's function formalism. Yet, here is one very simple diagram in Fig. 2.8 which sketches out the majority of the physics behind the generation of the long-range spin-triplet correlation. It is very similar to the argument when we deal with spin eigenstates of one electron in different systems. For example, one spin-up state in one system can evolve into spin-up and spin-down states in another system.

When the spin-singlet Cooper pair enters F1, it develops into one short ranged spin-singlet

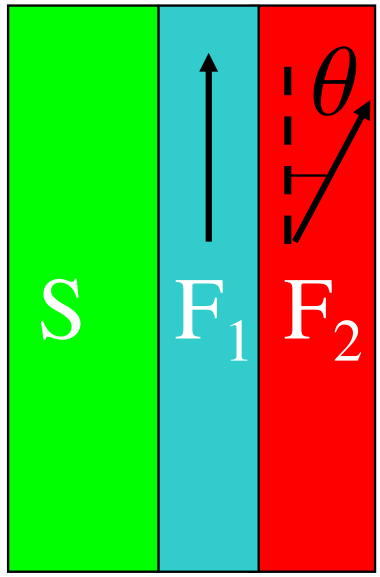

Figure 2.8: Mechanism for Spin triplet generation in presence of magnetic inhomogeneities where the second magnetization (F2) does not align with the first one (F1).

pair $|0,0>$ and one short ranged spin-triplet pair$|1,0>$. Then this short ranged spin-triplet pair $|1,0>$ can evolve into three spin-triplet components, two of which are long-ranged, as depicted in Eqn. 2.5.

$$S: \qquad \frac{1}{\sqrt{2}}[|\uparrow\downarrow> - |\downarrow\uparrow>]$$

Spin-singlet Cooper pairs evolve into two components

$$\begin{aligned} F1: \quad |\chi> \quad &= \tfrac{1}{\sqrt{2}}[\exp[iQx/\hbar]\,|\uparrow\downarrow> - \exp[-iQx/\hbar]\,|\downarrow\uparrow>] \\ &= \cos(Qx)|0,0>_{F1} + i\sin(Qx)|1,0>_{F1} \end{aligned} \tag{2.5}$$

"Even spin-triplet pairs" further develop into three more components

$$F2: \quad |1,0>_{F1} = \frac{\sin\theta}{\sqrt{2}}|1,1>_{F2} + \cos\theta|1,0>_{F2} - \frac{\sin\theta}{\sqrt{2}}|1,-1>_{F2}$$

where θ is the angle between the directions of the magnetizations in $F1$ and $F2$, shown in Fig. 2.8. We use the standard notation for singlet and triplet spin states:

$$\begin{aligned} |0,0> &= \frac{1}{\sqrt{2}}[|\uparrow\downarrow> -|\downarrow\uparrow>] \\ |1,1> &= |\uparrow\uparrow> \\ |1,0> &= \frac{1}{\sqrt{2}}[|\uparrow\downarrow> +|\downarrow\uparrow>] \\ |1,-1> &= |\downarrow\downarrow> . \end{aligned} \tag{2.6}$$

In deriving the Eqn. 2.5, we have applied the rotation matrix for total angular momentum $j = 1$ case. Below, we show the rotation matrix on y-axis:

$$R(\theta) = \exp(\frac{-iJ_y\theta}{\hbar}) = \frac{1}{2}\begin{bmatrix} 1+\cos\theta & -\sqrt{2}\sin\theta & 1-\cos\theta \\ \sqrt{2}\sin\theta & 2\cos\theta & -\sqrt{2}\sin\theta \\ 1-\cos\theta & \sqrt{2}\sin\theta & 1+\cos\theta \end{bmatrix}. \tag{2.7}$$

2.4 Ways to detect long range spin-triplet correlation

There are mainly two ways to obtain the signatures of the long-ranged spin-triplet correlation in S/F systems.

The first one is the tunneling spectrum, which measures the differential conductance to obtain the density of states. Kontos et al. [42] and our group [13] applied this technique in measuring proximity-induced density-of-states oscillations in spin-singlet S/F systems, where noncollinear magnetization was not involved. Detecting the long-range triplet correlation in tunneling is more difficult due to the very small signal. I made one attempt to improve the sensitivity of the tunneling experiment, but did not succeed in obtaining clean signals. My naive reason for this is that the traditional Al_2O_3 tunneling barrier might not be very suitable for the current case. We might need a full spin-polarized ferromagnetic oxide to replace the traditional Al_2O_3. Currently, we still have one undergraduate student working on this approach.

The second way to detect the long-range spin-triplet correlations is to measure the Josephson effect in S/F/S junctions, which will be discussed in the rest of the dissertation.

Chapter 3

Josephson Junction

3.1 Josephson effects

Brian Josephson [32, 33] in 1962 predicted theoretically that Cooper pairs could tunnel through a thin barrier when this barrier is sandwiched between two superconductors and the barrier is thin enough. This idea was verified experimentally the following year [1]. People named this effect the "Josephson effect".

Although the Josephson effect was originally predicted and verified for a thin insulating-barrier system, S/I/S, it is a more general effect. Different Josephson junctions can be made depending on the material of the barrier such as normal metal (S/N/S) or ferromagnetic metal (S/F/S). Fig. 3.1 shows a schematic geometry for a Josephson junction at the left side. At the right side of Fig. 3.1, a typical V-I curve is shown for our S/F/S spin-triplet Josephson junctions. We can see clearly from the V-I curve that junctions carry supercurrent until the current reaches the critical value I_C. At current much larger than $|I_C|$, the V-I curve is ohmic.

In order to explain the Josephson effect, let us take a look at the macroscopic quantum model of superconductivity. Along the way to a deeper understanding of superconductivity, one of the main milestones was the development of the phenomenological theory for superconductivity by Fritz and Heinz London [46] and V.L.Ginzburg and L.D. Landau [27]. Fritz

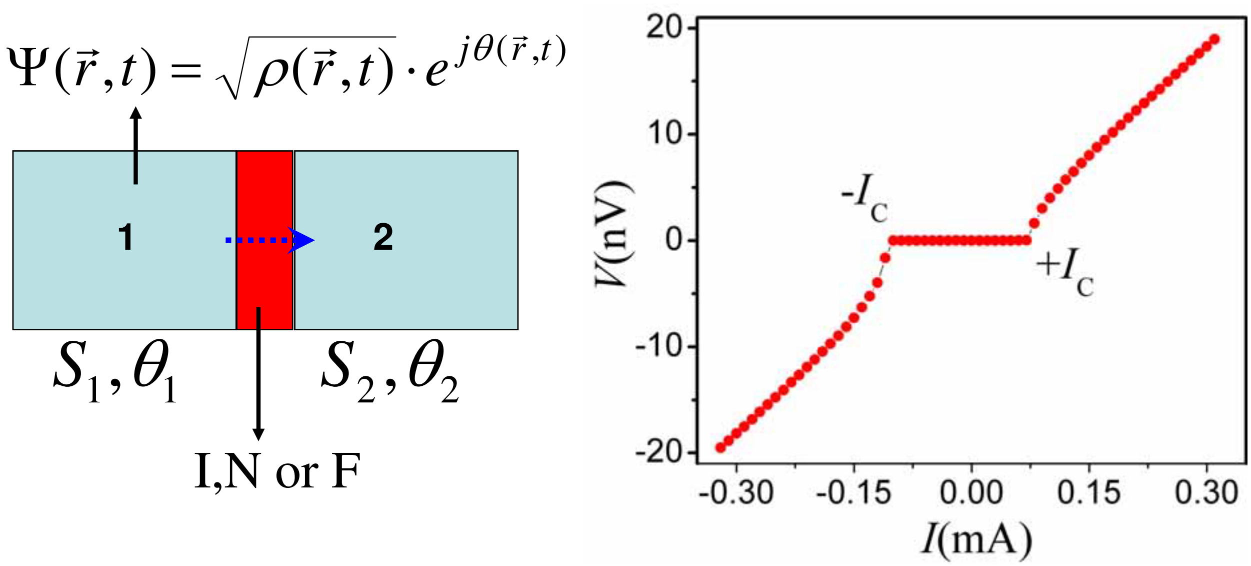

Figure 3.1: Left side is the geometry of two superconductors separated from each other by a non-superconducting barrier to form Josephson junction, which could be normal metal (N), insulator (I) or our ferromagnetic (F). Right side is a typical voltage vs. current characteristic for one of our samples, with critical current $I_C \simeq 0.2mA$.

London realized that superconductivity is an inherently quantum phenomenon manifesting itself on a macroscopic scale. Coherent phenomena in superconductors such as flux quantization provide the bases for the macroscopic quantum model of superconductivity. The key hypothesis of the macroscopic quantum model of superconductivity is that a macroscopic wave function $\Psi(\overrightarrow{r},t)$ can be used to describe the behavior of the whole ensemble of superconducting electrons; Ψ is a complex function with a magnitude and a phase, as shown by Eqn. 3.1. This macroscopic wavefunction obeys the Schrodinger-like Eqn. 3.2 in an electromagnetic field. The microscopic theory of BCS can also be used to justify this hypothesis.

$$\Psi(\overrightarrow{r},t) = \sqrt{n_s^*(\overrightarrow{r},t)}\exp^{i\theta(\overrightarrow{r},t)} \tag{3.1}$$

$$i\hbar\frac{\partial\Psi(\overrightarrow{r},t)}{\partial t} = \frac{1}{2m^*}(\frac{\hbar}{i}\nabla - q^*\mathbf{A}(\overrightarrow{r},t))^2\Psi(\overrightarrow{r},t) + q^*\phi(\overrightarrow{r},t)\Psi(\overrightarrow{r},t) \tag{3.2}$$

where $n_s^*(\overrightarrow{r},t) = \Psi^\dagger(\overrightarrow{r},t)\Psi(\overrightarrow{r},t)$ is the local density of Cooper pairs, $\mathbf{A}$ is the vector potential, ϕ is the scalar potential, m^* is the mass of one Cooper pair and $q^* = -2e$ is the charge of one Cooper pair. Electric field $\mathbf{E}$ and magnetic flux density $\mathbf{B}$ can be expressed in term of $\mathbf{A}$ and ϕ by Eqn. 3.3 and 3.4.

$$\mathbf{E} = -\nabla\phi - \frac{\partial \mathbf{A}}{\partial t} \tag{3.3}$$

$$\mathbf{B} = \nabla \times \mathbf{A} \tag{3.4}$$

Then we can get the flow of Cooper pairs by following the exact same method as we use to get the flow of probability in quantum physics, as shown in Eqn. 3.5.

$$\mathbf{J}_s = \frac{q^*\hbar}{2m^*i}(\Psi^\dagger\nabla\Psi - \Psi\nabla\Psi^\dagger) - \frac{q^{*2}}{2m^*}\Psi\Psi^\dagger\mathbf{A} \tag{3.5}$$

By substituting (3.1) into (3.5), we can obtain the supercurrent equation

$$\mathbf{J}_s = q^*n_s^*(\overrightarrow{r},t)\{\frac{\hbar}{m^*}\nabla\theta(\overrightarrow{r},t) - \frac{q*}{m*}\mathbf{A}(\overrightarrow{r},t)\}. \tag{3.6}$$

Here we clearly can notice that the superconducting current in a superconductor is related to the phase gradient and vector potential $\mathbf{A}$. After we pull $\hbar/m^*$ out of the bracket and introduce a gauge invariant phase gradient $\gamma = \nabla\theta - (q^*/\hbar)\mathbf{A}$, we see

$$\mathbf{J}_s = \frac{q^*n_s^*\hbar}{m*}\gamma. \tag{3.7}$$

So what will determine the current flowing across Josephson junctions? First of all, the current definitely can depend on Cooper pair densities on both sides. Second, it is pretty obvious that the gauge invariant phase gradient γ will play a very crucial role, which will also become a variable. And the Cooper pair density n_s^* in the electrodes is much higher than in the non-superconducting layer, which means we can assume that γ in the two superconducting electrodes is small. Therefore, we can roughly speculate that the current across junctions is governed by the gauge invariant phase difference φ across non-superconducting region, given by

$$\begin{aligned}
\mathbf{J}_s &= \mathbf{J}_s(\varphi) \\
\text{where } \varphi &= \int_1^2 \gamma(\overrightarrow{r}, t) \cdot d\overrightarrow{l} \\
&= \theta_2(\overrightarrow{r}, t) - \theta_1(\overrightarrow{r}, t) - \frac{q^*}{\hbar}\int_1^2 \mathbf{A} \cdot d\overrightarrow{l}.
\end{aligned} \tag{3.8}$$

Similar to any quantum system, any phase change of 2π should not make any difference on the final $\mathbf{J}_s$, which means $\mathbf{J}_s(\varphi) = \mathbf{J}_s(\varphi + 2n\pi)$. At the same time, if there is no current across the junction, both the phase gradient and the phase difference must be zero. In this case, $\mathbf{J}_s(0) = \mathbf{J}_s(2n\pi) = 0$. From these two arguments, we can obtain the current-phase relation

$$\mathbf{J}_s(\varphi) = J_c \sin(\varphi) + \sum_{m=2}^{\infty} J_m \sin(m\varphi) \tag{3.9}$$

where J_c is the critical current density, which is determined by the coupling strength, Cooper pair densities in the electrodes. When the Josephson coupling is weak, the second term of Eqn. 3.9 can be neglected.

In order to get the voltage-phase relation, we need first to derive the so-called energy-phase relation (3.10) by substituting (3.1) into (3.2) and assuming $n_s^* = const.$

$$-\hbar\frac{\partial\theta}{\partial t} = \frac{m^*}{2n_s^{*2}q^{*2}}\mathbf{J}_s^2 + q^*\phi \tag{3.10}$$

Then we take the derivative of the gauge invariant phase difference

$$\frac{\partial\varphi}{\partial t} = \frac{\partial\theta_2}{\partial t} - \frac{\partial\theta_1}{\partial t} - \frac{q^*}{m^*}\frac{\partial}{\partial t}\int_1^2 \mathbf{A}\cdot d\overrightarrow{l} \tag{3.11}$$

Substitution of (3.10) into (3.11) yields the second Josephson equation

$$\begin{aligned}\frac{\partial\varphi}{\partial t} &= \frac{q^*}{\hbar}[\phi(1) - \phi(2) - \int_1^2 \frac{\partial\mathbf{A}}{\partial t}\cdot d\overrightarrow{l}] \\ &= \frac{q^*}{\hbar}\int_1^2 (-\nabla\phi - \frac{\partial\mathbf{A}}{\partial t})\cdot d\overrightarrow{l} \\ &= \frac{q^*}{\hbar}\int_1^2 \mathbf{E}(\overrightarrow{r}, t)\cdot d\overrightarrow{l}. \end{aligned} \tag{3.12}$$

Here we summarize below the two Josephson equations

$$\mathbf{J}_s(\varphi) = J_c\sin\varphi \qquad (1st\ Josephson\ equation) \tag{3.13}$$

$$\frac{\partial\varphi}{\partial t} = \frac{2\pi}{\Phi_0}V \qquad (2nd\ Josephson\ equation) \tag{3.14}$$

$$\varphi = \theta_2(\overrightarrow{r}, t) - \theta_1(\overrightarrow{r}, t) - \frac{q^*}{\hbar}\int_1^2 \mathbf{A}\cdot d\overrightarrow{l} \tag{3.15}$$

where we have introduced the quantum flux $\Phi_0 = h/2e$ and the voltage drop across the junction $\int_1^2 \mathbf{E}(\overrightarrow{r}, t)\cdot d\overrightarrow{l} = V$.

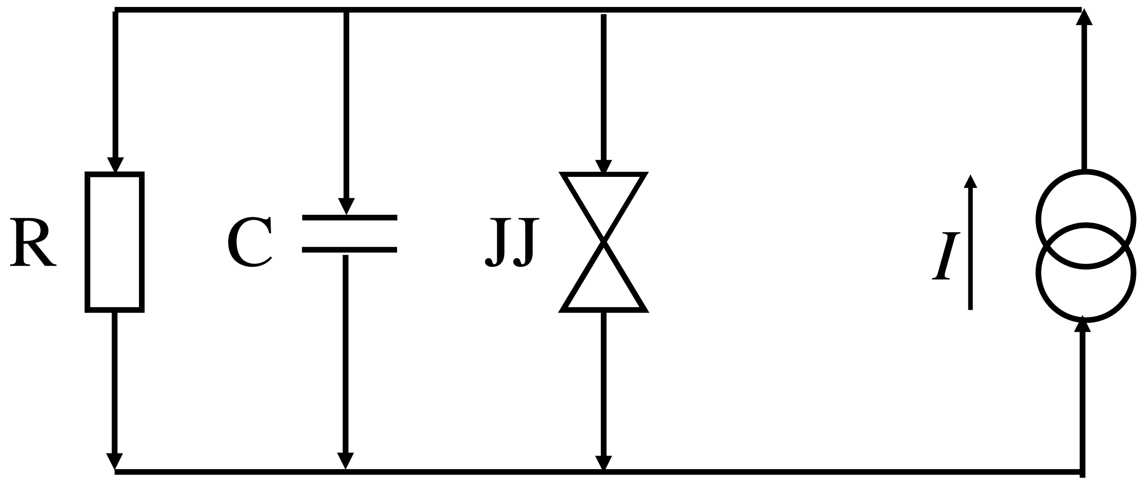

Figure 3.2: Equivalent circuit of Josephson junction,resistively and capacitively shunted junction model.

3.2 Resistively and capacitively shunted junction model

According to the Josephson equations, the current passing across a junction would determine the phase-difference of the junction. For the case $I < I_c$, a voltage would not develop across the junction and the phase-difference across the junction also would stay constant; but for $I > I_c$, situation will become more complicated because the junction will evolve into the voltage state, where we need to solve one non-linear equation in order to get overall knowledge of the system. We will introduce below a well known model called Resistively and Capacitively Shunted Junction (RCSJ) model, as shown in Fig. 3.2. In this model, we consider the electron-pair current, the current of normal unpaired electrons due to the voltage across the junction and the displacement current from the capacitance formed by the two close superconductor surfaces. If we bias a junction with a constant current I, we can write down the following equation

$$I = C\frac{dV}{dt} + \frac{V}{R} + I_c \sin\varphi \tag{3.16}$$

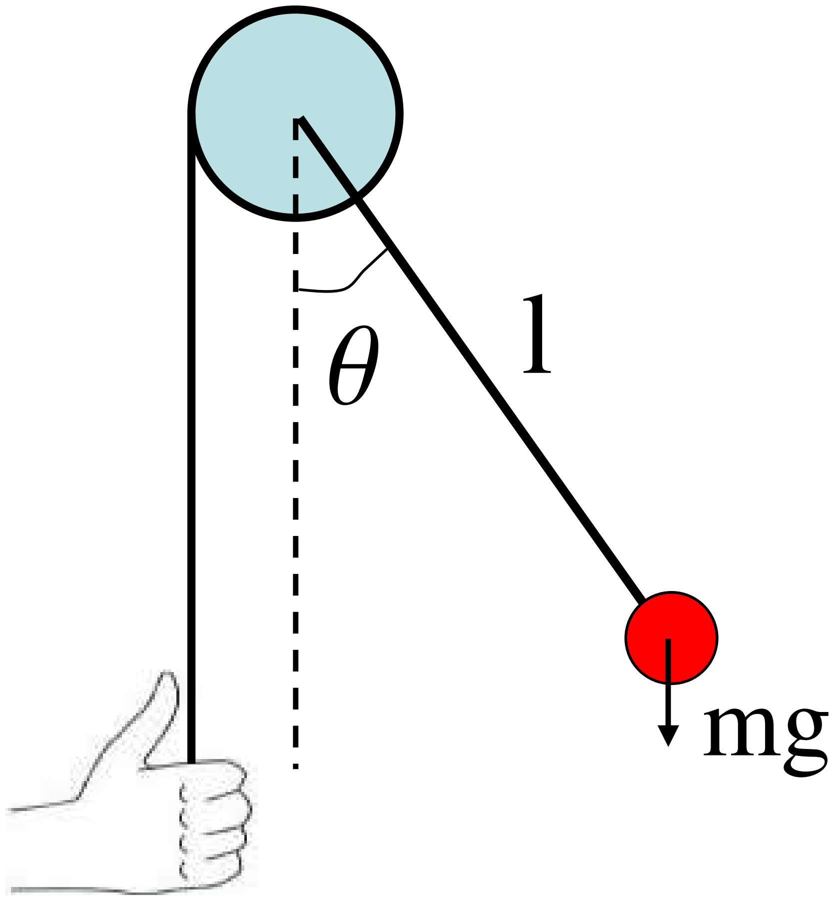

Figure 3.3: A pendulum analogue of a Josephson junction. A bob of mass m is attached to a weightless rigid rod, which can rotate freely around the pivot. A external torque T is applied by a very steady hand, which can swing the pendulum out of the vertical by an angle θ.

By replacing V with $(\Phi_0/2\pi)\partial\varphi/\partial t$, we can find out that the total current is related to the phase difference φ with the result that

$$I = \frac{\Phi_0 C}{2\pi}\frac{\partial^2\varphi}{\partial^2 t} + \frac{\Phi_0}{2\pi R}\frac{\partial\varphi}{\partial t} + I_c \sin\varphi \tag{3.17}$$

which is very analogous to the motion equation (3.18) of a rigid pendulum shown in Fig. 3.3.

$$T = ml^2\ddot{\theta} + \Gamma\dot{\theta} + mgl\sin\theta \tag{3.18}$$

The correspondence between the electrical properties of the junction and the mechanics of the pendulum is shown below,

$$
\begin{aligned}
\text{Josephson Junction} & \qquad\qquad \text{pendulum} \\
\text{Phase difference: } \varphi & \longleftrightarrow \text{Deflection: } \theta \\
\text{Total current: } I & \longleftrightarrow \text{Applied Torque: } T \\
\text{Capacitance: } C & \longleftrightarrow \text{Moment of inertia: } ml^2 \\
\text{Normal tunneling conductance: } 1/R & \longleftrightarrow \text{Viscous damping: } \Gamma \\
\text{Critical current: } I_c & \longleftrightarrow \text{Critical torque: } mgl \\
\text{Voltage across junction: } V = \frac{\Phi_0}{2\pi}\frac{\partial\varphi}{\partial t} & \longleftrightarrow \text{Angular velocity: } \omega = \dot{\theta}.
\end{aligned}
$$

If we apply a small torque, the pendulum will finally settle down at a constant deflection angle and there is also no angular velocity. Similarly, if a current smaller than I_c passes through the junction, there's only a superconducting pair current and no voltage will develop across the junction (φ is time-independent). On the other hand, if the torque is large enough to deflect the pendulum by 90^o, any further increase in the torque will result in the rotation of the pendulum, which will lead to a non-zero angular velocity $\dot{\theta}$. Equivalently, any current larger than I_c will drive the junction into the voltage state. For $|I| >> I_c$, $\partial\varphi/\partial t$ is proportional to I, so V-I curve is ohmic. Since Eqn. 3.17 and Eqn. 3.18 are both nonlinear equations, it is impossible to obtain analytical solutions for arbitrary I. But if we approximate $\sin\varphi$ as φ, we can solve a second order linear differential equation with constant coefficients to get one important parameter, namely the damping coefficient for a Josephson junction $\lambda = (\Phi_0/2\pi R)/(2\sqrt{(\Phi_0 C/2\pi)I_c}) = (\sqrt{(\Phi_0/2\pi)})/(2\sqrt{R^2 C I_c})$, which can be related to the well-known Stewart-McCumber parameter [48, 63] $\beta_c = (R^2CI_c)/(\Phi_0/2\pi) = 1/(4\lambda^2)$.

Similar to some classical mechanical or electrical systems, Josephson junctions can also be identified as underdamped or overdamped ones based on the β_c.

1. Underdamped Josephson junctions: For the $\beta_c > 1$ case, the junction capacitance and/or resistance are large, which is very similar to the underdamped pendulum case where the moment of inertia of the pendulum is large and/or the damping is very small. Fig. 9.3 in the appendix shows a typical V-I curve.

2. Overdamped Josephson junctions: For the $\beta_c << 1$ case, the junction capacitance and/or resistance are small, which corresponds to the overdamped pendulum case where the moment of inertia of the pendulum is small and/or the damping is very large. Fig. 3.1 demonstrates a characteristic V-I curve for one of our S/F/S junctions, where the voltage branch satisfies a simple form $V = R \cdot Re\{(I^2 - Ic^2)^{1/2}\}$.

3.3 0 and π Josephson junctions

Even though no energy will be dissipated in a Josephson junction in the superconducting state, there is a finite energy stored in the junction. As we increase the current, the phase difference of the junction has to change, which corresponds to a finite voltage. The energy stored in the Josephson junction can be given by

$$\begin{aligned} E_J &= \int_0^{t_f} I \cdot V dt \\ &= \int_0^{t_f} I_c \sin \widetilde{\varphi} \left(\frac{\Phi_0}{2\pi} \frac{\partial \widetilde{\varphi}}{\partial t}\right) dt \end{aligned} \tag{3.19}$$

With the phase $\varphi(0) = 0$ and $\varphi(t_f) = \varphi$, we can get

$$\begin{aligned} E_J &= \frac{\Phi_0 I_c}{2\pi} \int_0^{\varphi} \sin\widetilde{\varphi} d\widetilde{\varphi} \\ &= \frac{\Phi_0 I_c}{2\pi}(1 - \cos\varphi) = E_{J0}(1 - \cos\varphi) \end{aligned} \tag{3.20}$$

People usually call E_J the Josephson coupling energy, where $E_{J0} = (\Phi_0 I_c)/(2\pi)$. We also can see that the supercurrent of the junction is related to the Josephson energy E_J of the system by

$$I = \frac{2\pi}{\Phi_0}\frac{\partial E_J}{\partial\varphi} \tag{3.21}$$

Eqn.(3.20) corresponds to a Josephson junction with the minimum Josephson energy at $\varphi = 0$. Conventional Josephson junctions (the barrier is insulator or normal metal) most likely follow this energy-phase relation. We call them 0-junctions.

In 1965, Kulik [44] predicted a negative critical current $I_c < 0$ when studying spin flip tunneling through an insulator with magnetic impurities. In 1977, Bulaevskii et al. [14] showed that under certain conditions, spin flip tunneling due to magnetic impurities could lead to a π phase shift, as shown in Figure 3.4. The ground state now corresponds to a phase difference of $\phi = \pi$. This type of Josephson junction is called a π-junction. In 1982, Buzdin [15] predicted that the critical current I_c of S/F/S Josephson junctions would display damped oscillations as a function of the ferromagnetic layer thickness, where the vanishing of the critical current signals the transition between the 0 state and the π state as shown in Figure 3.5. This transition between two states in S/F/S junctions can be correlated with the sign change of the oscillating pair correlation in F layer shown in Fig. 2.7. And we mentioned at the end of the section 2.3.1, several researchers have observed Josephson

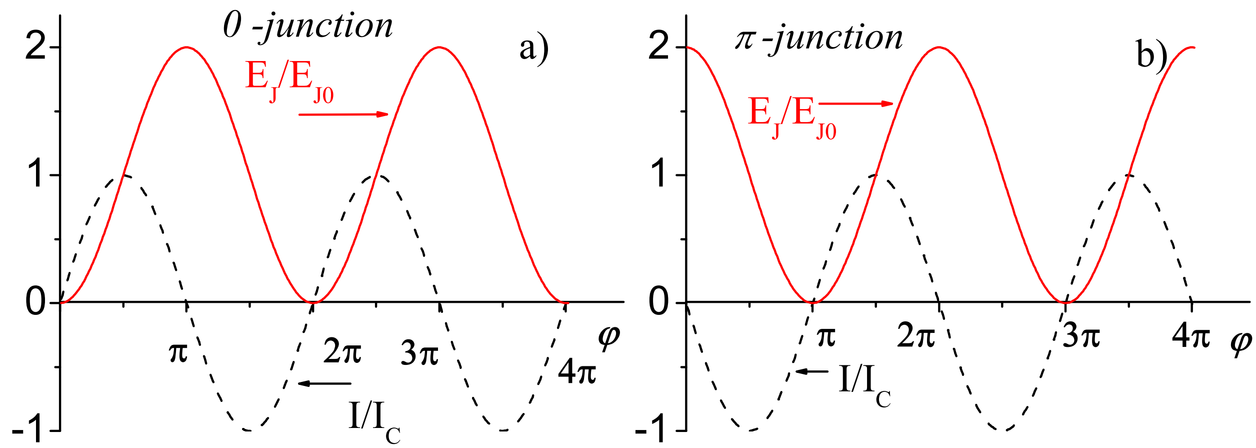

Figure 3.4: Normalized Josephson junction current and coupling energy with phase-difference φ as a variable. a) Zero-junction, b) π-junction.

junction critical current oscillations in S/F/S Josephson junctions [54, 58, 52, 55, 56]. For example, Ryazanov and his co-workers [54, 52] studied junctions with a weak ferromagnetic alloy CuNi and they first observed observe the 0-π transition. Later Robinson et al. [55, 56] found the 0-π transition in S/F/S Josephson junctions using strong ferromagnets, Ni, Co, Fe and Permalloy ($Ni_{80}Fe_{20}$).

3.4 Fraunhofer Patterns: magnetic field dependence of critical current in Josephson junction

Since we are working with finite-size Josephson junctions, a magnetic field applied in the plane of a Josephson junction will lead to a space dependent current density due to the space dependent gauge invariant phase difference by following Eqn.(3.15).

When a uniform magnetic field of flux density B_{ex} is applied parallel to a superconductor surface, the superconductor will produce enough screening current to counteract the magnetic field, which leads to a finite penetration depth λ_L of the magnetic field. The magnetic field

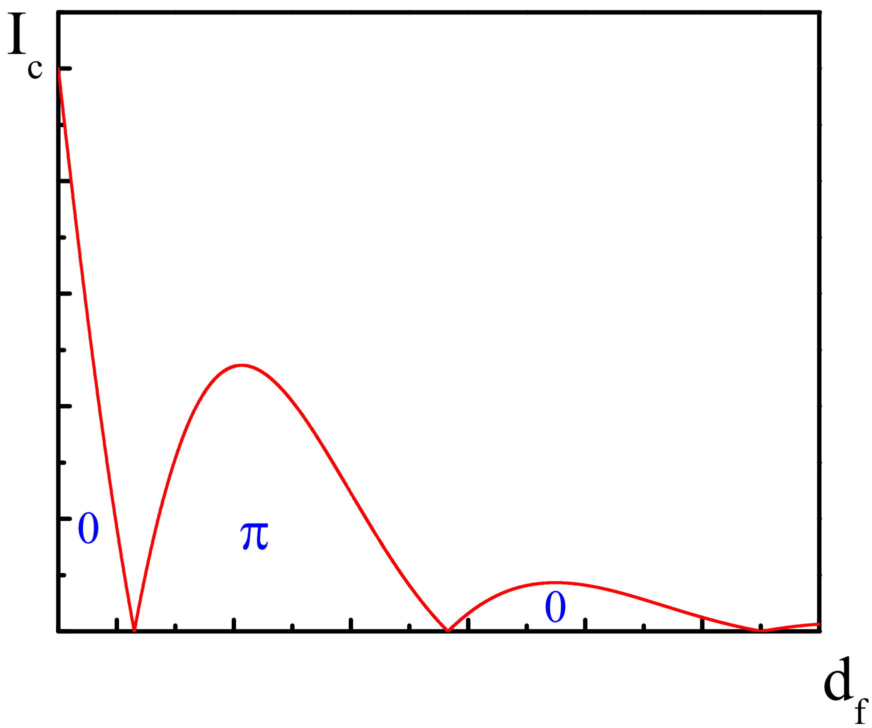

Figure 3.5: Oscillatory dependence of critical current of S/F/S junctions as a function of the ferromagnetic layer thickness, d_f predicted by [15].

will decay exponentially away from the surface given by

$$B(x) = B_{ex} \exp(-\frac{x}{\lambda_L}). \tag{3.22}$$

λ_L is called the London penetration depth and is given by

$$\lambda_L = \sqrt{\frac{m}{\mu_0 n_s e^2}} \tag{3.23}$$

where n_s is the density of the Cooper pairs, m is the electron mass and e is the charge.

We consider a circular Josephson junction with diameter D in an external applied field $\mathbf{B_{ex}} = (0, B_y, 0)$, as shown in Fig. 3.6. In order to study the effect of the applied magnetic field, we need to find out the phase shift introduced between two positions "ad" and "bc"

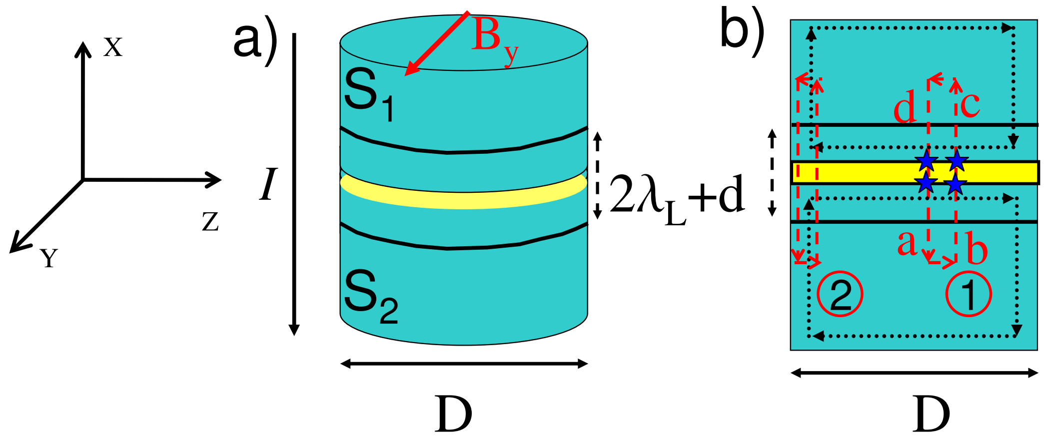

Figure 3.6: a)Schematic picture of a circular Josephson junction in an external applied field. Current flows in the x-direction, magnetic field is along the y-direction. d is the thickness of non superconducting layer, D is the diameter of the junction and λ_L is the London penertration depth. b)Cross section of the junction. The black dotted lines represent the screening current around the bulk superconducting layers. The two red dot contours show two different integration loops. (Not scale to the real dimension!)

along the z-direction. First we draw a closed contour shown in Fig. 3.6.b, along which the total phase difference has to be $2\pi n$, that is

$$\begin{aligned}\oint \nabla\theta \cdot d\mathbf{l} &= 2\pi n \\ &= \Delta\theta_{a\Rightarrow b} + \Delta\theta_{b\Rightarrow c} + \Delta\theta_{c\Rightarrow d} + \Delta\theta_{d\Rightarrow a} \end{aligned} \tag{3.24}$$

In order to get various terms for Eqn. 3.24, we can recall the gauge invariant phase gradient Eqn. 3.7 in the bulk superconducting region to get

$$\nabla\theta = \frac{2\pi}{\Phi_0}\left(\frac{m^*}{n_s q^{*2}}\mathbf{J_s} + \mathbf{A}\right) \tag{3.25}$$

and use the gauge invariant phase difference across the non-superconducting region (Eqn. 3.15)

$$\varphi = \theta_2(\overrightarrow{r}, t) - \theta_1(\overrightarrow{r}, t) - \frac{2\pi}{\Phi_0}\int_1^2 \mathbf{A} \cdot d\overrightarrow{l}. \tag{3.26}$$

We can write down each term for Eqn. 3.24,

$$\Delta\theta_{a\Rightarrow b} = \int_a^b \frac{2\pi}{\Phi_0}(\frac{m^*}{n_s q^{*2}}\mathbf{J_s} + \mathbf{A}) \cdot d\overrightarrow{l} \tag{3.27}$$

$$\Delta\theta_{b\Rightarrow c} = -\varphi_{bc} + \frac{2\pi}{\Phi_0}\int_b^c \mathbf{A} \cdot d\overrightarrow{l} \tag{3.28}$$

$$\Delta\theta_{c\Rightarrow d} = \int_c^d \frac{2\pi}{\Phi_0}(\frac{m^*}{n_s q^{*2}}\mathbf{J_s} + \mathbf{A}) \cdot d\overrightarrow{l} \tag{3.29}$$

$$\Delta\theta_{d\Rightarrow a} = \varphi_{ad} + \frac{2\pi}{\Phi_0}\int_d^a \mathbf{A} \cdot d\overrightarrow{l}. \tag{3.30}$$

By substituting Eqn. 3.27-3.30 into 3.24, we can obtain

$$\varphi_{ad} - \varphi_{bc} = 2n\pi - \frac{2\pi}{\Phi_0}\oint_C \mathbf{A} \cdot d\overrightarrow{l} - \int_a^b \frac{2\pi}{\Phi_0}\frac{m^*}{n_s q^{*2}}\mathbf{J_s} \cdot d\overrightarrow{l} - \int_c^d \frac{2\pi}{\Phi_0}\frac{m^*}{n_s q^{*2}}\mathbf{J_s} \cdot d\overrightarrow{l} \tag{3.31}$$

In order to figure out the line integration contribution from current density flowing from “a” to “b” and from “c” to “d”, we need to divide the current density into two components, circulating screen current and external driving current along the negative x-direction. And keep in mind that we are talking about a micron-size contour. The z-axis coordinates for positions “ad” and “bc” are z and $z + dz$, where dz is infinitesimal.

1. External driving current: The current from the external source is flowing along the negative x-direction and the spacial density does not change abruptly. One side of the line integration parallel to the x-axis will cancel the opposite side of the line integration parallel to the x-axis. At the same time, the portion of the line integration along the z-direction (perpendicular to the current) contributes nothing to the integration.

2. Screen current: First let us take a look at the case (Fig. 3.6.b case 1) when the line integral path is away from the London screen region. This line integral is zero, because

the contour can be chosen to be perpendicular to the screening current [6]. Second assume we place the line integral path inside the London screen region (Fig. 3.6.b case 2). Then it is similar to the external driving current case.

Therefore the line integral of the current density vanishes and we get

$$\varphi_{ad} - \varphi_{bc} = 2n\pi - \frac{2\pi}{\Phi_0}\oint_C \mathbf{A}\cdot d\overrightarrow{l} = 2n\pi - \frac{2\pi}{\Phi_0}\delta\Phi \tag{3.32}$$

where $\delta\Phi = B_y(2\lambda_L + d)dz$. Then we can obtain the differential form of phase shift

$$\begin{aligned} \varphi_{bc} - \varphi_{ad} &= -2n\pi + \frac{2\pi}{\Phi_0}B_y(2\lambda_L + d)dz \\ &\Downarrow \\ \frac{\partial\varphi}{\partial z} &= \frac{2\pi}{\Phi_0}B_y(2\lambda_L + d). \end{aligned} \tag{3.33}$$

Integration of Eqn. 3.33 gives us

$$\varphi(z) = \frac{2\pi}{\Phi_0}B_y(2\lambda_L + d)z + \varphi_0 \tag{3.34}$$

Using the current-phase relation, we obtain the supercurrent density

$$J_s(y,z) = J_c(y,z)\sin[\frac{2\pi}{\Phi_0}B_y(2\lambda_L + d)z + \varphi_0]. \tag{3.35}$$

For the simplest case, we assume that the maximum Josephson current density $J_c(y,z)$ of the junction is spatially homogeneous and is equal to J_c. Then for a circular junction, the total current going through the junction can be given by

$$I = J_c \int_{-D/2}^{D/2} \int_{-\sqrt{D^2/4-z^2}}^{\sqrt{D^2/4-z^2}} \sin[\frac{2\pi}{\Phi_0} B_y(2\lambda_L + d)z + \varphi_0] dydz. \tag{3.36}$$

After we maximize Eqn. 3.36 with respect to φ_0, we can obtain the expression for the maximum Josephson critical current,

$$I(B_y) = \Big| J_c \int_{-D/2}^{D/2} \int_{-\sqrt{D^2/4-z^2}}^{\sqrt{D^2/4-z^2}} \cos[\frac{2\pi}{\Phi_0} B_y(2\lambda_L + d)z] dydz \Big|. \tag{3.37}$$

The integral for Eqn. 3.37 can be given

$$I_c(\Phi) = 2I_c(0) \left| \frac{J_1(\frac{\pi\Phi}{\Phi_0})}{\frac{\pi\Phi}{\Phi_0}} \right| \tag{3.38}$$

where $I_c(0) = J_c \pi D^2/4$,$\Phi = B_y(2\lambda_L + d)D$ and J_1 is the first order Bessel function. In Fig. 3.7, we shows a Fraunhofer pattern based on Eqn. 3.38. In Fig. 3.8, we also show the two specific cases (a and c) and one general case (b) for the current density distribution along a small Josephson junction, which correspond the three marked positions in Fig. 3.7.

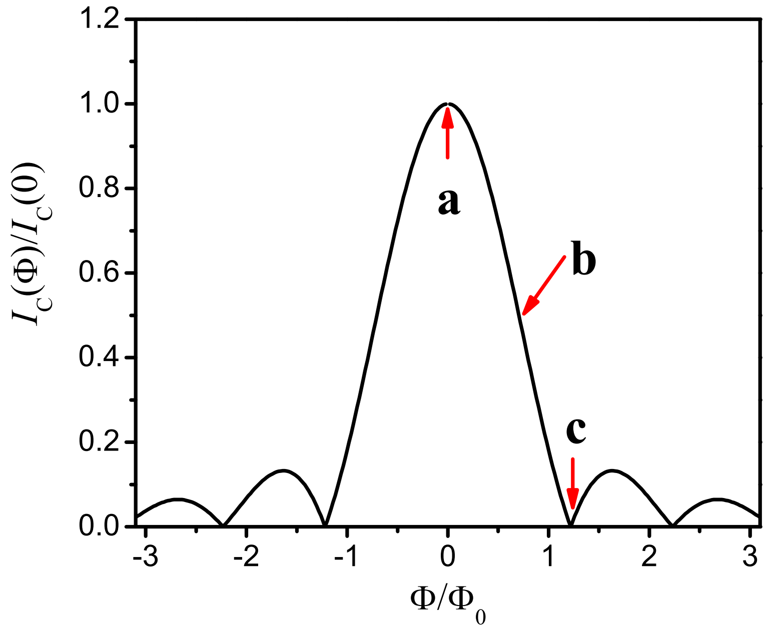

Figure 3.7: Fraunhofer pattern: dependence of the critical current on enclosed flux for a circular Josephson junction. The corresponding current density distribution for a) b) and c) cases is demonstrated in Fig. 3.8

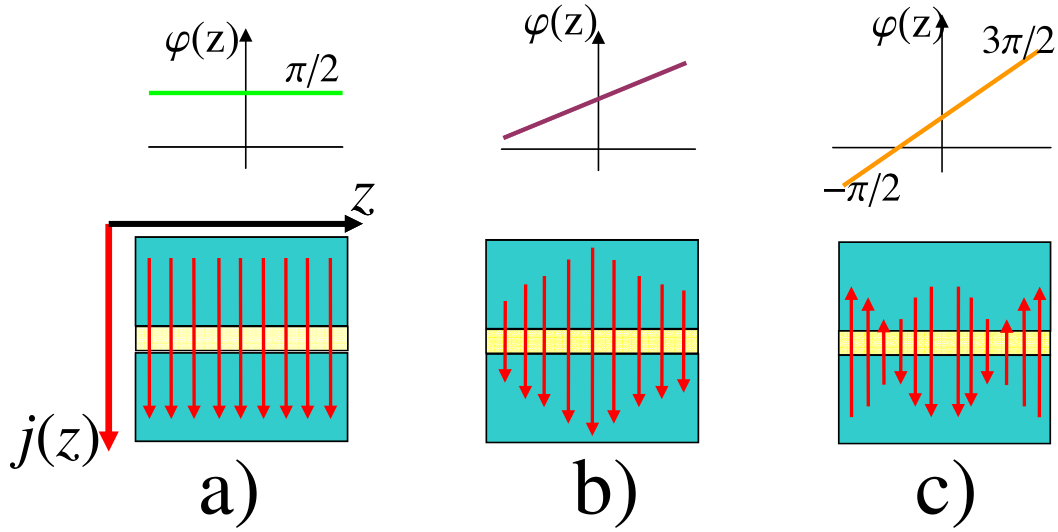

Figure 3.8: Current density across a Josephson junction. The upper part shows the gauge invariant phase difference across the junction vs. the z coordinate and the lower part shows the current density distribution along the z axis. (a)$\Phi = 0$ and $\varphi_0 = \pi/2$; (b)$\Phi \neq 0$ for a general case ; (c)$\Phi = \Phi_0$ and $\varphi_0 = -\pi/2$;

Chapter 4

Sample Fabrication Process and Measurement

In this chapter, the detailed sample fabrication process for ferromagnetic Josephson junctions and SQUID samples will be given. Some special technical concerns regarding growth of our thin films will also be discussed. Even though in name the two kinds of devices seem somewhat different, it turned out that they followed the same process flow diagram. And we also made some samples to characterize the magnetic properties using SQUID magnetometry. Since it is so easy to make these samples with one single sputtering step, I will not discuss it here.

4.1 Bird's-eye view of fabrication of Josephson junction and SQUID device

A sample fabrication diagram is going to be shown to you.

1. Defining the bottom multilayer pattern with photolithography

2. Sputtering the bottom multilayer

3. Make the photoresist pillars

4. Ion milling and silicon monoxide deposition

5. Liftoff

6. Defining the top Nb pattern with photolithography

7. Sputtering the top Nb

Before all of these, we need to dice some 3" Si wafers to get our half inch chips. The Si wafer package was opened inside the Cleanroom to avoid attracting dust particles. After spin coating the wafer with traditional S1813 photoresist and baking the wafer on the hotplate at 95^oC for about one minute, we took this wafer out of the cleanroom to dice it. The S1813 protection layer on these half inch chips was then removed in hot acetone. Finally we ultrasonically cleaned these chips in isopropyl alcohol (IPA) solution to remove any acetone residue. At last, we used nitrogen gas to blow away the IPA. We designed and ordered the required photomasks for our project. Basically, these masks will act as light shutters to define the desired features on our chips with the help of the UV light and photoresist.

4.1.1 Defining the bottom multilayer pattern with photolithography

In order to define our bottom leads, we either used one mechanical mask with one 300 mm narrow strip opening or we used photolithography masks as shown in Fig. 4.1. Photolithography is very similar to the old fashioned film photography. Here we spin coated our chips with S1813 which is a UV light sensitive polymer and baked at 105^oC temperature on the hot plate. After the solvent was totally driven out, we transferred the designed feature from our photomask to our chips. Since S1813 is a positive resist, this means the parts exposed to the

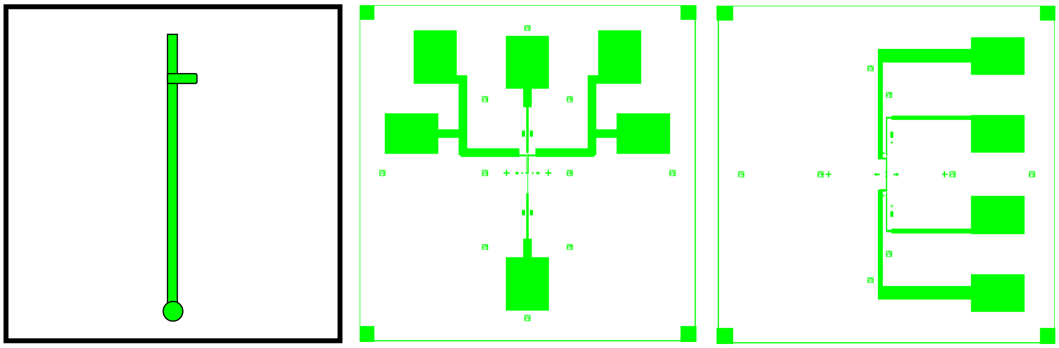

Figure 4.1: The mechanical mask and photomasks used in our bottom leads definition. All the green features correspond to the open places on the chips which will be covered with properly designed S/F/S multilayers. The two right-side photomasks were used for fabricating SQUIDs.

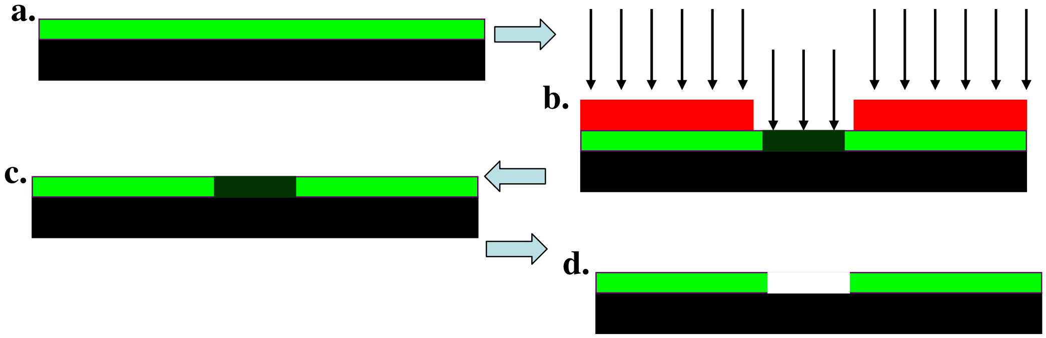

Figure 4.2: a.)Spin coating resist and baking b.) UV light exposure, where red squares represent mask opaque parts and dark blue square means exposed resist part. c.) Soaking in chlorobenzene d.) developing in the photodeveloper

UV light would be removed by the developer as shown in Figure 4.2. The detailed procedure for the S1813 resist will be given in an Appendix. After this, we place our mechanical masks in our sample holders first if we need mechanical masks to define the pattern. Then we load our chips in followed by the heat sink copper pieces and locking bridges. All above steps are carried out in the cleanroom to keep the samples as clean as possible. Then they are ready to be taken out of the cleanroom and to be loaded into our sputtering system.

4.1.2 Sputtering the bottom multilayer

All our multilayer S/F/S thin film deposition was carried out in our computer controlled sputtering system. We have four big triode guns and two small magnetron guns inside the sputtering chamber, as shown in Fig. 4.3. In order to avoid cross contamination, the plasma is confined by the aluminum foil wrapped chimneys. There are two automatically controlled plates inside the chamber. One is the rotating target plate right above the chimneys, which either open to the 4 large targets or two small ones. The other one is the sample positioning and masking plate (SPAMA) with 8 opening spots, which our samples are tightened into. With these two plates controlled by the Labview control program, we deposited our multilayer films very easily. After loading the samples and closing the chamber, the system was baked for approximate six hours and pumped for one or two days using a CTI Cryo-Torr high vacuum pump. The base pressure reached about $3 - 4 \times 10^{-8}$Torr. Once the base pressure was obtained, the system was cooled down with the help of liquid nitrogen. After the temperature on the samples was around -30^{o}C, we started the plasma by maintaining a constant Argon flow rate inside the chamber and turning on the sputter gun controller. After slowly setting the right power for each target source, we still waited for another twenty to thirty minutes to stabilize the guns and also to clean the chamber.

Then we loaded the gun configuration file into our control program and measured the corresponding targets' deposition rates with the film thickness monitoring crystals on the SPAMA plate. With all target rates set right, we sputtered our samples using the right sequence files, which was pretty straightforward. And in order to protect the multilayer films from oxidation, each chip was ended with 5nm Copper, 20nm or 5nm Niobium and 15nm Gold. If Photolithography was used for the bottom layer (e.g. for the SQUID project),

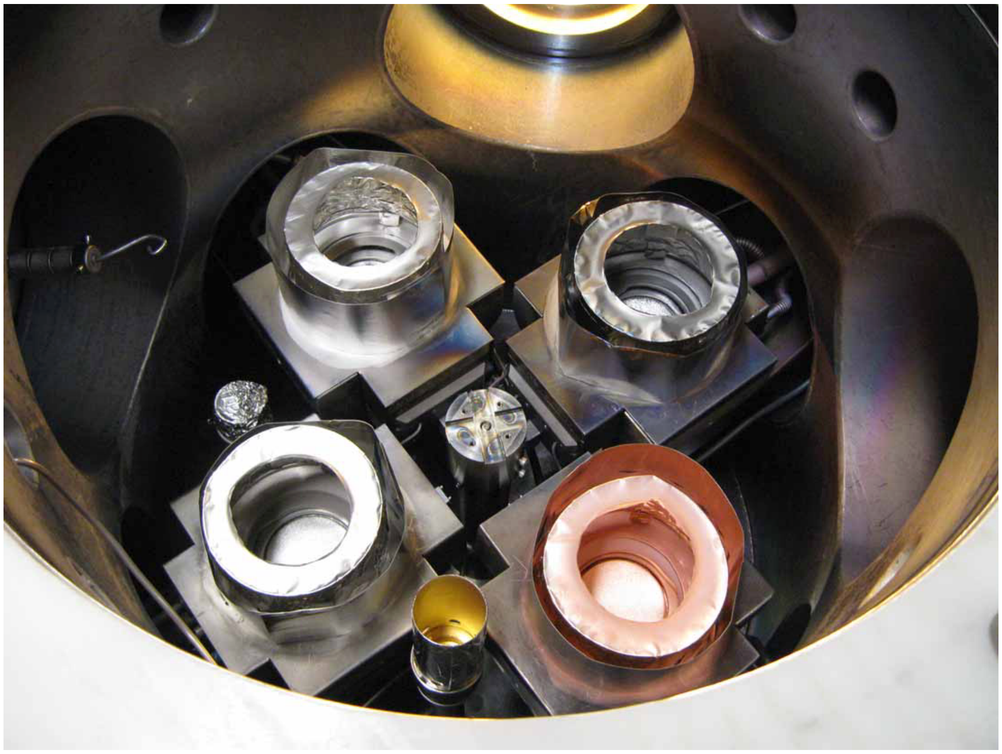

Figure 4.3: Top view of our sputtering chamber with four main triode guns and two small magnetron guns.

the resist must be lifted off after sputtering before proceeding to the next step.

4.1.3 Make the photoresist pillars

After we warmed up the sputtering system and took out our samples, we cleaned our samples again with Acetone followed by IPA. The next very crucial part is our Josephson junction pillar definition. And our samples were ready for the pillar definition now. In order to investigate the area dependence of critical current of our Josephson junctions, the diameters of our pillars were 3μm, 6μm, 12μm, 24μm and 48μm. And for the search for $\pi/2$ junctions in the SQUID project, we defined pillars with 6μm and 12μm diameters. For this step, I used AZ5214E resist and a tone reversal process, which proved to be very effective. One simplified diagram is shown in Fig 4.4. The detailed recipe can be found in the Appendix.

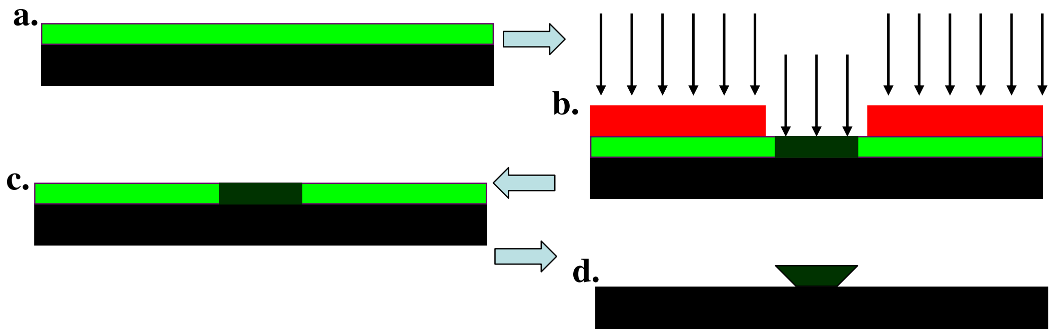

Figure 4.4: a.)Spin coating resist and baking b.) UV light under exposure, where red squares represent mask opaque parts and dark blue square means exposed resist part. c.) Image reversal baking and flood exposure d.) developing in the photodeveloper

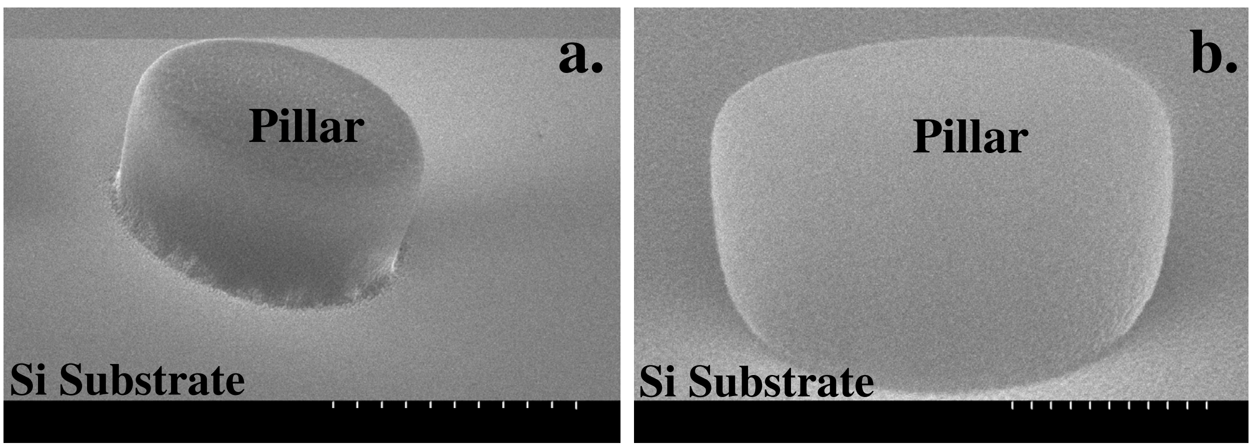

Figure 4.5: a.) Insufficient undercut, too straight resist wall b.) One nice pillar with diameter 3μm having right undercut

First we spin coated our chips with AZ5214E and baked them on the hot plate for about 90 seconds. Then we under-exposed the pillar portion with UV light, which initiates some chemical reaction. A following image reversal bake will further harden the exposed pillars. Finally, we fully flood exposed our chips to the UV light and then developed them for about 40 seconds. Nicely-shaped pillars came out with a good undercut.

Here we show several sample SEM figures to demonstrate what kind of undercut will be called suitable for our purpose. All these samples were coated with a very thin layer of Au in order to prevent charging during SEM imaging and to promote secondary electron emission.

Since we read the resist data sheet carefully and started from our previous recipe, we never obtained worse results than those shown in Fig. 4.5.a), where the wall of the resist was nearly perpendicular to the Si substrate. As we can see, the pillar of Fig. 4.5.b) was perfect for our following process. The negative slope at the base of the pillar not only protected the features underneath but also guaranteed the future liftoff solution penetration after we did our thermal Silicon monoxide deposition. There are several important parameters affecting the final undercut profiles, such as the reflectivity of the bottom layer, the baking temperature, the final contact between chip and mask. The higher the bake temperature is, the smaller the undercut is. The worse the contact is, the bigger the undercut is. For example, if we did very bad work with the contact, the 3μm pillars could totally disappear after developing. And the reflectivity of the bottom layer has more influence on the under-exposure time. In one word, it is not right to claim that the bigger the undercut is, the better the undercut is.

4.1.4 Ion milling and silicon monoxide deposition

Ion milling is used to define the area of the top Nb contact, hence the current-carrying area of the junction.

After having the right size photoresist pillars made, the samples could be loaded into our ion mill chamber. While assembling the sample holders, it is important to apply some silver paste to the back of our chips before attaching the Copper heat sink. Recently, we also used a thin stainless metal piece with one small opening at the center to reduce the processing area. This not only cuts some heat during the ion milling and Silicon monoxide deposition but also leaves two opening spots at the ends of the bottom multilayer strip, which could serve as areas for the two contacts. After the samples were loaded into the ion mill chamber, a base pressure of 3×10^{-8} Torr or better was achieved with overnight pumping by a turbo pump. A 3" Commonwealth Scientific Argon Ion beam source was used to get the ion milling job done at an Argon pressure of 2×10^{-4} Torr. In order to conserve the integrity of the ferromagnetic multilayers, the ion milling process was stopped at the middle of the top protection copper layer, which was mentioned at the end of Section 4.1.2.

After ion milling, the turbo pump gate valve was fully opened again and the argon gas was cut off from the chamber. Then we waited about 1 hour to let the ion mill gun cool down a little bit and to get the chamber pressure down again. Then the heating power of the SiOx source was turned on and slowly increased. In order to increase the uniformity of the deposition, a special kind of baffled boat was used. There are two cavities in this baffled boat. The SiOx was filled into one cavity on top of which there was a cap. When the SiOx sublimes, the gas travels indirectly through a series of baffles to the other open cavity which has an exhaust chimney for the vapor. During the evaporation, the sample was kept rotating in order to increase uniformity. A SiOx layer with thickness around 100nm was used to insulate the bottom multilayer from the following top Nb layer.

After the pillar pattern was transferred to the multilayer, the samples were taken out of the chamber and were ready for resist removal. We used a special resist remover recommended by the resist company, called AZ Kwik Strip Remover. We placed the chips in the hot remover at around 80^oC for about 10 minutes and then agitated the remover by the ultrasonic bath for about another 10 minutes. The portion protected by the resist was clean and shiny as shown in Fig. 4.5 for one pillar with 12μm diameter under optical microscope.

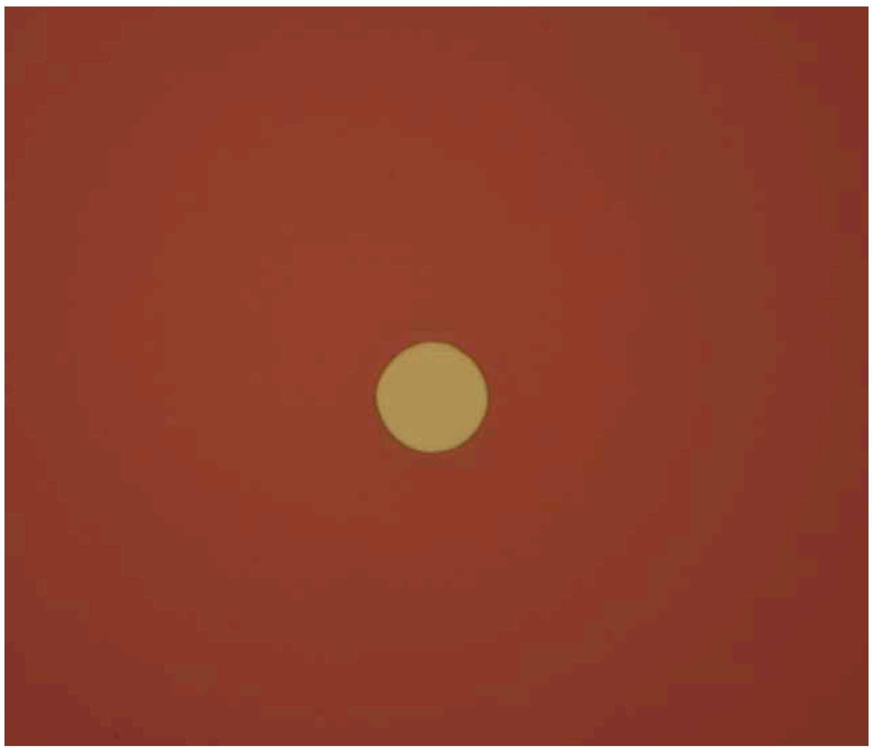

Figure 4.6: One pillar with 12μm diameter under optical microscope after liftoff. The gold colored circle is the exposed portion of the bottom multilayer and was defined by the resist pillar. The red brownish part is the bottom multilayer covered with the SiOx layer.

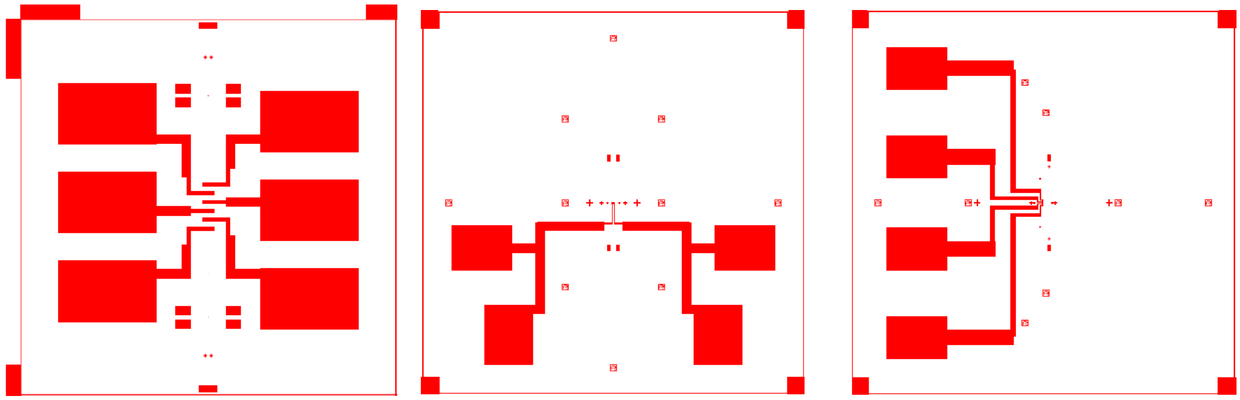

Figure 4.7: The photomasks used in our top leads definition. All the red features correspond to the open places on the chips which will be covered with Nb film. The Left mask was for the area-dependence project. The other two were for the SQUIDs.

4.1.5 Defining the top Nb pattern with photolithography

In order to well define our top leads, we used photolithography masks as shown in Fig. 4.7.

The layout of the top lithography mask carried enough alignment windows to make sure the top features were exposed right on the place we required. For this step, I still applied the same S1813 plus chlorobenzene recipe as we did for our bottom multilayer. After the photolithography and before the sputtering, in the past we did one shallow ion milling for about 10 seconds. However, it took about at least half a day to get every thing ready to start this 10 seconds work. So instead I usually just do one minute Oxygen plasma cleaning in the clean room, which could get rid of most resist residue. About 150nm Niobium was sputtered with an additional 15nm Au protection layer. Fig. 4.8 shows a SQUID sample under optical microscope, after lift-off.

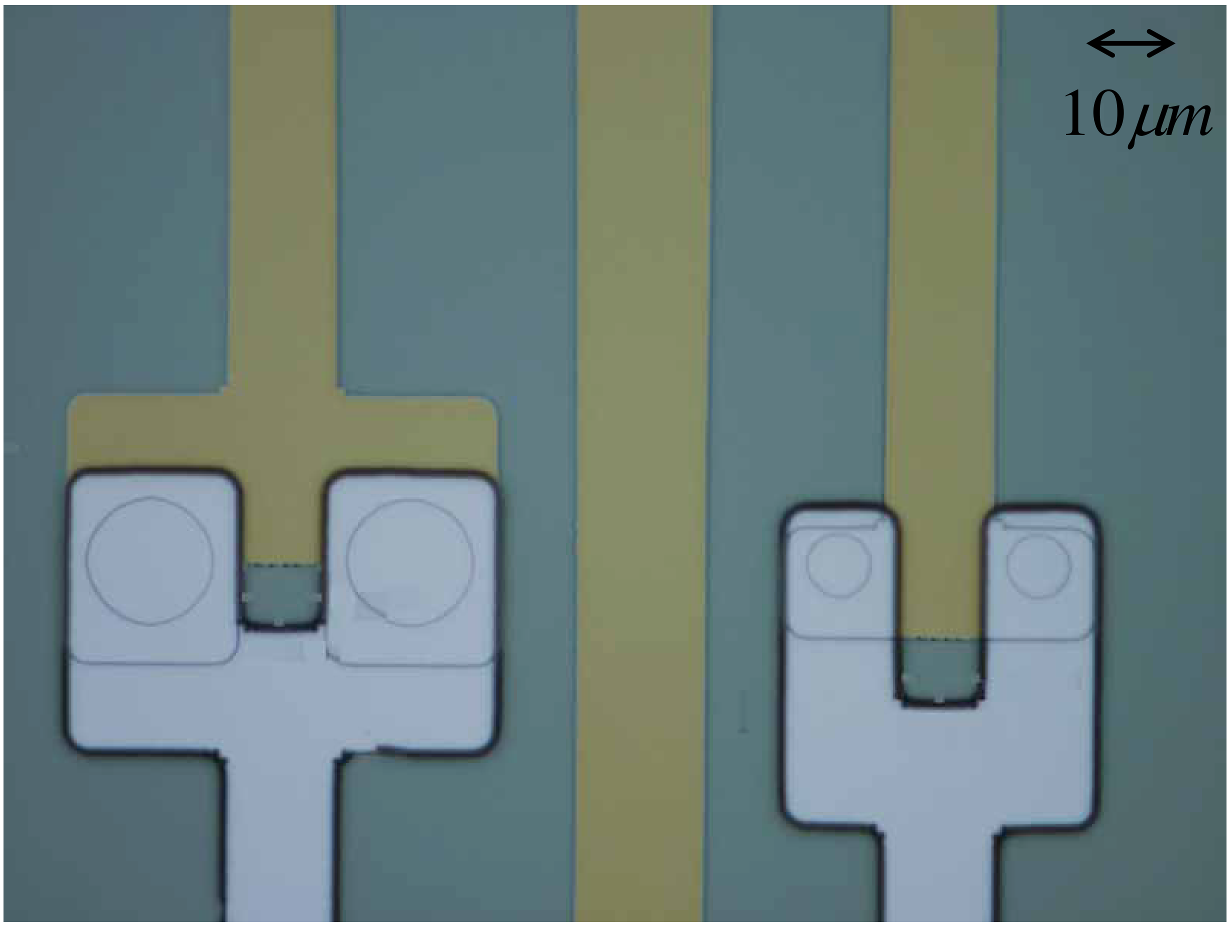

Figure 4.8: Zoom in image of one SQUID sample under optical microscope. The silver-colored fork-like features correspond to the top leads and the copper-colored fork-like features are the bottom multilayer under the SiOx. The middle straight line was used to generate the out-of-plane magnetic field.

4.2 Fabrication Issues

4.2.1 Growth of base Nb layer

Since we usually have 150nm Niobium as our base seeding layer, the following growth of multilayer magnetic thin films are affected by the surface morphology of it. There are many papers in the literature discussing the Nb growth parameters which might influence the final morphology, such as the substrate temperature, Ar pressure, deposition rate, etc. We tried two ways to improve the heat conducting efficiency, such as applying high vacuum grease to the back of our chips to increase the contact area and evaporating a thin layer of Au film at the back of our substrates. We also tried reducing the thickness of Nb to 100nm to cut the growth time, equivalently minimizing the heating issue. Even though all these efforts did not have any apparent effect on our final samples, one must keep in mind there are all kinds of possibilities which may affect our samples. We found one interesting recipe to get a smoother Nb base layer, which also generated different results from our traditional pure Nb base sample. This new base layer was made of Nb and Al stacks. In the following area dependence chapter, some more detailed description of the stack with AFM surface scan figures will be shown.

4.2.2 Undercut

As we already mentioned before, it was a very tricky step to obtain a proper and clean pillar. There is no universal recipe to fit all delicate requirements. Right now, our current one in the appendix works 100% for the similar base structure. Here we show one special case to demonstrate the problem of too much undercut. Here we still applied our successful recipe. We usually would have Cu[5nm]/Nb[20nm]/Au[15nm] as the protection layer for our bottom

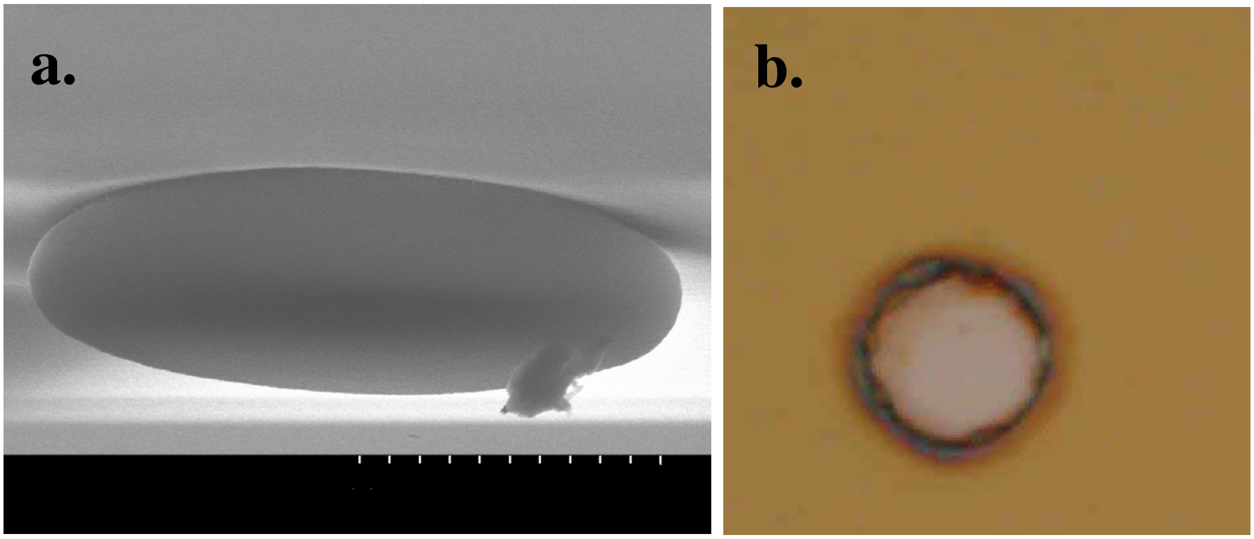

Figure 4.9: a.)One 6μm diameter sample with too much undercut. This figure was taken upside down right after the AZ5214E development. b.) Zoom in image of a corrupted 6μm pillar under optical microscope after SiOx deposition and the liftoff from the same run of Fig. a.)

multilayer structure to finish our run. The only thing different for the ruined ones shown in this section was that the we replaced our traditional Cu[5nm]/Nb[20nm]/Au[15nm] with Cu[5nm]/TiCu[Xnm]/Au[15nm].

As we can see from Fig. 4.9 , the resist wall of the AZ5214E pillar was not steep enough at the top, which might cause the hard time of the following liftoff of the SiOx. The dirty edge in Fig. 4.9.b) was found out to be the residue of SiOx as shown in SEM Fig. 4.10. Even though we tried to leave these samples in the ultrasonic bath longer, the liftoff process never turned out right. There could be two possible reasons for this problem. One might be due to the reflectivity altered by the missing Nb layer or the alloying between TiCu and Au. The other one might be due to the heat problem during the SiOx deposition, which could cause the melt-down of the resist because of the excessive undercut. Therefore, the lesson we learned here is that we should always do dose tests to make sure the recipe is compatible with the new case even though there might be just some tiny change with our samples.

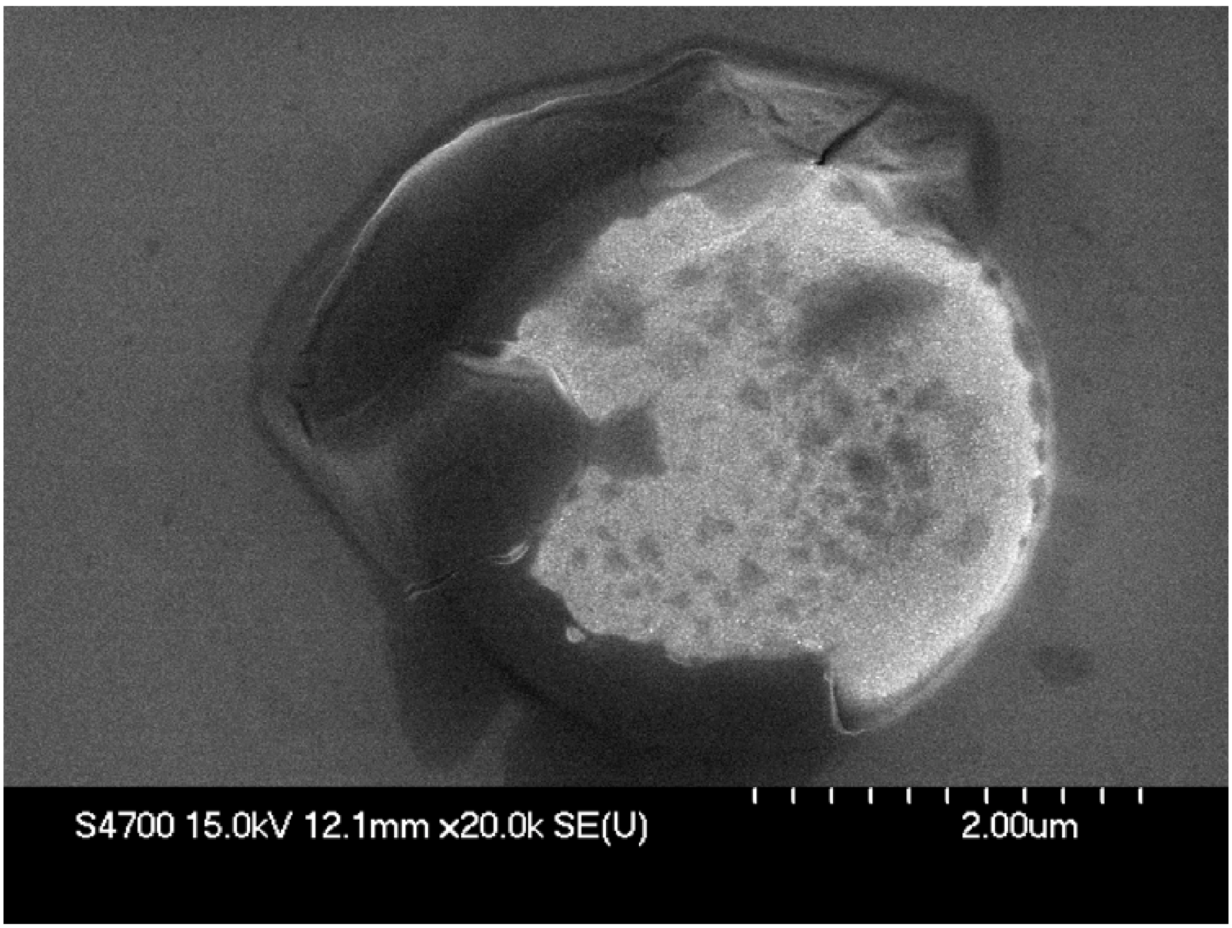

Figure 4.10: SEM image of one 3μm pillar after the SiOX liftoff.

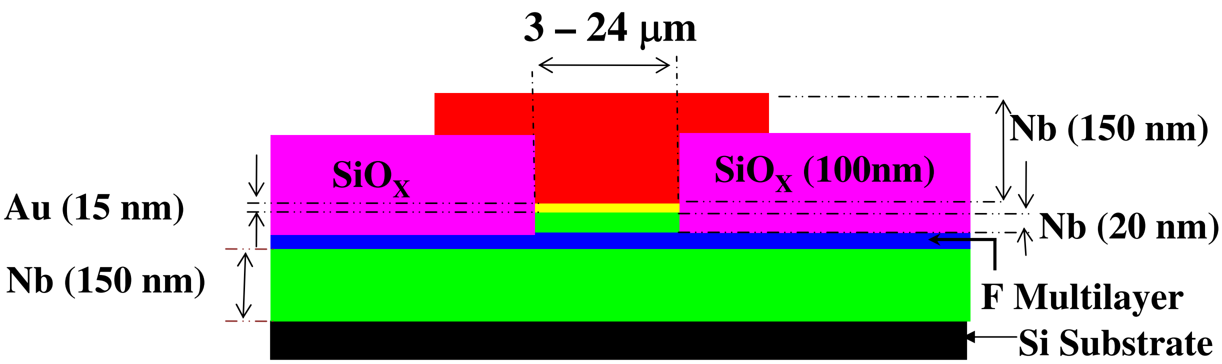

Figure 4.11: Schematic diagram of S/F/S Josephson junction cross section. Current flow is in the vertical direction inside the junction. Here we use the red and green colored Nb Layers to match the Fig. 4.12.

4.3 Measurements

After we do our final liftoff, the samples are ready to be tested. The cross section of a typical junction is shown in Fig. 4.11. The diameters for single Josephson junctions are 3,6,12 and 24μm. And the ones for SQUIDs are 6 and 12μm. Usually the ARn (product of area and normal state resistance) for our typical junctions is around 8 f $\Omega * m^2$. For SQUIDs, the ARn for an individual junction is in the range of 20-40 f $\Omega * m^2$ due to the contribution from the CuTi alloy. There are several ways to measure samples, such as differential measurements dV/dI, I-V scan with SQUID-based current comparator circuits and I-V fast scan with room temperature electronics. In most cases we obtained our data by using the I-V scan with the SQUID-based system. There was one exception. S/I/S samples have much higher ARn, which unlocked our SQUID circuits. In this case, we would have to use the I-V fast scan system with room temperature electronics.

The typical contact leads configuration corresponding to our different type samples is shown in Fig. 4.12. After taking into account the zero resistance property of superconducting Nb film, we can see that these are typical four probe measurement setups. Our sample is

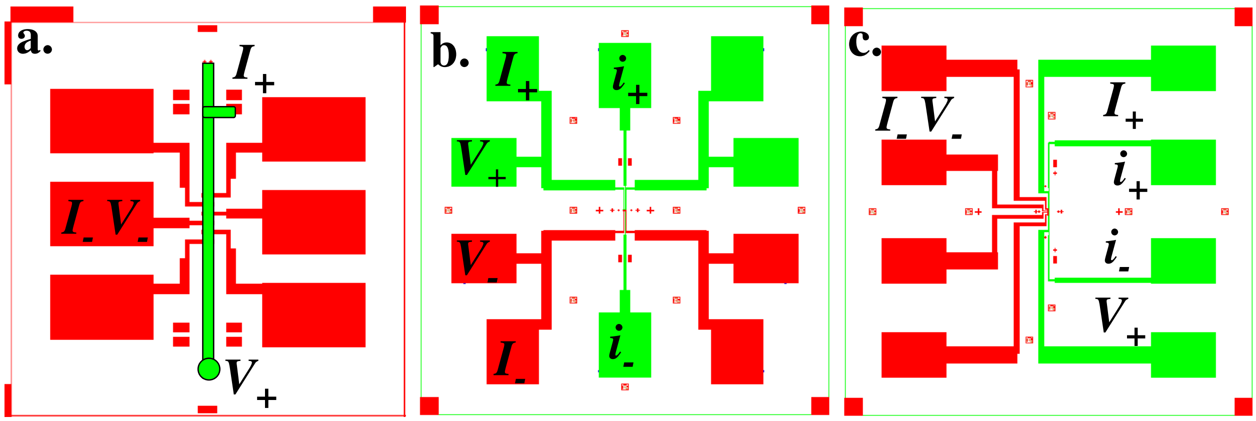

Figure 4.12: Example showing the contact leads on the real samples a.) Single Josephson junction. b.) and c.) SQUIDs

mounted on a Quick dipper probe, in which required leads, a superconducting magnet, a persistent switch and a SQUID detector are built. For our routine Fraunhofer pattern scan, an in-plane magnetic field is generated by the superconducting magnet. On the other hand, if we need to observe the modulation of our SQUID sample, an out-of-plane magnetic field will be provided by the on-chip strip wire by passing current through I_{M+} and I_{M-}.

4.3.1 SQUID-based electronics setup

The essential piece of our SQUID-based electronics setup relies on a current comparator module as shown in Fig. 4.13. Basically, the SQUID control electronics tries to maintain the flux inside the SQUID loop by outputting enough current to make sure no circulating current flows in the closed loop formed by the sample, the reference resistor and the coupling inductive wire. This implies that the voltage across the sample is equal to the voltage across the reference resistor. By ramping the current passing through the sample using a floating current source, we can switch the Josephson junction between the superconducting state and the normal state. At the same time, the output voltage of the SQUID electronics is recorded.

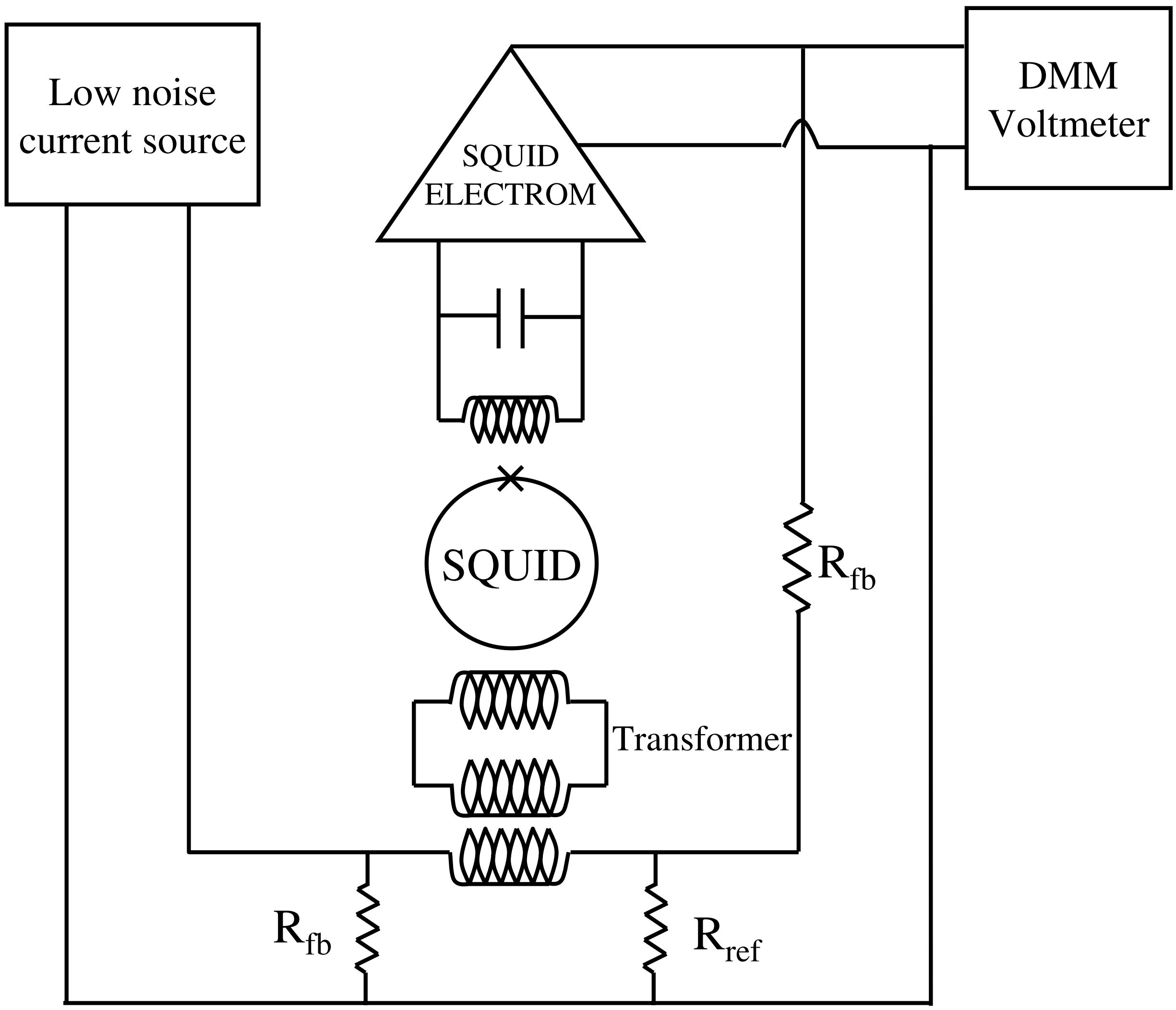

Figure 4.13: SQUID based current-comparator circuit used in our setup

Then we can calculate the voltage across the sample by the following relation,

$$V_S = V_{DMM}\frac{R_{ref}}{R_{ref}+R_{fb}}, \tag{4.1}$$

where R_{ref}=96$\mu\Omega$ (QD-1) or 126$\mu\Omega$ (QD-2) is the reference resistor, R_{fb}=10$k\Omega$ is the feedback resistor and V_{DMM} is the output voltage of the SQUID electronics recorded by the DMM. Since R_{fb} is much bigger than the R_{ref}, we can neglect the R_{ref} in the denominator.

This setup works perfectly for our single junctions and SQUIDs. The data collection program and processing program were coded in Labview by me. A few detailed flow diagrams of these programs can be found in the Appendix.

4.3.2 Room temperature-based electronics setup

In order to test out SIS junctions which have much larger resistance than S/F/S junctions, we set up a room-temperature based electronics system as shown in Fig. 4.14. A Stanford DS345 synthesized function generator provided a voltage across the sample R_s and ballast resistor R_b. The actual voltage across the sample and the one provide by the function generator were both recorded after proper amplification and signal filtering with a Labview program written by me. At the same time, a data processing plug-in program was also running to generate the final I-V data. This original data processing program coded in C++ was initially developed by Fred Pierre, which averaged several cycles together and generated evenly spaced points along the current axis. However this program was very hard to use and also assumed the system was working in the current source mode, which was not always correct for us. After I carefully studied the averaging algorithm of that C++ program, I wrote the Labview plug-in program which took account of all possible source modes and could automatically output the final file by getting various input parameters from the source file.

Input Parameters	Source Parameters
Gain Mes	(Gain from PreAmp * Gain from Filter)for Voltage Axis
Gain DC	Gain from Filter for Current Axis
Steps	Points along the final Current Axis
Cutting Level	Threshold level to reframe the current axis
Rb	Resistance of ballast resistor

Table 4.1: Parameters for Processing program of room temperature fraunhofer program.

Basically, there are two main averaging processes involved here in order to minimize the

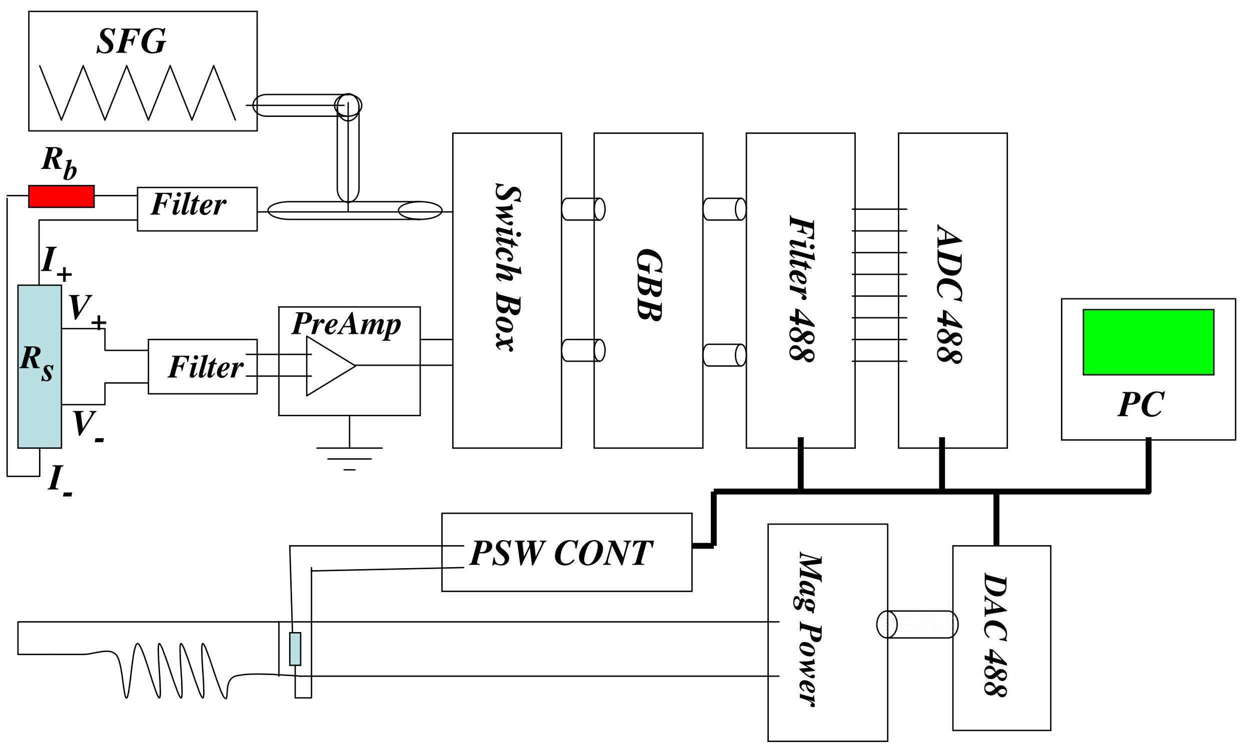

Figure 4.14: Diagram showing wiring configuration for the fast scan measurements. SFG represents the function generator; GBB represent the Ground breaking box; PSW CONT represents the persistent switch control box.

noise. One is the ensemble averaging, which is very similar to taking data N times to get the average value for a particular reading. At the same time, we know that the standard deviation of the mean of N measurements is smaller by a factor of $\sqrt{N}$ than the standard deviation of a single measurement. The only thing different here is that we collected many cycles' data and then average them by cycle. The other averaging process we use is boxcar averaging. It is assumed that the analog analytical signal varies only slowly with time and the average of a small number of adjacent points is a better measure of the signal than any of the individual points. In practice 2 to 50 points are averaged to generate a final point. Both averaging processes are performed by my plug-in program right after the data has been collected. Last but not least, we intentionally picked a sweep frequency of 3.2 Hz to reduce the noise from the power lines, which is a multiple of 60 Hz or 120 Hz. In this case, the 60Hz noise signal cancels every 4 cycles and the 120 Hz signal cancels every 2 cycles, which is also the reason we pick up 48 cycles. A similar description of the ensemble averaging and the scan frequency selection can be found in the dissertation of Dr. Mike Crosser.

Here is our case. We usually set the frequency of the function generator to 3.2Hz and scan 48 cycles, which means improves the original signal/noise ratio by a factor of $\sqrt{48}$. And we also set the ADC 488 to 10 KHz sampling rate. Therefore, for each raw scan we will have 150,000 current-voltage pairs shown by Equation 4.2. The number of data points in our final processed data are set to 500, which means that each final point is obtained by averaging the adjacent 6 points as shown by Equation 4.3.

$$Total\ samplings\ per\ scan = 10kHz \times \frac{48cycles}{3.2Hz} = 150k\ samples \tag{4.2}$$

$$Points\ per\ boxcar\ averaging = \frac{Total\ samplings\ per\ scan}{500 * 48cycles} \approx 6\ points \tag{4.3}$$

We just mention one more thing to close this chapter. Each raw data file for 150,000 current-voltage pairs takes about 2.58MB storage. And if we scan a full Fraunhofer pattern with 60 points, it will take about 155MB. Therefore, data storage is one main drawback of this fast scan system.

Chapter 5

Interpretation of distortion of Fraunhofer patterns and enhancement of critical current

Very convincing evidence for the spin-triplet correlations has been confirmed by several groups around the world [34, 62, 2, 57], including our group. We measured the critical current I_C in Josephson junctions with the structure Nb/F$'$/SAF/F$''$/Nb, where SAF stands for "synthetic antiferromagnet" and F$'$ and F$''$ are thin ferromagnetic layers. The critical current only provides information about the amplitude behavior of the spin-triplet supercurrent. However, the phase across the junctions was still a very intriguing problem. Several theoretical works [9, 70, 31, 68] suggested that the junctions could be either 0 or π junctions, depending on the chirality of the successive magnetic moments in the junction. In the π junction, the current reverses its direction with respect to the phase difference between the two superconducting electrodes, which is equivalent to the introduction of an extra π phase factor in the Josephson supercurrent-phase relation. In traditional Josephson junctions, 0 junctions are very common. It is relatively easy to modulate between the 0 and π junction in a spin-triplet S/F/S, which is not only of theoretical importance but also is crucial from the application perspective. In this chapter and the next two chapters, we will try to unveil this problem.

5.1 Introduction to spin-triplet Nb/F′/SAF/F″/Nb Josephson junctions

We introduce some experimental background of our spin-triplet S/F′/SAF/F″/S Josephson junctions, most of which can be found in our previous publications [35, 73]. A cross section of our samples is shown in Fig. 5.1. In order to keep the magnetic layers intact, we stop ion milling between the bottom of the 20nm Nb and the bottom of the top 5nm Cu layer.

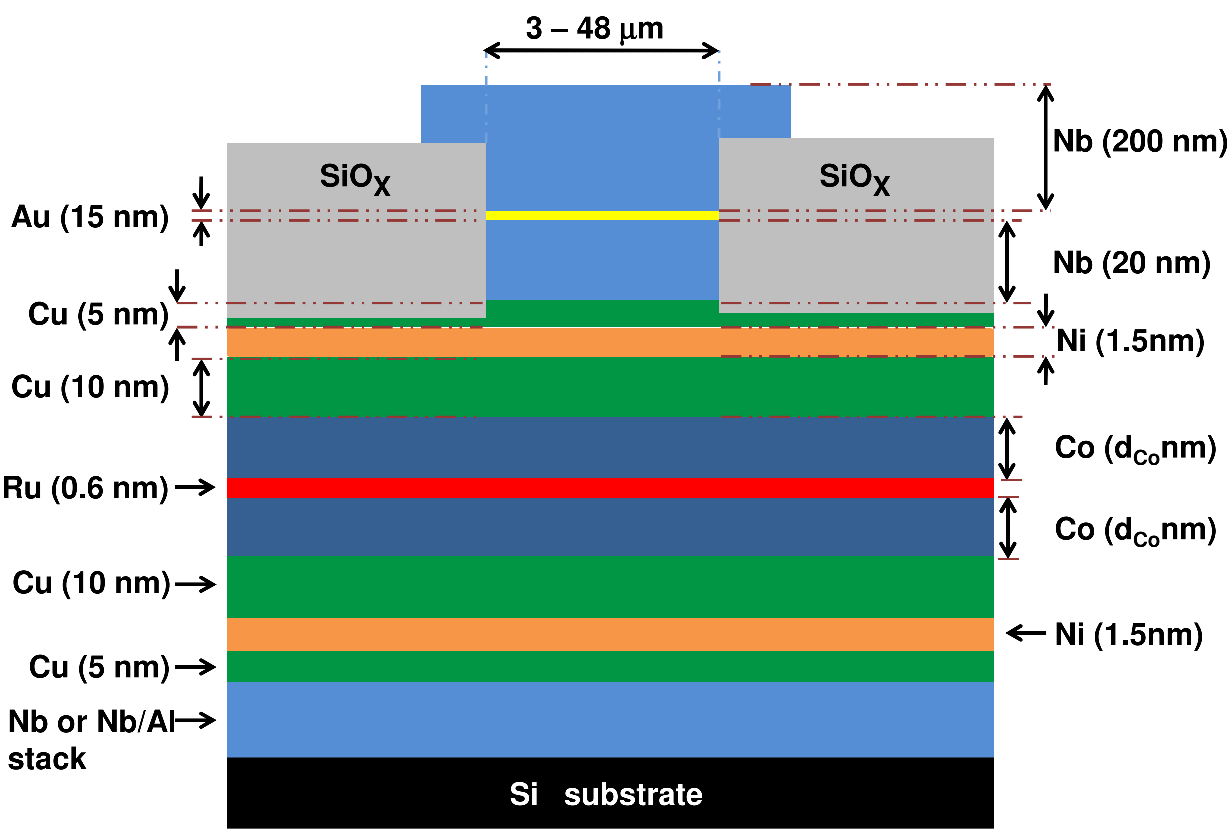

Figure 5.1: Schematic diagram of Josephson junctions. The Cu buffer layers provide the seeding layers for the growth of Ni and Co and also play an important role to decouple the Ni layers from Co layers magnetically.

In Fig. 5.2 a) and b), we show the two voltage-current curves for a $3\mu m$ diameter spin-triplet Josephson junction with $d_{Co} = 6nm$, respectively at in-plane field $H = 0Oe$ and $H = -100Oe$ provided by the superconducting coil on our quick-dipper. All these data were taken at 4.2K inside the liquid Helium. As we can see here clearly, the critical current of Josephson junctions depends on the magnetic flux going through the junctions. After we took a full critical current vs in-plane magnetic field scan, we could get a Fraunhofer pattern as shown in Fig. 5.2 c), from which we could easily read the maximum critical current.

We determined the normal state resistance for a junction from the slope of the V-I curve for $I >> I_C$. Sometimes in order to do this, we applied a relatively high in-plane field, such as $400Oe$, to get I_C close enough to zero and to make the V-I curve as straight as possible. The product $I_C R_N$ of the normal state resistance R_N and the maximum critical current I_C is the most important parameter from which we can tell whether junctions are spin-singlet or spin-triplet. Figure 5.3 shows $I_C R_N$ for several types of junctions, versus total cobalt thickness. We can see clearly here that the decay of the $I_C R_N$ for samples with F$'$ and F$''$ is very slow compared to the decay for samples without F$'$ and F$''$. This is the hard evidence for the spin-triplet correlation. We also observed that the data for samples with Ni were more scattered compared with others. We will discuss this in the following sections.

We just mention one more thing to end this section. All the above results come from samples with one crucial center piece- the SAF. Recently, we replaced the SAF with a Ni/[Co/Ni](n) multilayer with out-of-plane magnetization and we also observed the spin-triplet Josephson current [26].

5.2 Theoretical background of the phase of long-range spin-triplet Josephson junctions

Since our long-range spin-triplet Josephson junctions are multilayered ferromagnetic structures, the Cooper pairs will definitely obtain center-of-mass momentum Q, which in turn will result in the phase shift. Even the earlier theoretical works [9, 70, 31] already pointed out that the different magnetic configuration determines whether the ground state of the system is $0-state$ or $\pi-state$. In 2010, Trifunovic et al. [68] studied our work [34] and calculated the pair amplitudes by using a full self-consistent numerical solution of the Eilenberger equations. Their results also demonstrated that the ground state of our Josephson junctions shown in Fig. 5.4 is $0-state$ for anti-parallel magnetizations in the two Ni layers and that the ground state for the case with parallel magnetizations in the two Ni layers is $\pi-state$.

If we stick with the similar simple argument in Section. 2.3.2, we also can come to the same conclusion. We will discuss this problem using the schematic shown in Fig. 5.5.

After the spin-singlet Cooper pair goes through the top Ni layer NiT, it can develop into two short-ranged components as depicted in Eqn. 5.1.

$$\begin{aligned}
|\chi>_a &= \frac{1}{\sqrt{2}}[|\uparrow\downarrow>_{NiT}\exp(iQt_{NiT}) - |\downarrow\uparrow>_{NiT}\exp(-iQt_{NiT})] \\
&= |0,0>_{NiT}\cos(Qt_{NiT}) + i|1,0>_{NiT}\sin(Qt_{NiT}) \qquad (5.1)
\end{aligned}$$

Since the short-ranged spin-singlet $|0,0>_{NiT}$ will decay even more in the following Co layer CoT, we can neglect it. On the other hand, the short-ranged spin-triplet $|1,0>_{NiT}$

will evolve into three components shown in Eqn. 5.2.

$$|\chi>_b = i\sin(Qt_{NiT})(-\frac{1}{\sqrt{2}}|1,1>_{CoT}\sin\theta_1 + |1,0>_{CoT}\cos\theta_1 + \frac{1}{\sqrt{2}}|1,-1>_{CoT}\sin\theta_1) \tag{5.2}$$

We further assume that the decay coefficient for majority band is α and that the decay coefficient for minority band is β. Similarly, the short-ranged spin-triplet $|1,0>_{CoT}$ will decay very quickly in the Co layer. Therefore, we can neglect $|1,0>_{CoT}$. After the two long-ranged spin-triplet components go through the top Co layer, we can get

$$|\chi>_c = i\sin(Qt_{NiT})(-\frac{\alpha}{\sqrt{2}}|1,1>_{CoT} + \frac{\beta}{\sqrt{2}}|1,-1>_{CoT})\sin\theta_1 \tag{5.3}$$

Since the majority band of the top Co layer Co_T corresponds to the minority band of the bottom Co layer Co_B, and vis-a-vis for the minority band of the top Co layer:

$$|\chi>_d = i\sin(Qt_{NiT})(-\frac{\alpha}{\sqrt{2}}|1,-1>_{CoB} + \frac{\beta}{\sqrt{2}}|1,1>_{CoB})\sin\theta_1 \tag{5.4}$$

After taking into account the further decay in the bottom Co layer, we can get

$$\begin{aligned} |\chi>_e &= i\sin(Qt_{NiT})(-\frac{\alpha\beta}{\sqrt{2}}|1,-1>_{CoB} + \frac{\beta\alpha}{\sqrt{2}}|1,1>_{CoB})\sin\theta_1 \\ &= i\frac{\alpha\beta\sin(Qt_{NiT})}{\sqrt{2}}(-|1,1>_{CoT} + |1,-1>_{CoT})\sin\theta_1 \end{aligned} \tag{5.5}$$

When the electrons encounter the bottom interface between Co and Ni, they undergo another rotation and develop into

$$|\chi>_f = i\frac{\alpha\beta\sin(Qt_{NiT})}{\sqrt{2}}(-\cos\theta_2|1,1>_{NiB} - \sqrt{2}\sin\theta_2|1,0>_{NiB} + \cos\theta_2|1,-1>_{NiB})\sin\theta_1 \tag{5.6}$$

Since long-ranged spin-triplet electron pairs $|1,\pm 1>$ would not be able to converted into spin-singlet Cooper pairs $|0,0>$, we can neglect them to simplify the math. After taking into account the exchange field influence on the short-ranged spin-triplet $|1,0>$ electron pairs, we can obtain

$$\begin{aligned}|\chi>_g &= -i\frac{\alpha\beta\sin(Qt_{NiT})}{\sqrt{2}}(|\uparrow\downarrow>_{NiB}\exp(iQt_{NiB}) + |\downarrow\uparrow>_{NiB}\exp(-iQt_{NiB}))\sin\theta_1\sin\theta_2 \\ &= -i\alpha\beta\sin(Qt_{NiT})(|1,0>_{NiB}\cos(Qt_{NiB}) + i|0,0>_{NiB}\sin(Qt_{NiB}))\sin\theta_1\sin\theta_2\end{aligned} \tag{5.7}$$

Finally, Cooper pairs reach the other-side of Josephson junctions,

$$|\chi>_h = \alpha\beta\sin(Qt_{NiT})\sin(Qt_{NiB})\sin\theta_1\sin\theta_2|0,0> \tag{5.8}$$

Let us treat the simplest case as shown in Fig. 5.4. For the case in Fig. 5.4.(a) where $\theta_1 = \pi/2$ and $\theta_2 = -\pi/2$, $\sin\theta_1\sin\theta_2$=-1 corresponding to a π-state. For the case in Fig. 5.4.(b) where $\theta_1 = -\pi/2$ and $\theta_2 = -\pi/2$, $\sin\theta_1\sin\theta_2$=1 corresponding to a 0-state.

Since our junctions consist of multiple domains in the virgin state, they should contain a mixture of 0 and π subjunctions, shown in Fig. 5.6. It means that the total critical current of the junction would be proportional to the square root of the the number of domains in a junction according to a random walk model. Since the number of domains is proportional to the area of the junction, the total critical current of the junction would be proportional to the square root of the area. This contradicts the traditional junction critical current which is proportional to the area. After we fully magnetize the same junction with a large enough in-plane field, the magnetizations of the two Ni layers are parallel to each other and the $\pi - state$ coupling would dominate across the whole junction. In this later case, the critical current will be proportional to the junction area, similar to a traditional Josephson junction. This issue was also our initial motivation to study the phase problem.

5.3 First indirect phase indication: critical current enhancement

What will happen for ferromagnetic Josephson junctions if we magnetize them by applying a large enough in-plane field? Let's take a look at the spin-singlet case made of our "synthetic antiferromagnet" without the two extra thin ferromagnetic layers. We show the virgin state and magnetized state Fraunhofer patterns in Fig. 5.7, for a 10-μm-diameter Josephson junction of the form Nb(150)/Cu(5)/Co(10)/Ru(0.6)/Co(10)/Cu(5)/Nb(25)/Au(15)/Nb(150), where all thickness are in nm. There is not much difference between the virgin and the magnetized states.

For spin-singlet Josephson junctions of the form Nb/PdNi/Nb, made of weekly ferromagnetic alloy $Pd_{82}Ni_{12}$, Dr. Khaire also observed similar results [40]. There is no obvious change of critical current, even though the center of the Fraunhofer pattern shifted to a field of around -160 Oe for a sample with $d_{PdNi} = 47.5nm$ and diameter equal to $10\mu m$.

After we inserted the two very thin layer 1.5nm Ni layers, the first thing we noticed was that the critical current of the samples increased several decades higher compared with those without thin Ni layers. And we also noticed that the critical current changed from run to run and varied from sample to sample in the as-grown state as we shown in Fig. 5.3. But after we applied a high enough in-plane field, we not only obtained much better shaped Fraunhofer pattern but also enhanced the critical current several times as shown in Fig. 5.8. At the same time, the center peak of the Fraunhofer patterns in the magnetized state were shifted to a negative field by about 30 Oe, where the external applied flux exactly cancels the intrinsic magnetic flux from the Ni layers.

As we can see, there was not too much change in the Fraunhofer patterns of the Co/Ru/Co SAF spin-singlet Josephson junction before and after the high-field in-plane magnetization. Therefore, we believe that it is more likely that the reorientation of the magnetic moments of the 1.5nm Ni F$'$ and F$''$ layers contributed to the final well-shaped Fraunhofer pattern.

To explain the I_C enhancement, we need to introduce the spin-flop concept [35, 73]. In the virgin state, the two Co layers are anti-ferromagnetically exchange coupled to each other through the 0.6nm Ru while pointing in all possible directions in the plane. After we applied a high enough in-plane magnetic field, the two Co layers would be roughly aligned parallel to the external field direction. However, the two Co layers would never recover to the original state after we remove the field. Instead, they would scissor to the direction perpendicular to the external field while maintaining anti-ferromagnetic coupling.

As we already mentioned in the theory introduction, the phase of the junctions depends on the relative orientations of the multi-ferromagnetic layers. The situation can be illustrated in Fig. 5.10 .

When the samples were in the as-grown state, the phase fluctuation between 0 and π of the sub-junctions across one Josephson junction was totally random since the junction consisted of randomly distributed magnetic domains. In this case, if we applied a fixed gauge-invariant phase difference across the junction, some portion of the junction would provide positive current while others would provide negative current. Then it is apparent that the critical currents of these sub-junction would cancel one another. If we naively applied the random-walk model to our case, the typical supercurrent in a given sample would be proportional to the square root of the number of the domains, hence to the square root of the junctions. On the other hand, after we magnetized our sample, we would expect the π phase to be dominant across the junction since the magnetizations of the Ni F′ and F′′ were parallel to each other, which meant the θ_1 and θ_2 in Fig. 5.10 had the same sign. In this case, the critical current for the whole junction would be proportional to the junction area.

The evolution of I_c as the sample is magnetized is shown for a 6-μm diameter Josephson junction in Fig. 5.11.a). And we also show the magnetization of a Cu(5nm)/Ni(1.5nm) multilayer in Fig. 5.11.b). The sample was first measured in the as-grown state (H = 0). Then the magnetizing field H was stepped up to 3600 Oe with varying step sizes evident in the figure. After application of each value of H, the field is reduced to zero and the Fraunhofer pattern is measured in low field. The squares show the resulting values of I_cR_N as the sample is magnetized. For low fields, nothing happens, which might mean the magnetization process is still reversible. Then there is a shallow dip in I_cR_N for H near 500 Oe, which corresponds to the turning point on the M-H curve in Fig. 5.11.b), which may be related to a change of the Ni domain structure. When H is increased above 500 Oe, I_c increases sharply. The field range where I_c increases corresponds to the field range where the Ni films become magnetized, which matches the coercive field of the Ni as shown in Fig. 5.11.b). In Fig. 5.11.a), we also show what happens when a field is applied in the opposite direction to the original magnetizing field (circles). Again, nothing happens for small field values. Then, as the Ni films are demagnetized, I_c drops to values as low as or even lower than the value at the dip we observed when first magnetizing the samples. As the Ni films are re-magnetized in the negative direction, I_c increases sharply again to a value essentially identical with that observed on the positive field side. We have measured full magnetization curves for several samples, and they all look very similar to the one shown in Fig. 5.11.a).

What would happen if we demagnetize samples with an oscillatory decaying in-plane field as shown in Fig. 5.12 after we fully magnetize them? Here is what we did. We first magnetized our samples with an in-plane field of 2000 Oe and then reduced the field to zero. Then we measured our traditional Fraunhofer pattern in low field. Then we applied one oscillatory decaying in-plane field to demagnetize the sample as shown in Fig. 5.12 with A_{Dem} stepping up from 0 Oe to 1200 Oe. After each demagnetization, we took one Fraunhofer patten. Three typical Fraunhofer patterns representing the initial, mid and final stage respectively are shown in Fig. 5.13.

After we took the Fraunhofer patterns for all the oscillatory-decay demagnetization fields, we obtained $I_C R_N$ vs A_{Dem} in Fig. 5.14.a). And we also show in Fig. 5.14.b) the corresponding field shift of the center peak for each Fraunhofer pattern. Since there was no obvious peak for the Fraunhofer with $A_{Dem} = 1200Oe$, we just set it to zero.

As we can see here, the product $I_C R_N$ decreased by a factor of 20 relative to the value in the "fully-magnetized" state, which also gave us the explanation why sometimes we observed the critical current enhanced up to a factor of 20 compared with its value in the as-grown state [35].

The most important thing we found out here is the modulation of the critical current in our junctions by the external in-plane field, no matter whether we magnetized or demagnetized our samples.

5.4 Discussion of distortion of Fraunhofer patterns

In order to understand the relationship between magnetic states and the quality of Fraunhfer patterns, we first take a look at the spin-singlet case, as shown in Fig. 5.7 for junctions containing the SAF center piece, and Fig. 5.15 for junctions of the form Nb/Ni/Nb. As we can see, there is clearly a sharp contrast between these two types of ferromagnetic spin-singlet Josephson junctions. At the same time, it is well known and has been discussed in Section 3.1 that the general expression for Josephson current density $J(\mathbf{x,y})$ in a Josephson junction is related to the gauge invariant phase difference φ through $J(\mathbf{x,y}) = J_C sin(\varphi)$, where $\varphi = \Delta\theta - (q^*/\hbar)\int \mathbf{A(x,y)dl}$. And the total critical current I_s is equal to $\int J(\mathbf{x,y})dxdy$.

In any real sample with large area, there are many magnetic domains across the junctions. These randomly distributed magnetic domains modulate the local magnetic magnetic field $\mathbf{B(x,y)}$. This means the local vector potential is also tuned by the local magnetic domains indirectly since $\mathbf{B(x,y)} = \nabla \times \mathbf{A(x,y)}$. And for our SAF case, we definitely can get much nicer Fraunhofer patterns since we engineer the two Co layers to get zero local magnetic flux from the magnetization. Yet for a strong ferromagnetic material like Ni or Co not incorporated into a SAF, the distortion of Fraunhofer patterns is almost unavoidable, because of the presence of the randomly oriented magnetic flux due to randomly distributed magnetic domains. Dr. Khaire et al. discussed four ways to avoid the distortion of the Fraunhofer pattern [40]. Obviously we now know for sure that the carefully engineered SAF is a good option. Another way is to work with materials with weak magnetization such as PdNi, in order to minimize the local magnetic flux contributed by randomly distributed magnetic domains. As shown in Fig. Allfraunhofers, Dr. Khaire obtained clean Fraunhofer patterns for Josephson junctions of the form Nb/PdNi/Nb with different thickness of PdNi [40].

Yet there is an alternative explanation for the distortion of Fraunhofer patterns. Let us review some results from previous literatures [40, 38]. As we mentioned in the theory introduction chapter, the phase of the spin-singlet Josephson junctions can be controlled by the thickness of the magnetic layer. In other words, the proximity effect in a ferromagnetic layer can lead to a damped oscillation of the superconducting order parameter in the F-layers. Kemmler et al. [38] studied the most well controlled case with 0-π Josephson junctions, by putting a 0 junction and π junction side by side in one single junction as shown in Fig. kemmerlerzeropi.And the corresponding experimental Fraunhofer patterns were also shown in Fig. kemmerlerzeropiJJ for single phase junctions and for 0-π junctions. It was very obvious that Kemmler etc. found the double peaks in the junctions with two different phase sub-junctions.

Dr. Khaire in our group also observed similar results. For her Nb/PdNi/Nb Josephson junctions, she observed clearly single peaks for junctions with various thickness as shown in Allfraunhofers. It is because the oscillation period for PdNi is around 4.2nm [40]. Therefore, the junctions were all single phase ones.

On the other hand, Dr. Khaire also found some very "messy" Fraunhofer patterns for the Nb/Ni/Nb junctions [40], in the virgin state and magnetized state. The reason for this observation on Ni Josephson junctions is that the very short oscillation period for Ni results in the 0 and π sub-junctions randomly distributed across the whole junction, no matter whether it is magnetized or not.

The reason I favor this alternative explanation is that Dr. Khaire did not get undistorted Fraunhofer patterns even after she fully magnetized her Nb/Ni/Nb junctions. And I would like to mention one more comment on the SAF spin-singlet Josephson junction systems. We all know that Co is a strong magnetic material. Why did the SAF junctions not show distorted Fraunhofer patterns in the as-grown state and the magnetized state? The reason is also pretty straightforward. As we know, Cooper pairs would gain one positive center-of-mass momentum **Q** which in turn causes the phase shift $\delta\phi_1 = Qd_1^{Co}$ in the first Co layer. However, the same Cooper pairs would obtain one negative center-of-mass momentum **-Q** in the second layer giving the phase shift $\delta\phi_2 = -Qd_2^{Co}$. Therefore in sum there is not any phase shift and also no gain in center momentum, which means there would not be any damped oscillatory order parameter [11]. Then one uniform phase across the SAF type Josephson junction will be the case no matter whether it is in the as-grown state or in the magnetized state.

Even though the mechanism of the phase control in spin-triplet Josephson junctions is different from the one in spin-singlet Josephson junctions, the concept of 0 and π still can be applied with spin-triplet Josephson junctions. Regarding our spin-triplet Josephson junctions, we can now see easily that the "poor" quality of final Fraunhofer patterns in the as-grown state can be associated with the mixture of 0 and π sub-junctions. However in the magnetized state, we can regain nice single peak Fraunhofer patterns because one uniform phase dominates across junctions.

The biggest difference between spin-triplet Josephson junctions and spin-singlet Josephson junctions is whether it is possible to recover neat Frauhofer patterns and to observe the enhancement of critical current after fully magnetizing the samples. The phases of spin-singlet junctions are predetermined by the thickness of local magnetic film instead of magnetization. On the other hand, the phases across the spin-triplet junctions are determined by the magnetization, which give us the extra freedom over the control of phase.

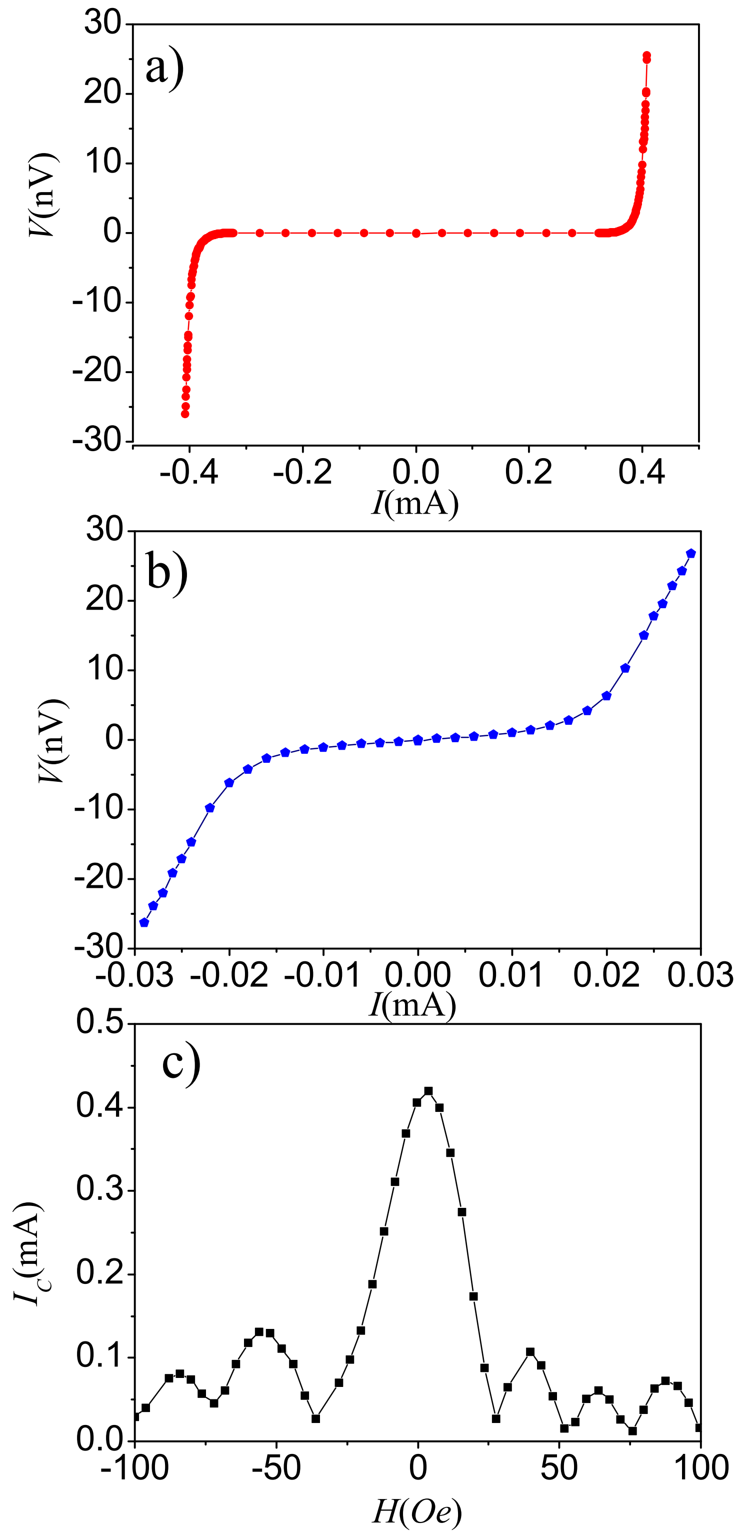

Figure 5.2: a) and b) are two voltage-current V-I curves for a $3\mu m$ diameter spin-triplet Josephson junction with $d_{Co} = 6nm$, respectively at in-plane field $H = 0Oe$ and $H = -100Oe$. c) Critical current (I_C) vs applied in-plane field (H) (Fraunhofer pattern) for the same junction in the as-grown state. The solid lines are just guides for the eye.

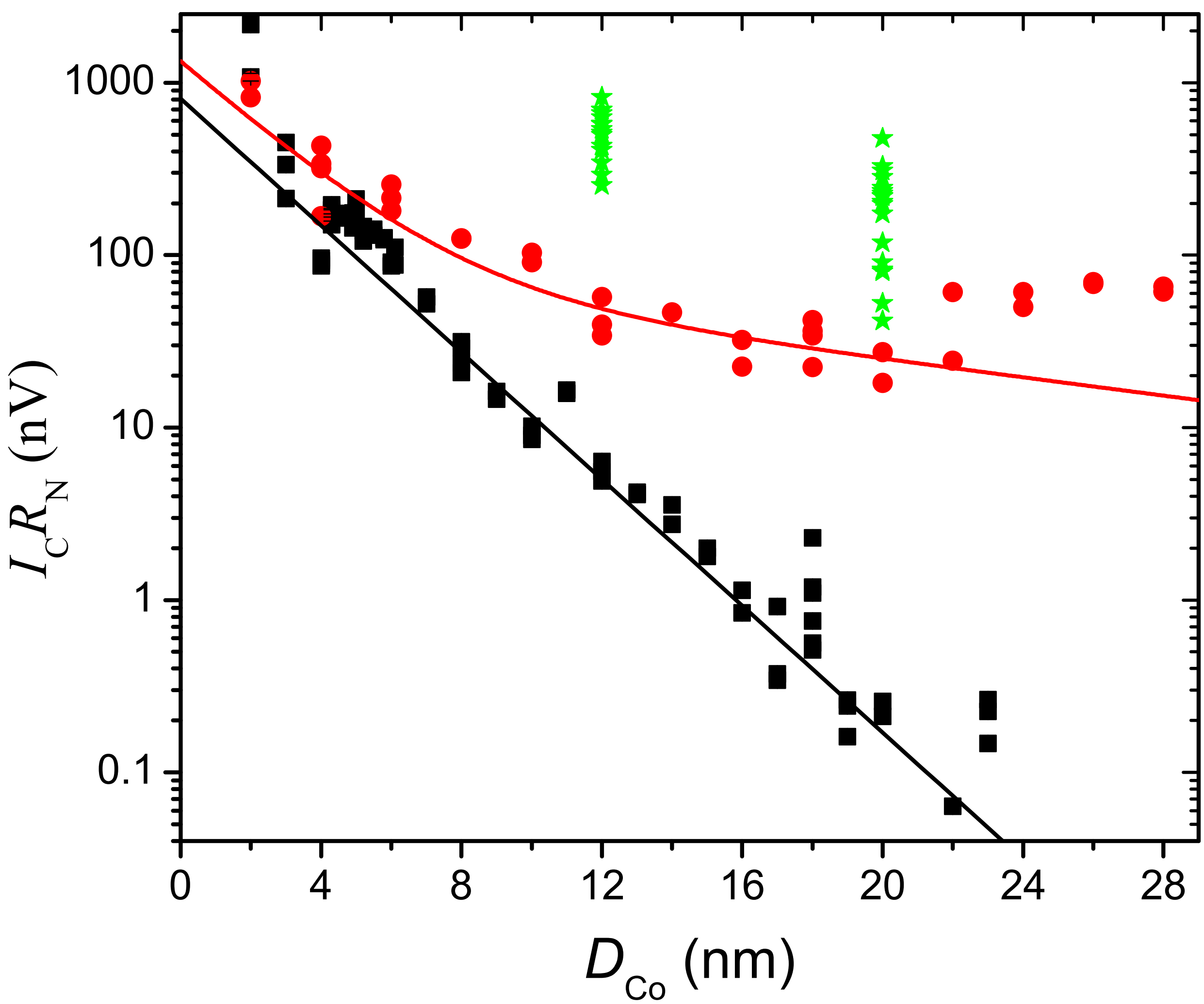

Figure 5.3: The product $R_N I_C$ of the normal state resistance R_N and the maximum critical current I_C vs total cobalt thickness ($D_{Co} = 2d_{Co}$) in the as-grown state. Red circles are samples having F′ and F″ =PdNi with $d_{PdNi} = 4nm$, green stars are those having F′ and F″ =Ni with $d_{Ni} = 1.5nm$, while black squares are those with only SAF. The black solid line is a fit to $Aexp(-D_{Co}/\xi)$, with $\xi = 2.3nm$. And the red solid line is a fit to $A_1 exp(-D_{Co}/\xi_1) + A_2 exp(-D_{Co}/\xi_2)$, with $\xi_1 = 2.4 \pm 0.7nm$ and $\xi_2 = 16.5 \pm 2.2nm$. Red-circle and black-square data were taken by Dr. Khaire and Dr. Khasawneh respectively [34]. The green-star data were collected by me from samples in the as-grown state.

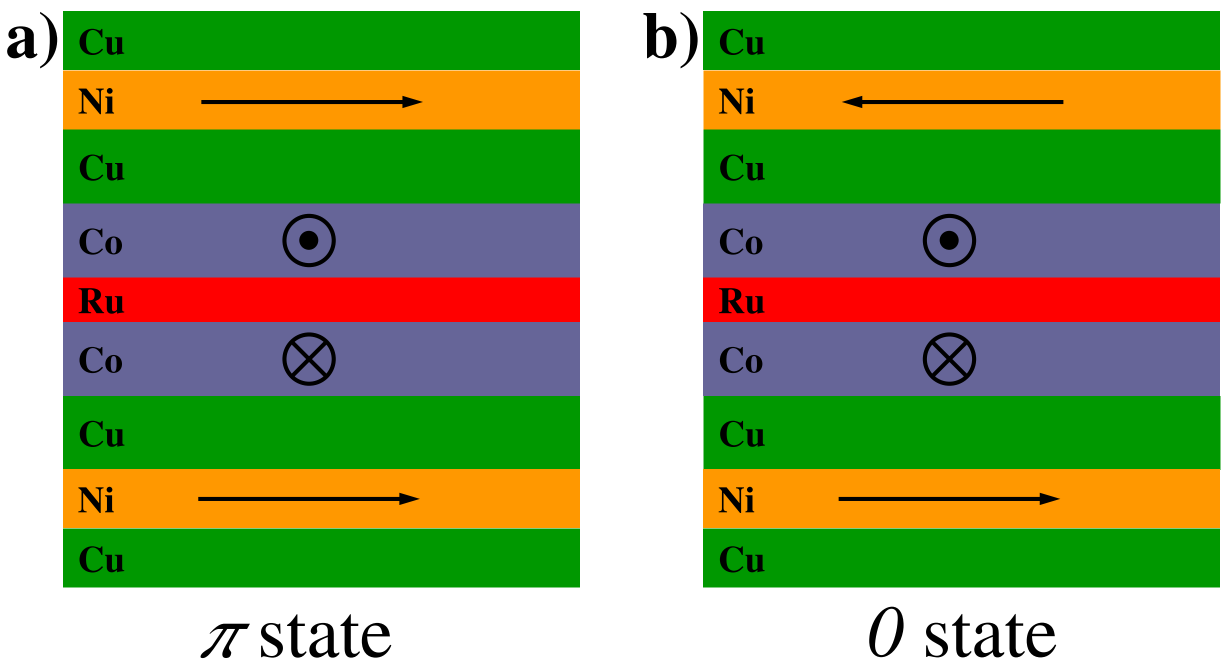

Figure 5.4: The phase of the long-range spin-triplet Josephson junction can be tuned by the relative orientation of magnetizations of the two Ni layers. a) The ground state for parallel magnetizations in the two Ni corresponds to $\pi - state$. b)On the other hand, the $0 - state$ is the case when the magnetizations of the two Ni layers are anti-parallel.

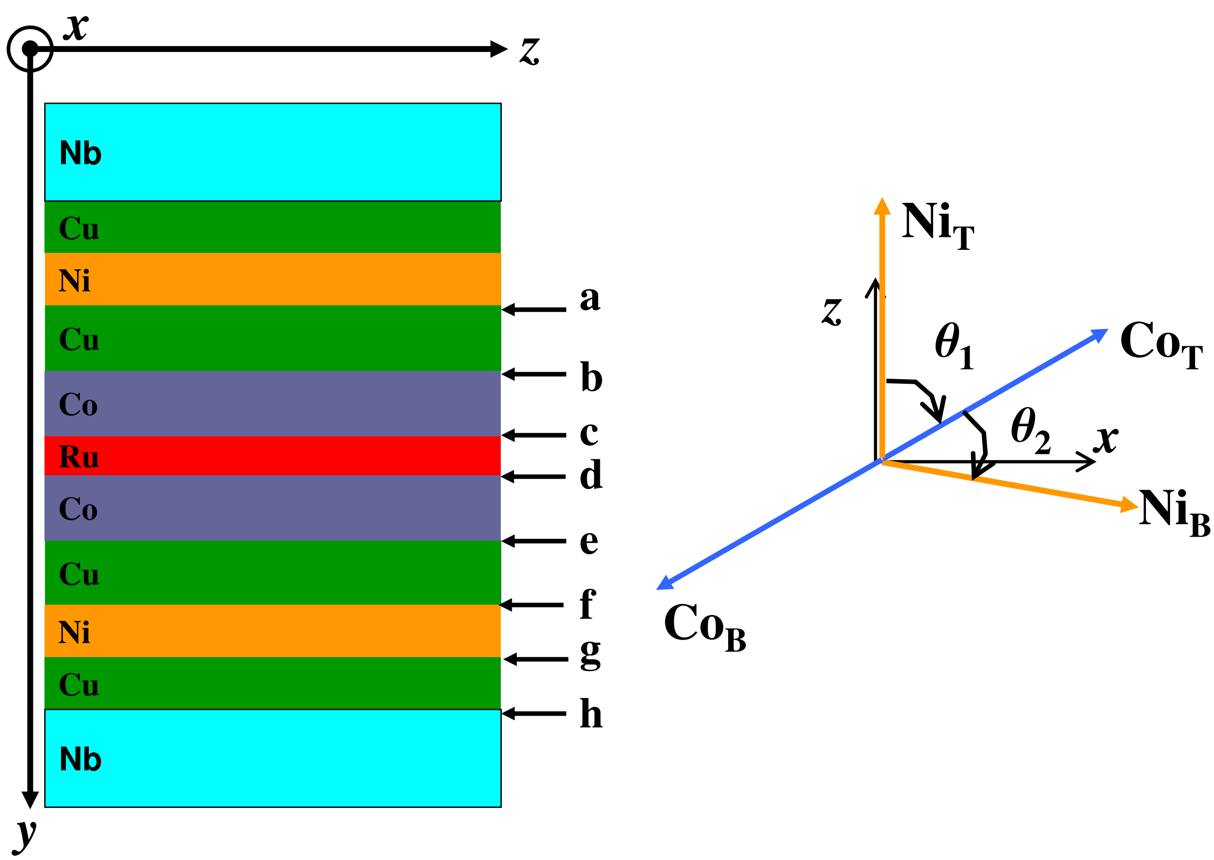

Figure 5.5: Left: Schematic diagram of Josephson junction showing the different layer stacked along the y axis; Right: Magnetizations of different magnetic layers, where we define the clockwise rotation is position. And all the magnetizations are in the x-z plane.

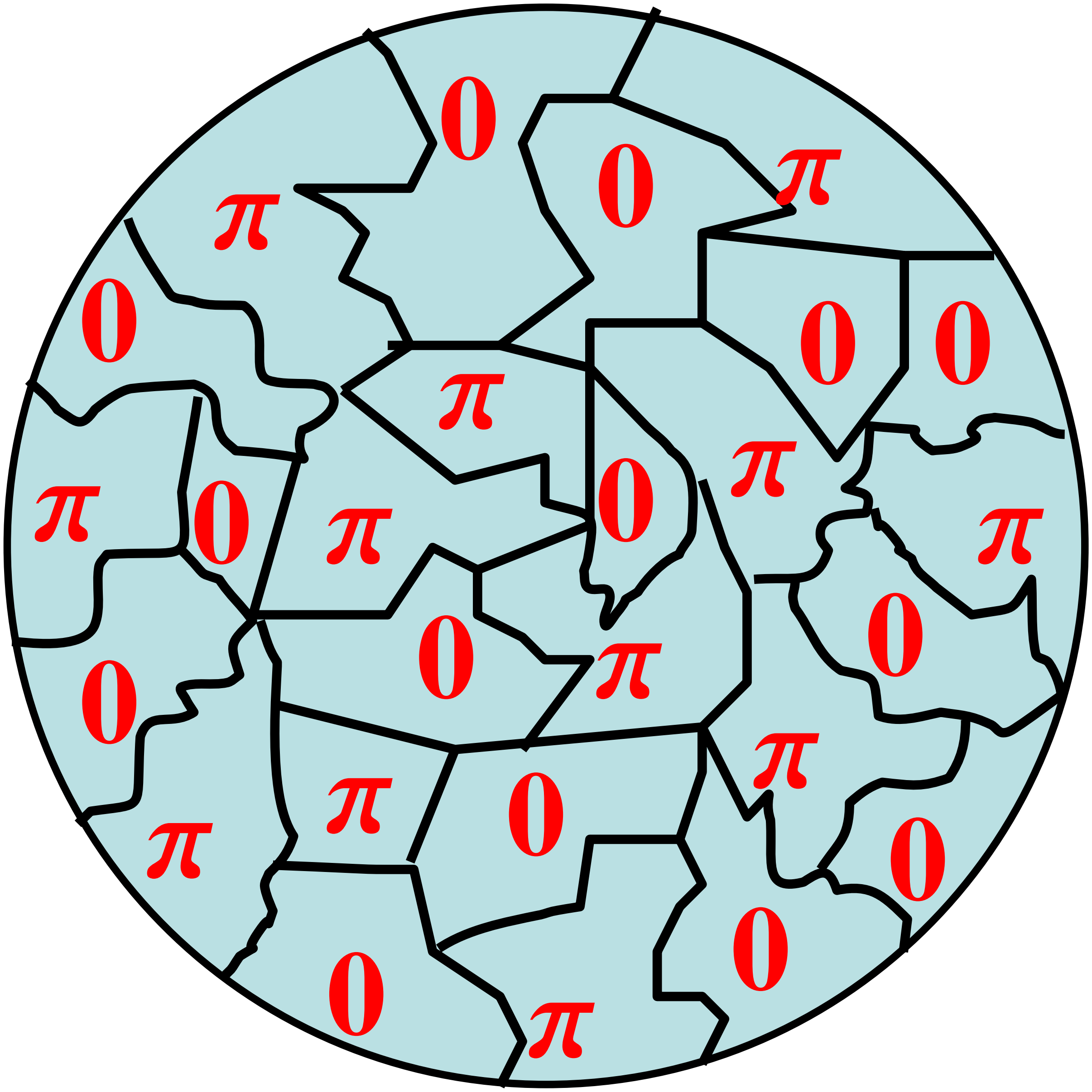

Figure 5.6: A schematic depiction of 0 and π states randomly distribute across a Josephson junction.

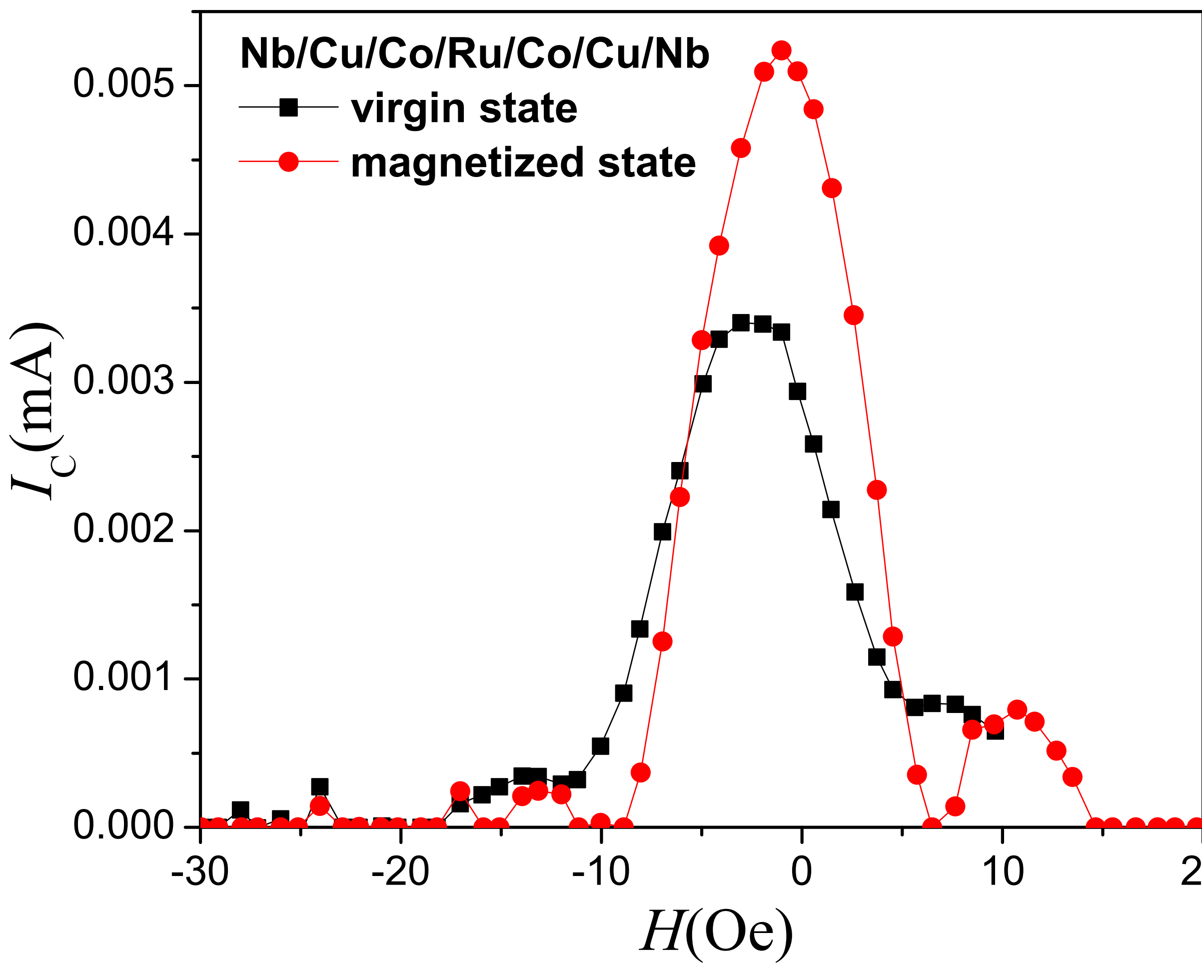

Figure 5.7: Fraunhofer patterns for a 10-μm-diameter spin-singlet Josephson junction made of our "synthetic antiferromagnet". The red circle dots were taken after the sample was magnetized by an in-plane field of 2000Oe; the black squares were measured in the virgin state. This sample was made by Dr. Khasawneh and the data were taken recently by me. The solid lines are just guides for the eye.

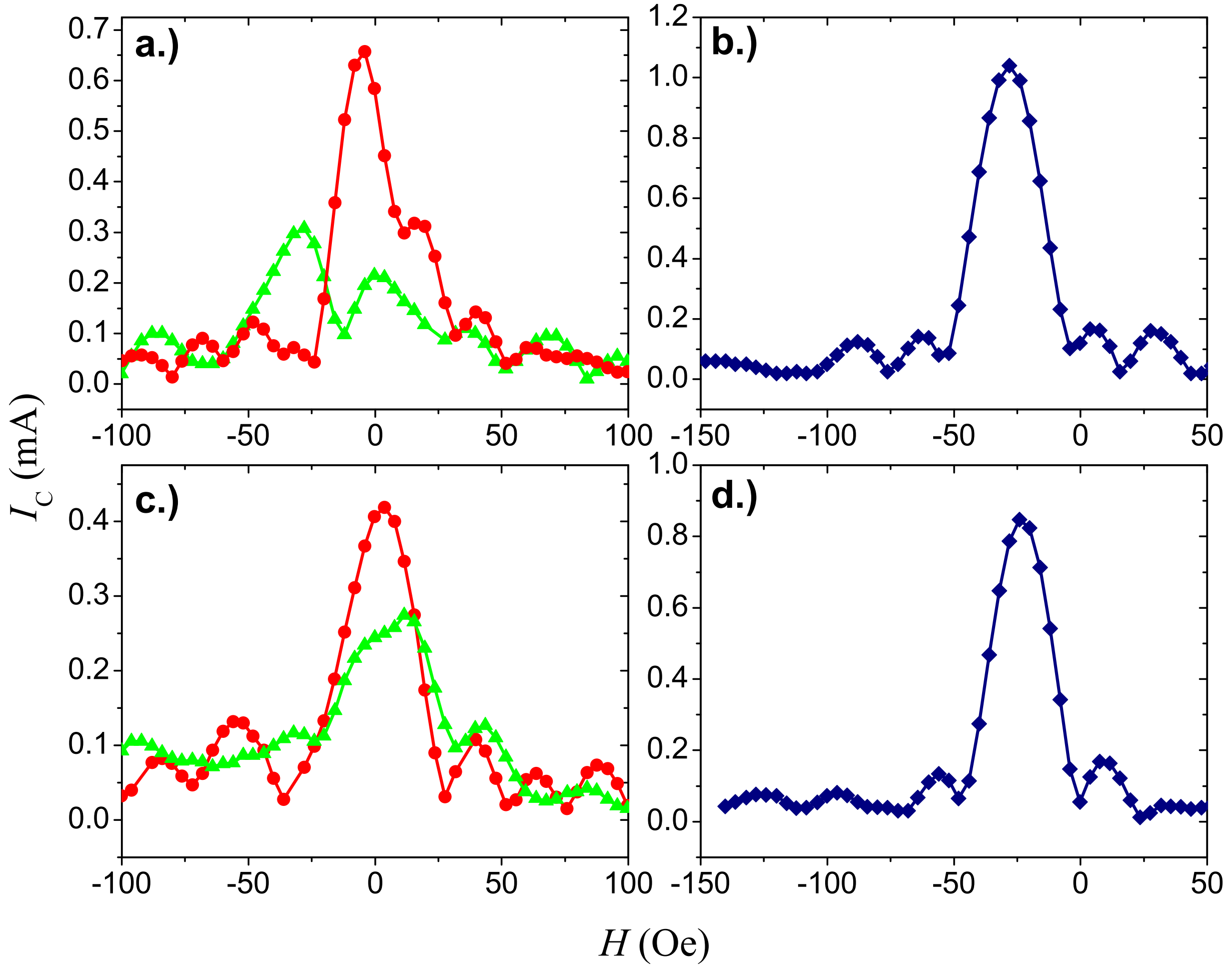

Figure 5.8: Fraunhofer patterns for two 3-μm diameter Josephson junctions with F$'$=F$''$=Ni (1.2nm) and $d_{Co} = 6nm$, measured in the virgin state (a and c), and after the samples were magnetized by a large in-plane field (b and d). Two separate virgin-state runs are shown for each sample. The lines are only guides for the eye. [73]

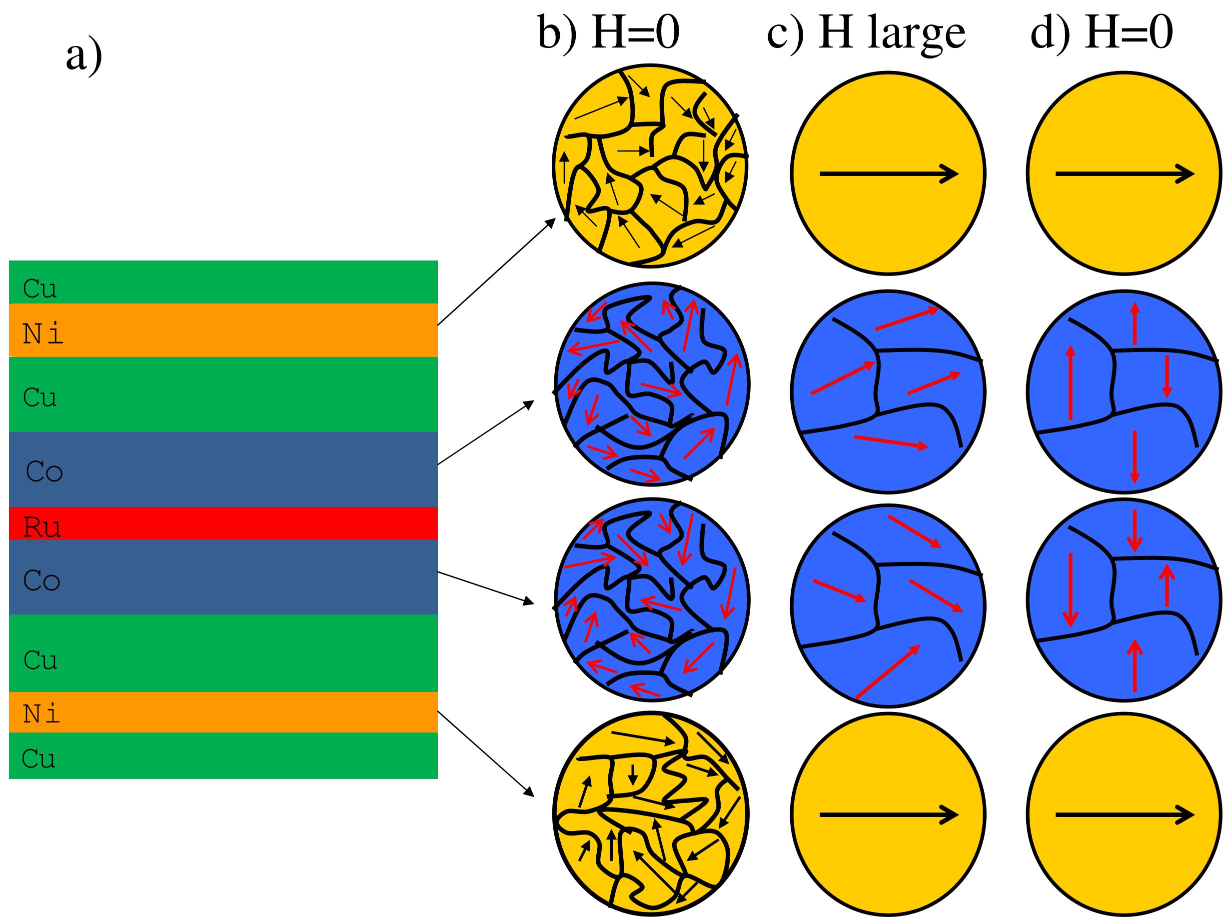

Figure 5.9: A schematic cartoon showing the different stages of magnetization process of the Ni and Co layers before and after we applied a high magnetic field (for example about $1200Oe$). a) Cross section of the magnetic multilayer. b) Magnetization of the domains of the ferromagnetic layers in virgin state. c) Magnetization of the domains while a high field is being applied. d) Magnetization of the domains after the field is removed.

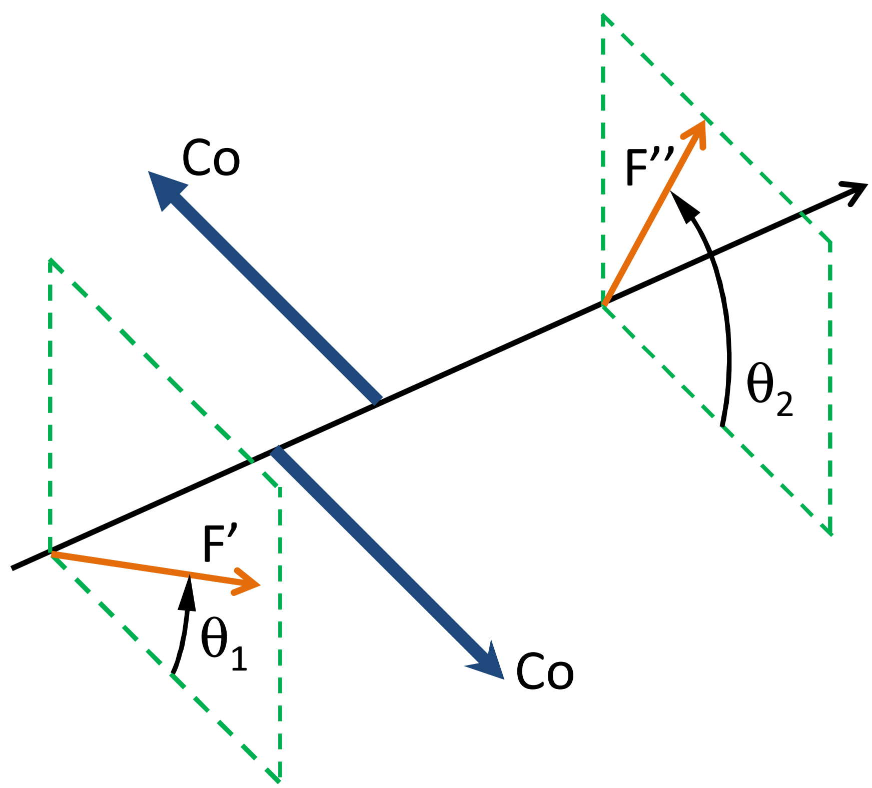

Figure 5.10: Cartoon showing relative orientations of magnetization for the ferromagnetic layers in our Josephson junctions when viewing along the current flowing direction (i.e. along the dirенction perpendicular to the Si substrate as shown in Fig. 5.1). If angles θ_1 and θ_2 have the same sign (where we constrain $|\theta_1|, |\theta_2| < \pi$), the junction will have π coupling; if they have opposite signs, the junction will have 0 coupling. [73]

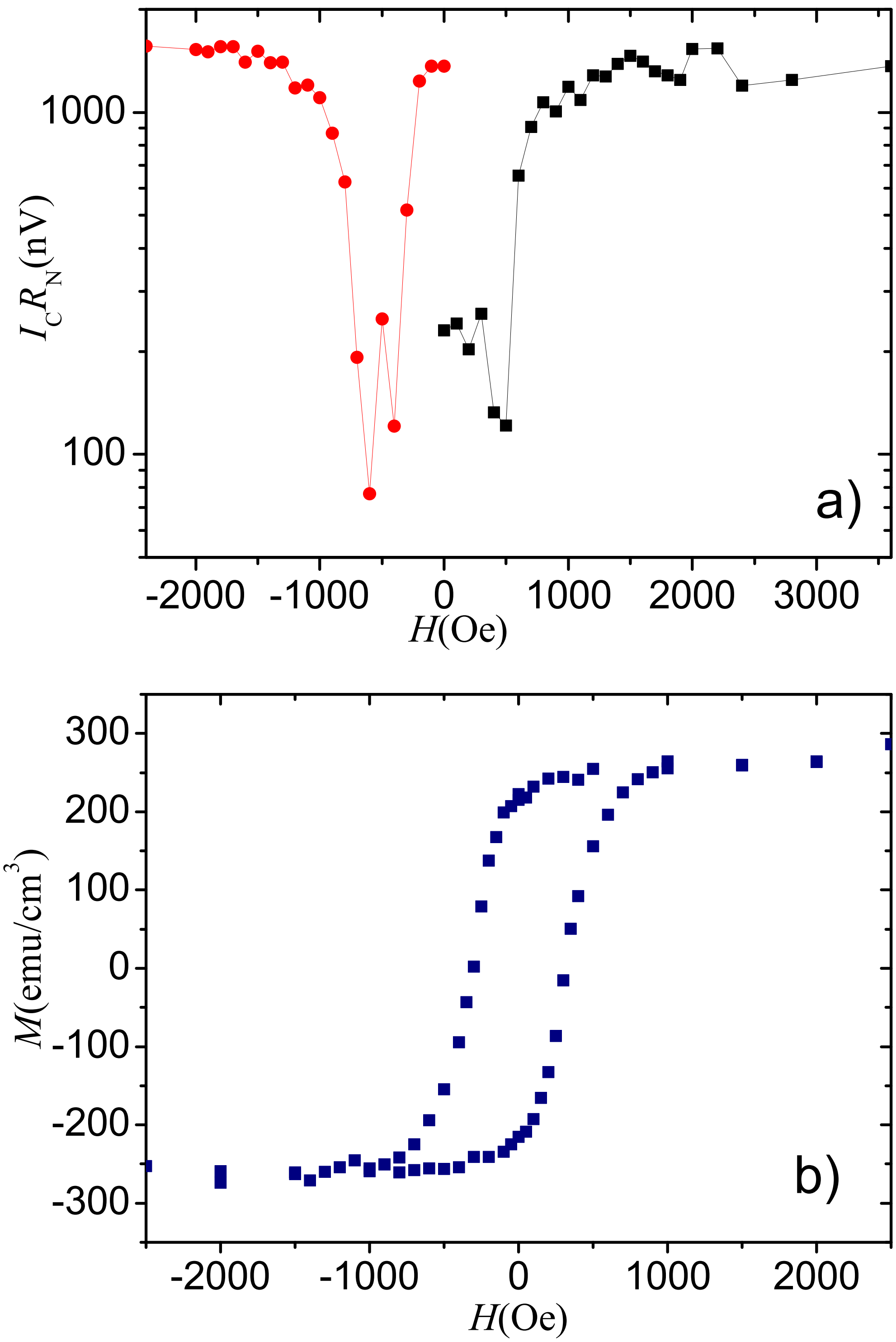

Figure 5.11: a) $I_c R_N$ product vs. applied in-plane field for a 6-μm diameter Josephson junction. The sample was first magnetized in positive field (squares), then the sample was demagnetized and finally re-magnetized in negative field (circles) [73]. b)Magnetization M vs. in-plane field H (black squares); the sample for M vs. H measurement was made by Carolin Klose and also was measured by her.

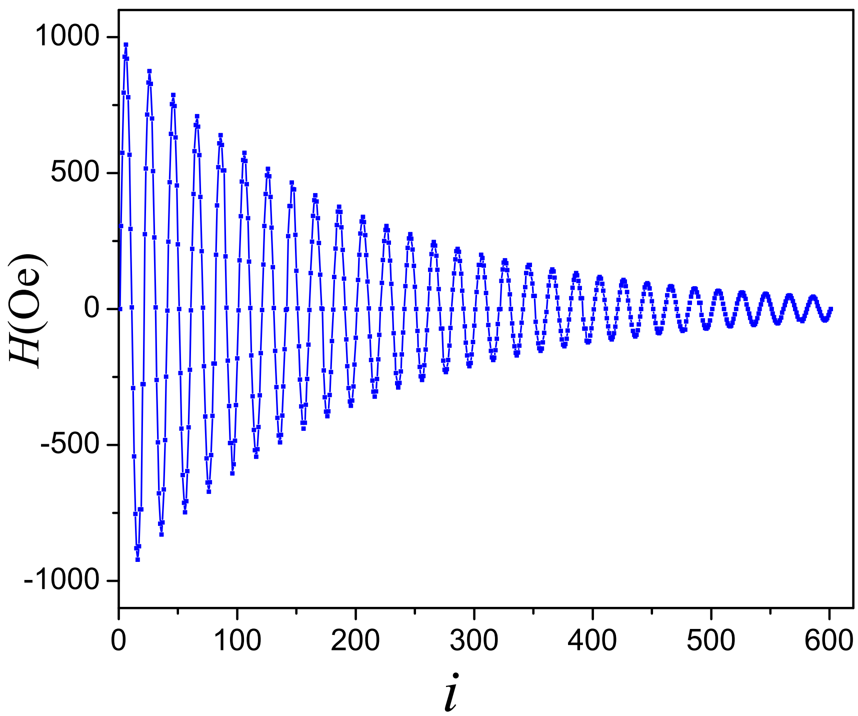

Figure 5.12: One oscillatory decaying demagnetization field example following the $A_{Dem} * \sin((i/P) * \pi) * \exp(-(i/\xi)$ with $A_{Dem} = 1100Oe,\ P = 10$ and $\xi = 190$

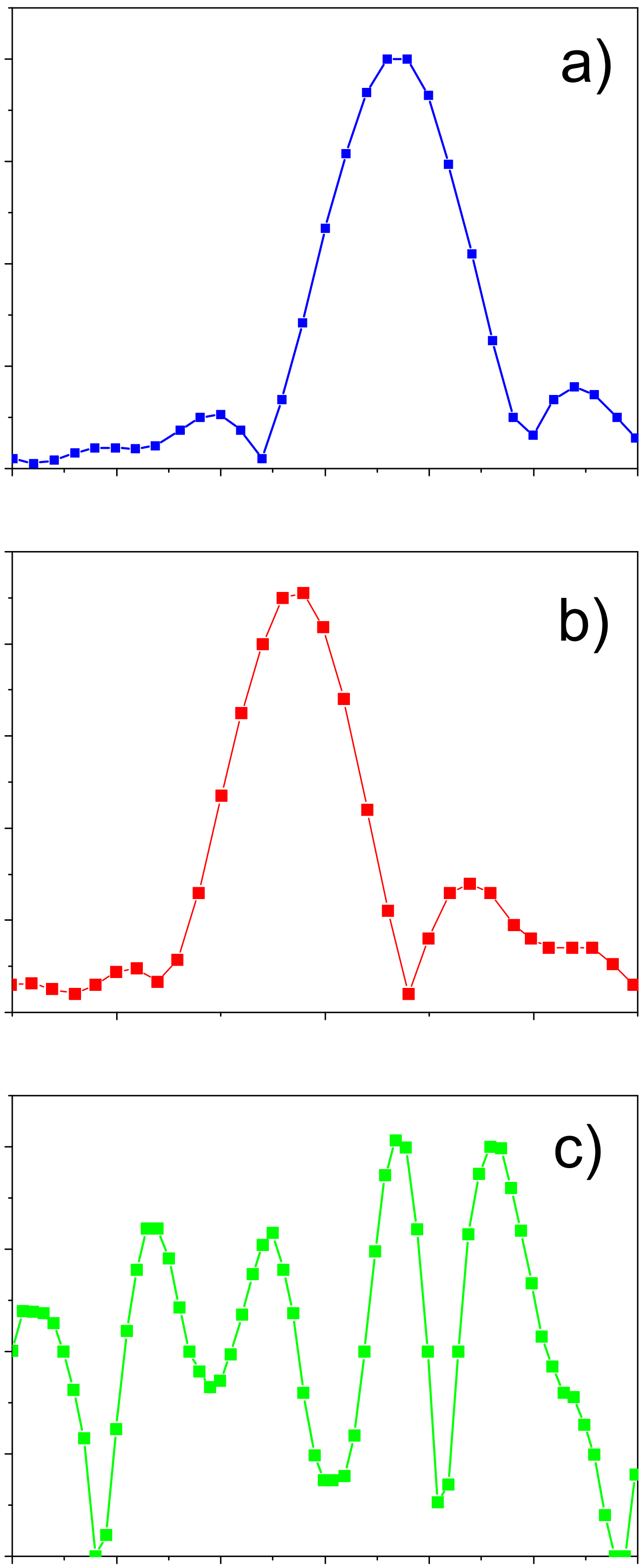

Figure 5.13: Fraunhofer pattern for a 6-μm diameter Josephson junction a) right after sample was magnetized at 2000 Oe . b) after applying $A_{Dem} = 800 Oe$. c) after applying $A_{Dem} = 1200 Oe$

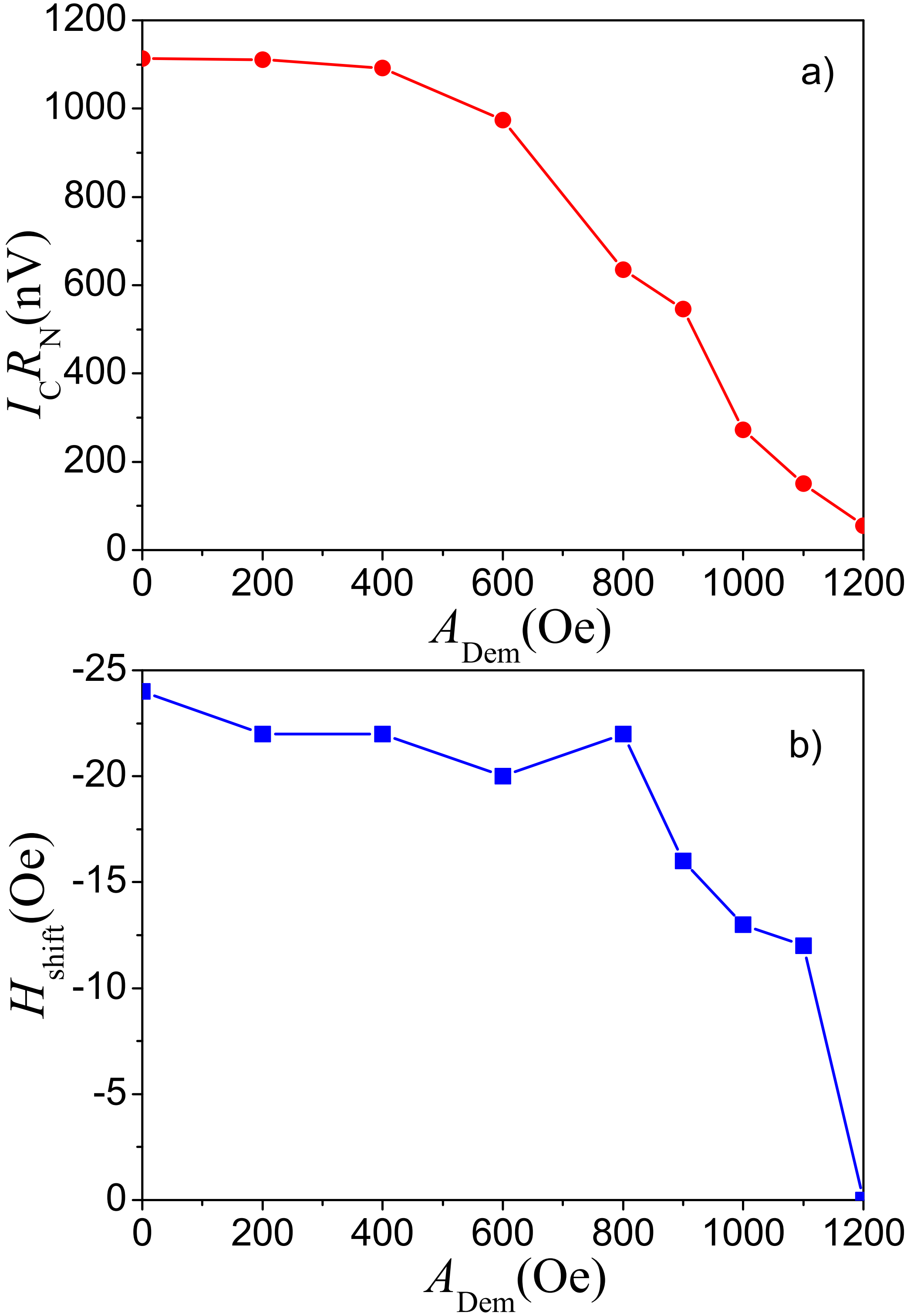

Figure 5.14: First we fully magnetized our sample with 2000 Oe in-plane field. Then we took Fraunhofer patterns after applying step-increasing oscillatory decaying in-plane field. a) $I_C R_N$ vs A_{Dem}, b)field shift of the center peak H_{shift} vs. A_{Dem}.

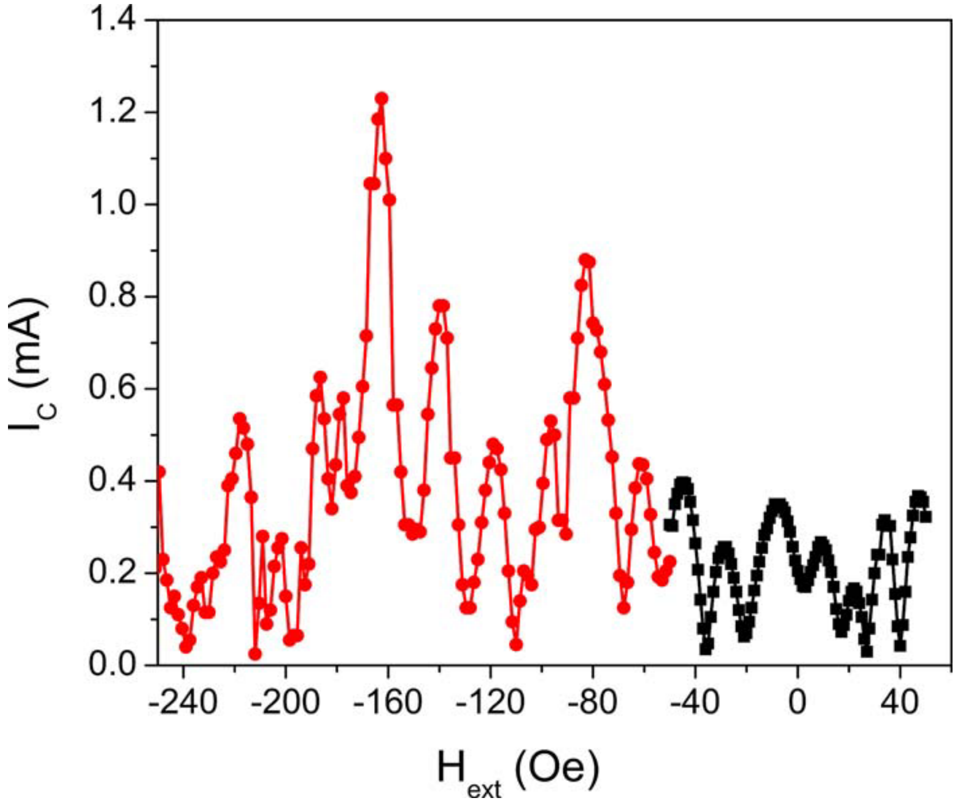

Figure 5.15: (color online). Critical current vs. in-plane magnetic field for a Nb/Ni/Nb circular Josephson junction of diameter $10\mu m$, with $d_{Ni} = 11$nm. The black points (squares) were measured in the virgin state, whereas the red points (circles) were measured after magnetizing the sample in an external field of +1 kOe. The random pattern arises due to the intrinsic magnetic flux of the complex domain structure of the Ni layer. Reprinted figure with permission from [40] as follows: T.S. Khaire, W.P. Pratt Jr. and N.O. Birge, Phys. Rev. B **79**, 094523 (2009). Copyright (2009) by the American Physical Society. http://link.aps.org/doi/10.1103/PhysRevB.79.094523

Chapter 6

Experimental results for area dependence of triplet Josephson junctions

We already notice in the previous chapter that the phase of spin-triplet junctions is controlled by the magnetic moments in them. There are also two indirect pieces of evidence for the existence of 0 and π sub-junctions. We expected that the total critical current of our spin-triplet junctions will be proportional to the square root of the area in the as-grown state. In this chapter, we try to test this idea. The schematic diagram of Josephson junction samples has already been shown in Fig. 5.1.

6.1 Josephson junctions with Nb base

Initially, when I started with this area-dependence project, I did not have too much knowledge about what I would expect. And we also held our breath hoping that we would get nice Fraunhofer patterns even in the as-grown state. Therefore, when we observed Fraunhofer patterns as shown in Fig. 6.1 for our 2001 run, we thought that maybe the Ru layer did not behave very well or that the we should try PdNi instead of Ni as the F$'$ and F$''$ layers.

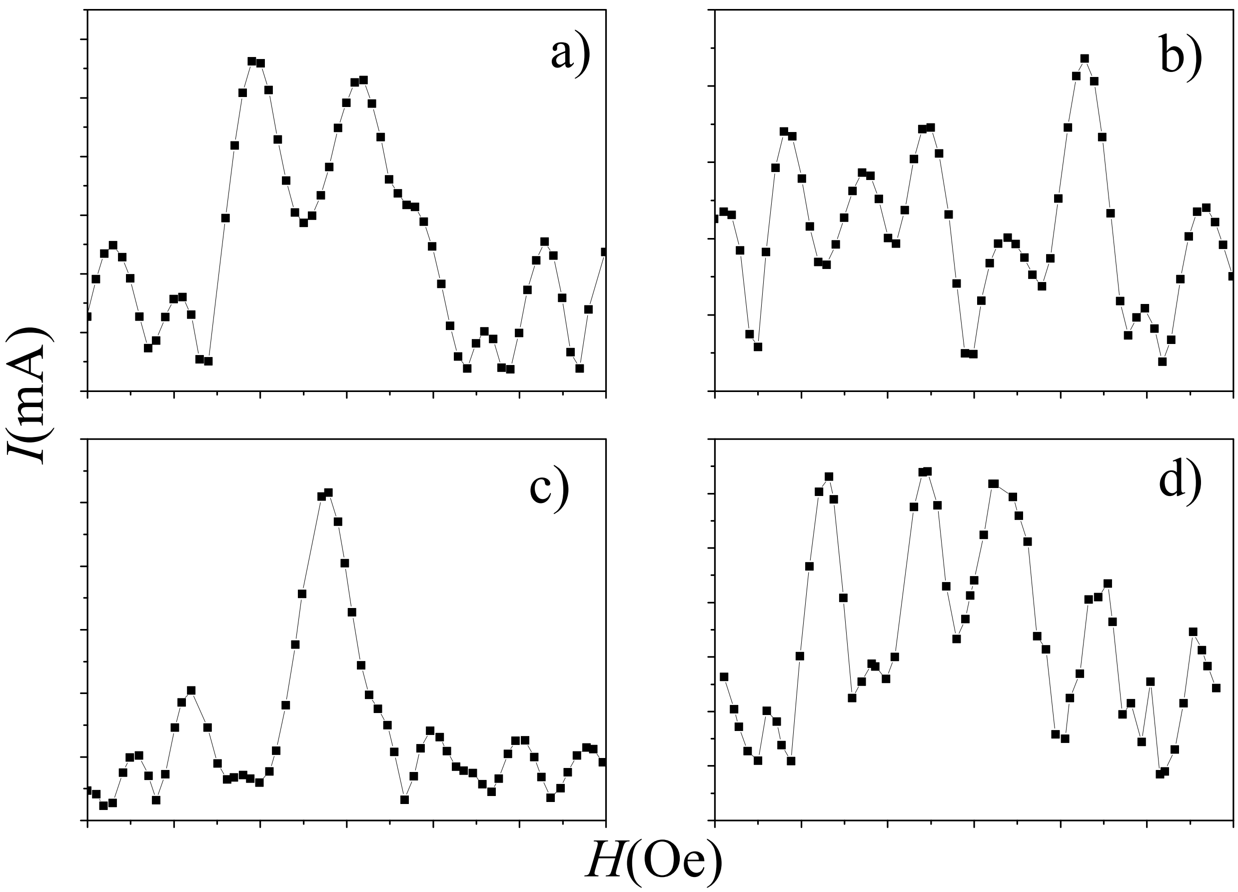

Figure 6.1: Josephson junction critical current vs. in-plane magnetic field for junctions with similar structure as shown in Fig. 5.1 , except here we have $d_{Co} = 10nm$. The data shown in a),b),c) and d) were taken in the as-grown state on a single substrate from run-2001, with junction diameter of $3\mu m$, $6\mu m$,$12\mu m$ and $24\mu m$ respectively.

At the same time, I also made a mistake during our magnetization process. Even though at the beginning I realized that magnetic flux would be trapped in the Nb leads after we magnetized our samples with a high in-plane field, I just did not force myself to remove the flux by lifting our quick dipper above the liquid helium level. And we were also misled by an assumption that pillars near the edge of substrates would not work most of time. These two issues further enhanced my misunderstanding regarding what we obtained.

It really took us a little while to figure out the mystery. We tested our Ru exchange coupling and made sure that 0.6nm thickness could work for us. And we also proposed to replace the Ni with PdNi [74] and found there was no obvious improvement of quality of Fraunhofer patterns in the as-grown state. We also gave up the mechanical mask to arrange six pillars as close as possible to the center of chips by using photolithography, which also did not improve the quality of the Fraunhofer patterns in the virgin state. Later the thickness of Co was also cut to 6nm to see whether it could make some difference. We did not find any correlation of quality of Fraunhofer patterns with the thickness of Co layers.

After we made sure that nothing was wrong with what we did, we proceeded to study the area-dependence of critical current of Josephson junctions again. We fabricated and measured a large number of samples with diameters of $3\mu m$, $6\mu m$ and $12\mu m$ with the structure shown in Fig. 5.1. Fig. 6.2 shows the results for samples grown on our traditional thick (150 nm) superconducting Nb base, for both the virgin and magnetized states. The points representing the magnetized state (open symbols) are averages of the measurements taken after application of 1600, 2000, and 2400 Oe in-plane field. (There is little variation of I_cR_N between those three measurements as we can see from Fig. 5.11.(a).) The solid symbols represent the virgin state. We usually averaged over two runs, although a few samples were measured only once, and one sample was measured 5 times in the virgin state.

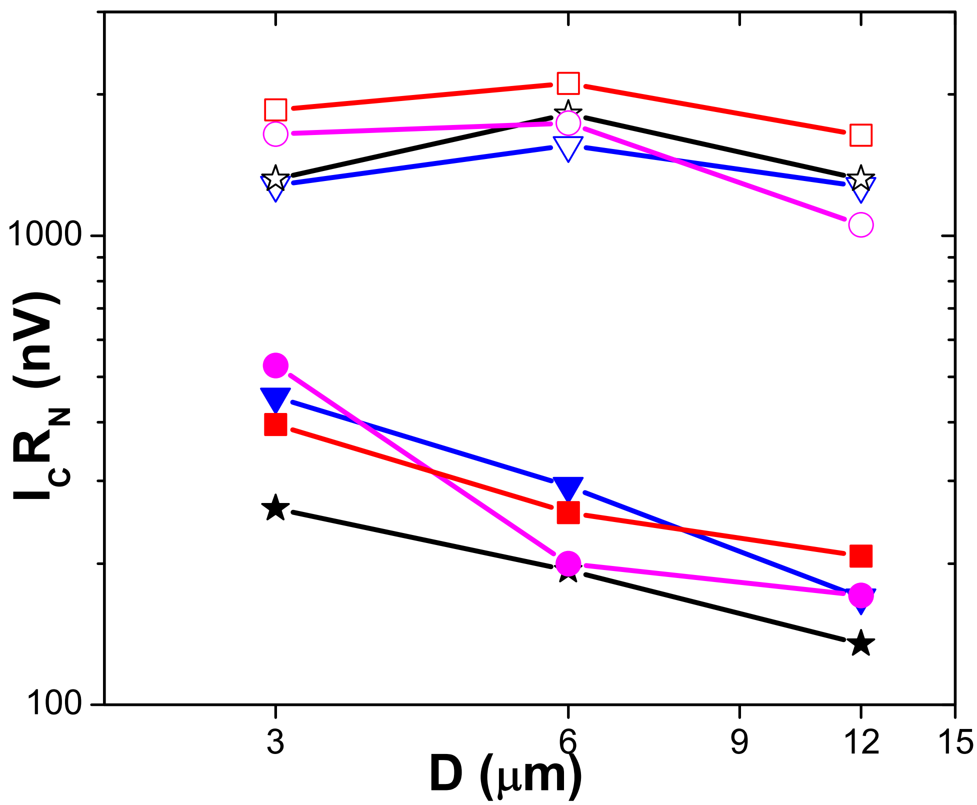

Figure 6.2: (color online) Critical current times normal-state resistance vs. junction diameter for Josephson junctions grown on a 150-nm Nb base electrode from run-2051. Solid symbols represent virgin-state data; open symbols represent data acquired after the samples were magnetized by a large (≈2000 Oe) in-plane magnetic field. [73]

The results of the magnetized state measurements in Fig. 6.2 clearly show that I_cR_N is essentially independent of sample area. And we also observed that the product R_NA of normal state resistance and junction area was roughly a constant equal to $8f\Omega \cdot m^2$, which means R_N is inversely proportional to junction area. These observations imply that I_c is proportional to area. That is the usual situation, and is what one expects when the Josephson coupling is uniform across the junction area. In contrast, the virgin-state data show a decrease in I_cR_N with increasing sample size. According to the random walk model discussed previously, I_c should scale with the square-root of the junction area, hence I_cR_N should scale inversely with the square-root of area, or equivalently, inversely with junction diameter D. The virgin-state data shown in Fig. 6.2 do exhibit a noticeable decrease with junction diameter, supporting the random walk picture, although the dependence is slightly less steep than $I_c \propto D^{-1}$.

If we now look retrospectively at what we did, we realized there was nothing wrong with our first batch of samples (run-2001). And the data of junctions with diameter of $24\mu m$ located close to the edge of substrates is definitely also reliable. Fig. 6.3 shows a global decrease trend in I_cR_N with increasing sample size. Since I did not properly remove trapped flux from the Nb film, the Fraunhofer patterns in the magnetized state did not behave very well especially for the large area samples. Therefore, I do not include the magnetized state for $24\mu m$ pillars in Fig. 6.3. However, we also observed that I_cR_N in the magnetized state is independent with area [74] without including the $24\mu m$ junctions.

6.2 Josephson junctions with Nb/Al multilayer base

While we were still struggling to figure out why we could not get nice virgin-state Fraunhofer patterns, we learned that a $(\mathrm{Nb/Al})_n$ multilayer could provide a much smoother growth interface for the following layers compared with our traditional pure Nb base [67, 61]. Researchers often took advantage of this $(\mathrm{Nb/Al})_n$ multilayer structure when trying to make more reliable tunnel junctions. So we fabricated two types of base layers without the following magnetic multilayer in order to assess the quality of Nb/Al multilayer, of the form $[\mathrm{Nb(40nm)/Al(2.4nm)}]_3\mathrm{/Nb(40nm)/Au(15nm)}$. The results from atomic force microscopy measurement are shown in Fig. 6.4 . The root-mean-squared roughnesses of the pure 150-nm-

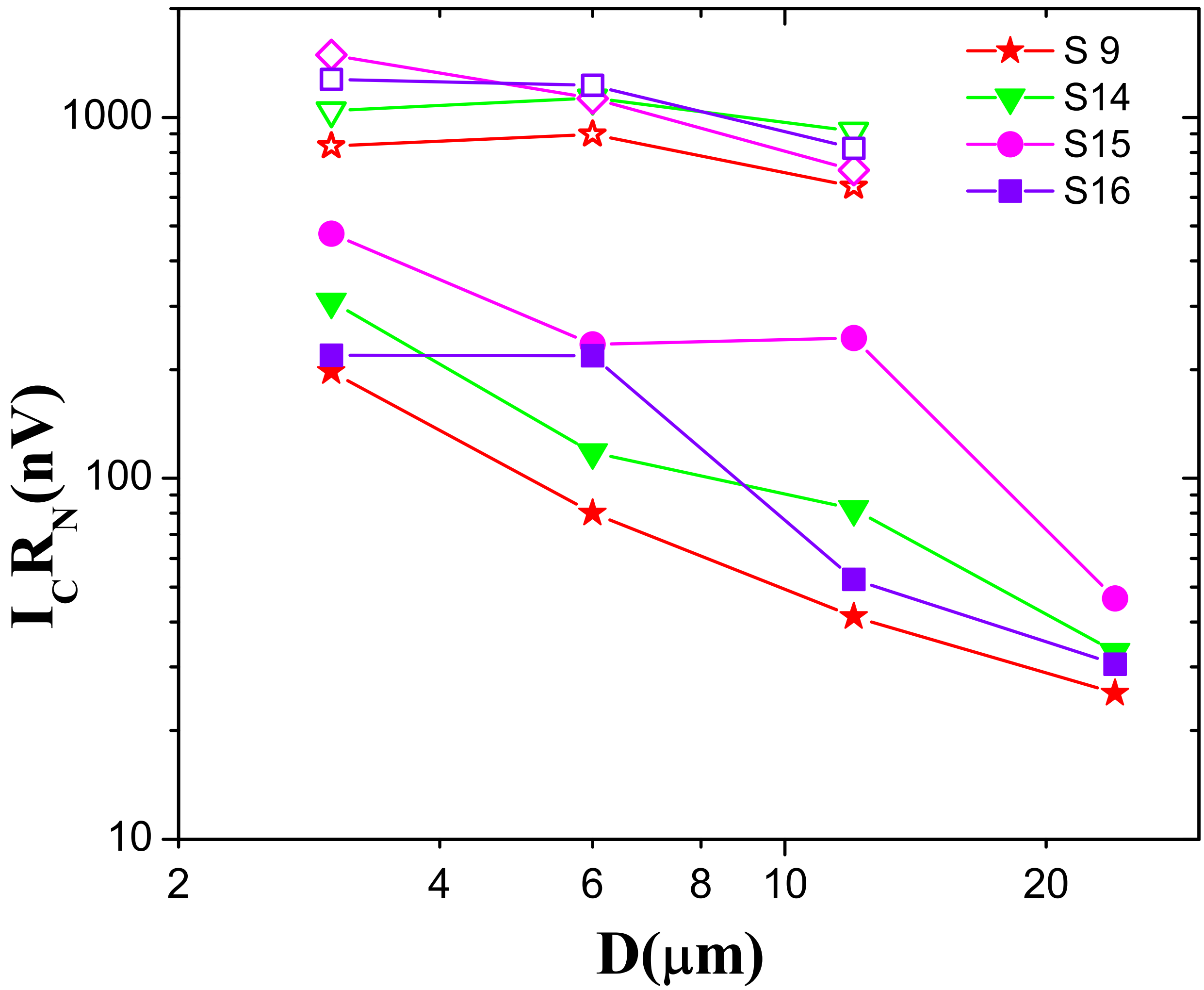

Figure 6.3: (color online) Critical current times normal-state resistance vs. junction diameter in the as-grown state for Josephson junctions grown(solid symbols)and in the magnetized state (open symbols) on a 150-nm Nb base electrode from run-2001.

thick Nb and Nb/Al multilayer are 0.53 nm and 0.23 nm, respectively, over the $250 \times 250\text{nm}^2$ area shown. We can see clearly that the Nb/Al multilayer provides a smoother base than the pure Nb.

In the same run-2051, we also fabricated some samples with the Nb/Al multilayer base of the form [Nb(40nm)/Al(2.4nm)]$_3$/Nb(40nm)/Au(15nm) as shown in Fig. 5.1. We made similar measurement on these samples, as we did with those with the pure Nb base. We found that I_cR_N of these samples is independent of junction diameter both in the as-grown

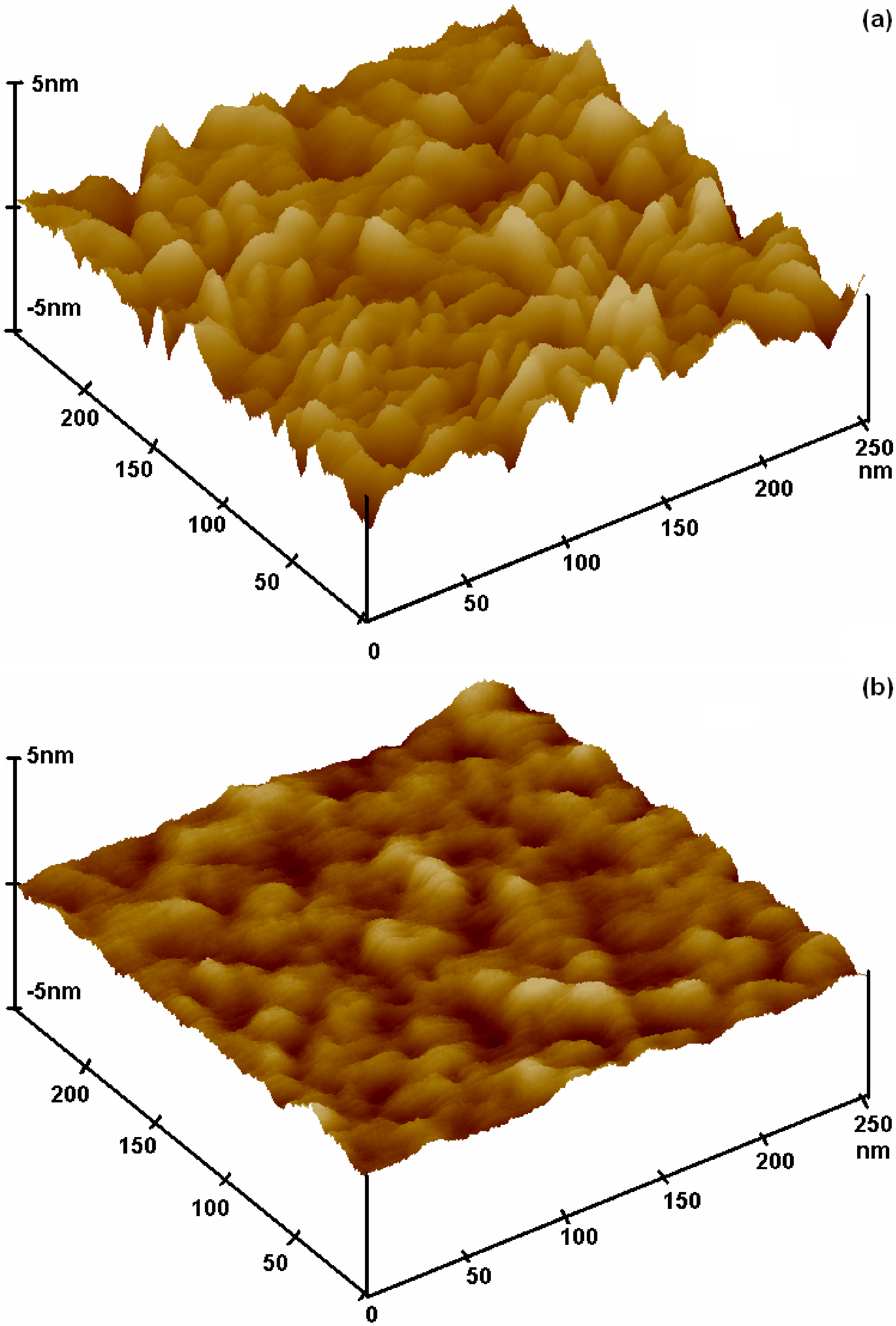

Figure 6.4: (color online) Atomic force microscopy pictures of (a) a 150-nm thick Nb base layer and (b) a Nb/Al multilayer. [73]

state and in the magnetized state, as shown in Fig. 6.5 . However, the value of I_cR_N of these samples in the magnetized state is still very close to those of the pure Nb base samples.

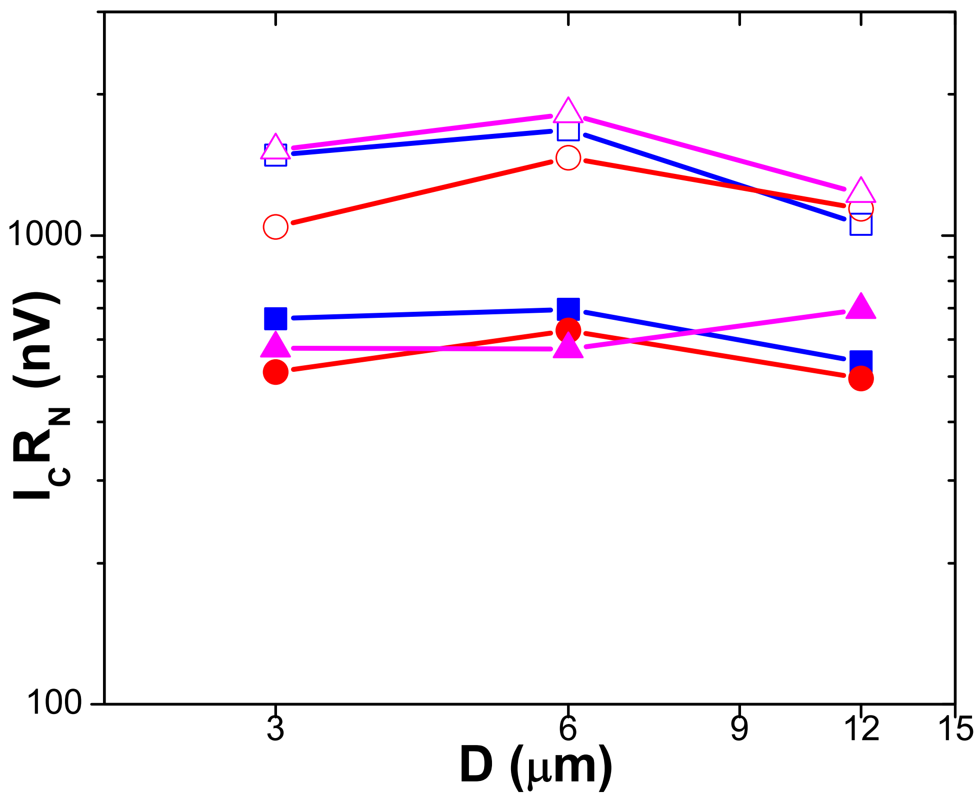

Figure 6.5: (color online) Critical current times normal-state resistance vs. junction diameter for Josephson junctions grown on a Nb/Al multilayer from run-2051. Solid symbols represent virgin-state data; open symbols represent data acquired after the samples were magnetized by a large (2000 Oe) in-plane magnetic field. [73]

6.3 Discussion

After we average a set of samples over the same size for the different base type junctions, we get the results as shown in Fig. 6.6. We immediately notice that (i) I_cR_N for the magnetized state is independent on the size of junctions and does not depend too much on the type of base layer; (ii) the virgin-state data for the Nb base samples shows the decreasing trend with the increasing junction diameter, but not quite following the D^{-1} shown by the dot-dashed line; (iii) the virgin-state data of samples on the Nb/Al multilayer base demonstrate the independence of junction diameter.

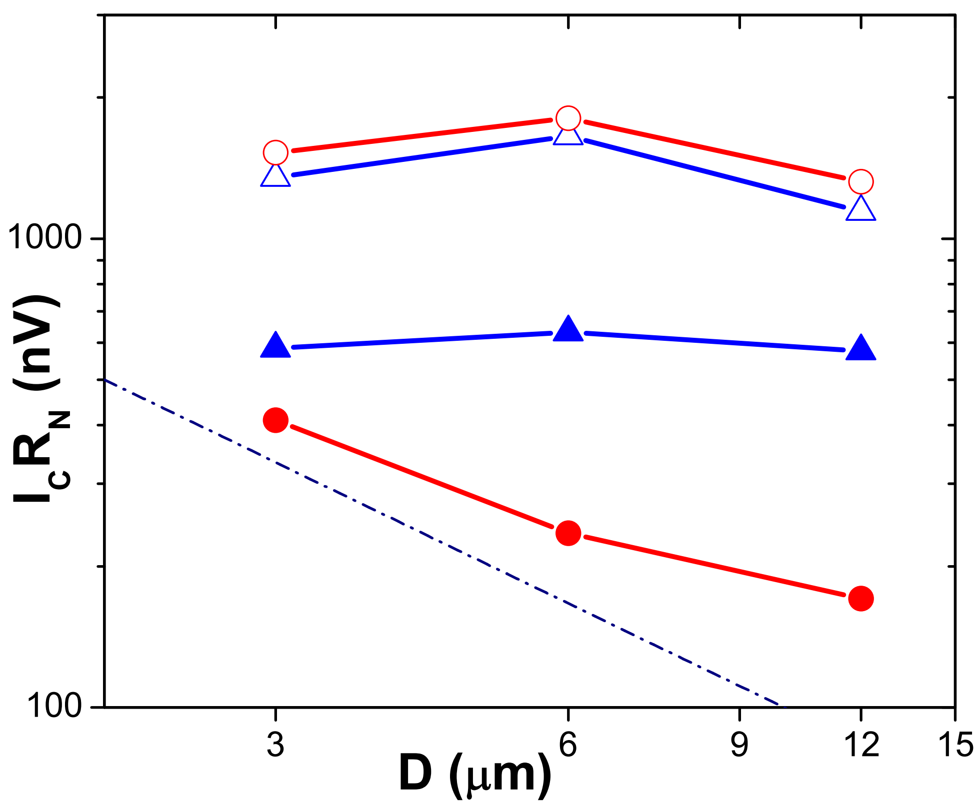

Figure 6.6: (color online) Summary of I_cR_N data for all the Josephson junctions studied in run-2051. Each symbol represents the average value for all samples of a given size and base layer, in either the virgin-state (solid symbols) or after being magnetized (open symbols). The circles represent samples grown on a 150-nm Nb base layer, while the triangles represent samples grown on a Nb/Al multilayer described in the text. The dot-dashed line illustrates the relation $I_cR_N \propto D^{-1}$. [73]

Obviously, the roughness of the base layer does have a very profound effect on the area-dependence of critical current in the virgin state.

One possibility is that the roughness of the Nb base layer perturbs the domain structure of the Ni F$'$ and F$''$ layers –possibly even to the extent that one or both of those layers are not continuous. From some research, researchers have learned that many magnetic materials exhibit magnetically "dead" layers when placed next to nonmagnetic or superconducting materials. [65, 50, 51] Dead layers can arise even at a perfect interface due to electronic structure effects; [45] they are typically exacerbated by interface roughness or by interdiffusion between the two metals near the interface. In cases when surface roughness is dominant, one can imagine the presence of isolated magnetic or superparamagnetic clusters that are only weakly coupled to the bulk of the magnetic film; in the latter case one would expect large spin fluctuations to be highly detrimental to superconductivity.

A second explanation is that the observed sub-linear scaling of the supercurrent with junction area for the junctions grown on the rougher Nb base is simply a reflection of the gradual deterioration of the quality of the Fraunhofer patterns with increasing sample size.

A possible way to address both issues would be to use PdNi alloy rather than pure Ni as the F$'$ and F$''$ layers. PdNi is a weak ferromagnetic material with small magnetization. And we already know that we were able to produce Josephson junctions with high-quality Fraunhofer patterns even with much thicker PdNi layers when Dr. Khaire's studied the spin-singlet Josephson junctions as shown in Fig. **??**. The optimal PdNi thickness for producing spin-triplet supercurrent is in the range of 4-6 nm, [34] which is much thicker than the 1-2 nm optimal range for Ni, [41].

We made some samples with $d_{Co} = 10nm$ and $d_{PdNi} = 4nm$ on the pure Nb base while keeping the rest of the structure of Fig. 5.1. However, we did not gain anything by replacing Ni with PdNi as shown in Fig. 6.7. The Fraunhofer patterns did not turn out nice and neat as we expected.

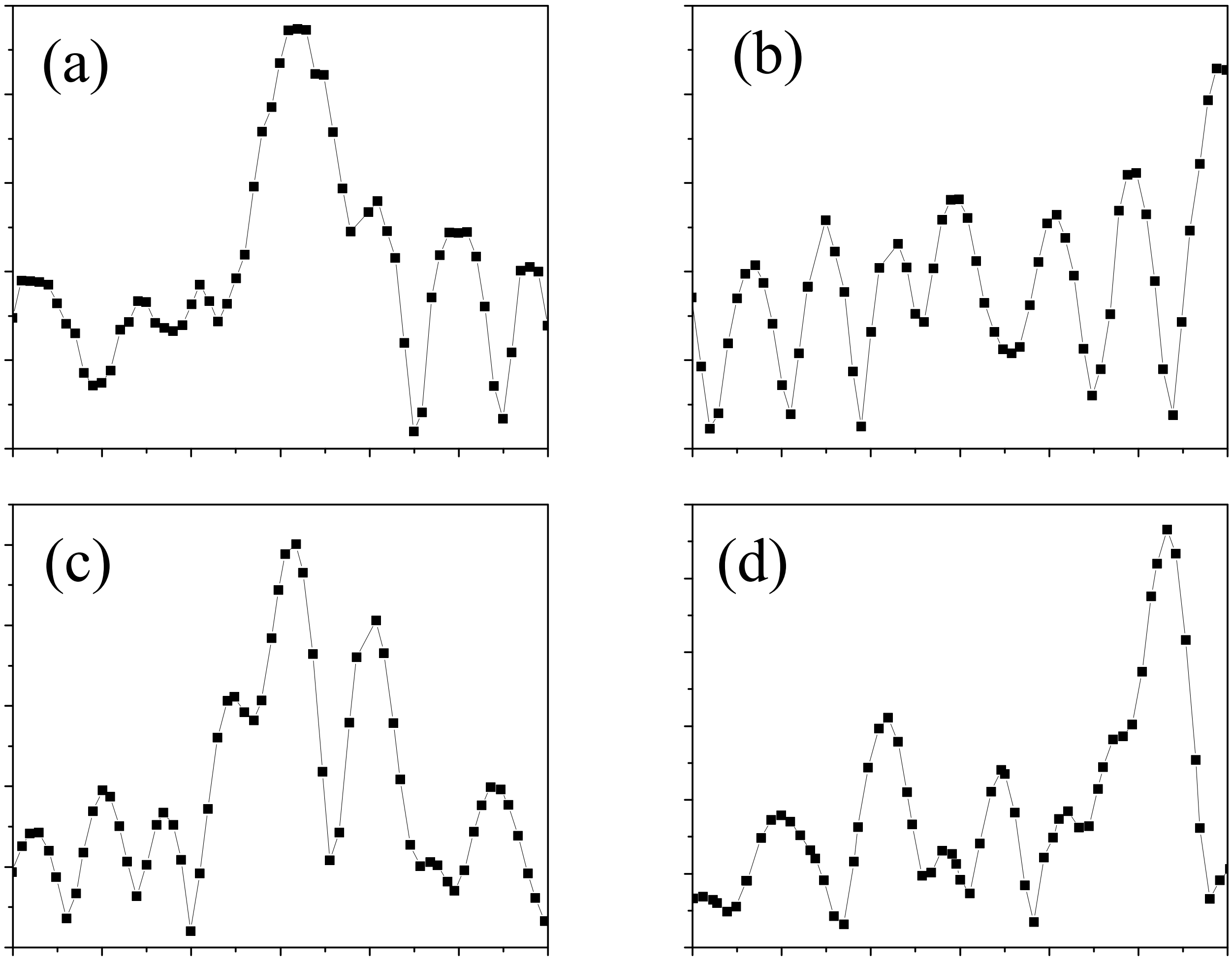

Figure 6.7: Josephson junction critical current vs. in-plane magnetic field for junctions with similar structure as shown in Fig. 5.1 , except here we have $d_{Co} = 10nm$ and $d_{PdNi} = 4nm$. The data shown in a),b),c) and d) were taken in the as-grown state on a single substrate from run-2037, with junction diameter of $3\mu m$, $6\mu m$,$12\mu m$ and $24\mu m$ respectively.

What we can comment on this issue is that the roughness difference of these two type of base layers really affects the domains of Ni layers in a unique way. And the Josephson junctions grown on Nb/Al multilayer base do not follow the random walk model.

Zyuzin and Spivak (ZS) have proposed a brand-new view of a Josephson junction containing a random spatially-varying pattern of 0 and π couplings. [77] Those authors addressed S/F/S junctions with spin-singlet rather than spin-triplet supercurrent, and considered the situation where the F-layer thickness is large, so that the average supercurrent is small, whereas mesoscopic fluctuations of the Josephson coupling have random sign. Fluctuations in F-layer thickness with spin-singlet Josephson junctions could produce spatially-varying 0 and π couplings. In our samples, the spin-singlet supercurrent is negligibly small (see Figure 3 in Ref. [34]), and the random-sign spin-triplet Josephson coupling arises from the local variations in magnetic domain structure. In spite of the different mechanisms underlying the spatially-varying random-sign Josephson coupling, there is no apparent reason why the ZS model should not apply to our spin-triplet Josephson junctions. ZS calculated the total energy of such a junction, and concluded that the ground state corresponds to, on average, a $\pi/2$ phase difference between the two superconducting electrodes. The phase difference is spatially modulated, with local variations toward lower phase difference in regions of 0-coupling and larger phase difference in regions of π-coupling. According to the ZS result, the total supercurrent scales with the junction area, as is the case for conventional Josephson junctions. And in the next chapter, we will try to investigate the ground state of our Nb/Al multilayer base samples using a Superconducting Quantum Interference Device (SQUID).

Chapter 7

First attempt on spin-triplet SQUID

In the previous chapter, it is pretty surprising to notice that the value of I_cR_N of Nb/Al multilayer based samples in the as-grown state is a constant. We discussed the possibility of $\pi/2$ phase difference in the ground state proposed by Zyuzin and Spivak. That brings up a very interesting question, namely, what is the flux period for a DC SQUID made of two $\pi/2$ Josephson junctions? Or in other words, can we determine whether we really have $\pi/2$ Josephson junctions if we can get different SQUID behavior? In this chapter, we will discuss our first attempt to resolve this question using spin-triplet SQUIDs.

7.1 Introduction to SQUID

7.1.1 $\pi/2$ Josephson junctions

Since the states corresponding to $\pi/2$ and $-\pi/2$ are degenerate and have the minimum Josephson energy, we can write down the following energy expression:

$$E_J = E_{J1}(\cos 2\varphi + 1) \tag{7.1}$$

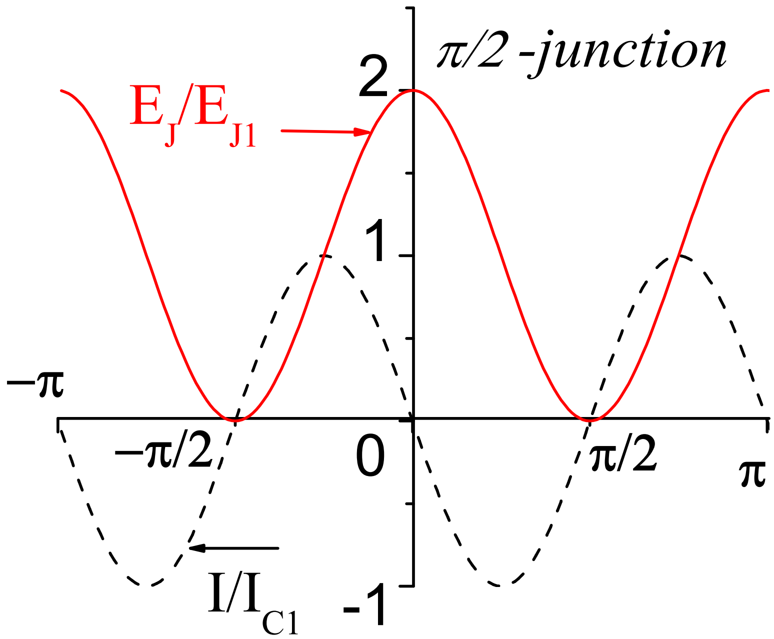

Figure 7.1: Normalized Josephson junction current and coupling energy for $\pi/2$-junction with phase-difference φ as a variable.

We can also find the current-phase relationship from

$$I = \frac{2\pi}{\Phi_0}\frac{\partial E_J}{\partial \varphi} = -\frac{4\pi}{\Phi_0} E_{J1} \sin 2\varphi = -I_{c1} \sin 2\varphi \tag{7.2}$$

where $E_{J1} = (\Phi_0 I_{c1})/(4\pi)$.

In Fig. 7.1, we show the normalized Josephson junction current and coupling energy for a $\pi/2$ junction. By comparing with the 0 and π junctions discussed in Section 3.3, the most obvious difference is that the period of the $\pi/2$ junction is half the period of 0 or π junction.

7.1.2 Traditional SQUID

We have learned that all the electron-pairs in a superconductor can be described by a single wave function where the electron pairs wave retain phase coherence over long distances. And

Fraunhofer patterns in Josephson junctions are one of the phenomena that demonstrate the coherence of Cooper pairs and the diffraction effect of the coherence. Similarly to ordinary electromagnetic waves, interference can be observed with Cooper-pair waves. One type of superconducting quantum interference device is made of two Josephson junctions, as shown in Fig. 7.2. Here we consider the simplest case by assuming that the two junctions have the identical critical current I_c. According to the first Josephson relation Eqn. 3.13, the two junctions are characterized by the current-phase relation $I_1 = I_c \sin(\varphi_{ad})$ and $I_2 = I_c \sin(\varphi_{bc})$. Then we can get the total current

$$I = I_c \sin\varphi_{ad} + I_c \sin\varphi_{bc} = 2I_c \cos(\frac{\varphi_{ad} - \varphi_{bc}}{2}) \sin(\frac{\varphi_{ad} + \varphi_{bc}}{2}) \tag{7.3}$$

By following the nearly identical procedure as in section 3.4, we can obtain the gauge-invariant phase difference φ_{ad} and φ_{bc}. In order to satisfy the requirement that the total phase change along the closed contour is $2\pi n$, we demand

$$\begin{aligned} \oint \nabla\theta \cdot d\mathbf{l} &= 2\pi n \\ &= \Delta\theta_{a\Rightarrow b} + \Delta\theta_{b\Rightarrow c} + \Delta\theta_{c\Rightarrow d} + \Delta\theta_{d\Rightarrow a} \end{aligned} \tag{7.4}$$

The different terms in Eqn. 7.4 are shown below,

$$\Delta\theta_{a\Rightarrow b} = \int_a^b \frac{2\pi}{\Phi_0}(\frac{m^*}{n_s q^{*2}}\mathbf{J_s} + \mathbf{A}) \cdot d\overrightarrow{l} \tag{7.5}$$

$$\Delta\theta_{b\Rightarrow c} = -\varphi_{bc} + \frac{2\pi}{\Phi_0}\int_b^c \mathbf{A} \cdot d\overrightarrow{l} \tag{7.6}$$

$$\Delta\theta_{c\Rightarrow d} = \int_c^d \frac{2\pi}{\Phi_0}(\frac{m^*}{n_s q^{*2}}\mathbf{J_s} + \mathbf{A}) \cdot d\overrightarrow{l} \tag{7.7}$$

$$\Delta\theta_{d\Rightarrow a} = \varphi_{ad} + \frac{2\pi}{\Phi_0}\int_d^a \mathbf{A} \cdot d\overrightarrow{l}. \tag{7.8}$$

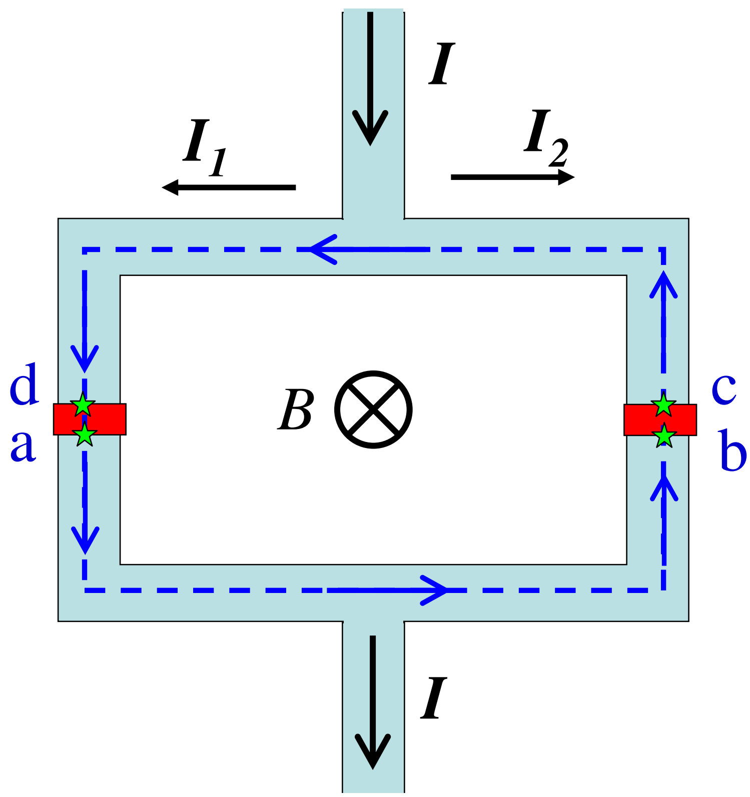

Figure 7.2: A dc-SQUID consisting of two Josephson junctions in parallel connected by a bulk superconducting loop. The broken blue wire indicates the close contour path.

Substitution of Eqn.(7.5-7.8) into Eqn. 7.4 yields

$$\varphi_{ad} - \varphi_{bc} = 2n\pi - \frac{2\pi}{\Phi_0}\oint_C \mathbf{A}\cdot d\overrightarrow{l} - \int_a^b \frac{2\pi}{\Phi_0}\frac{m^*}{n_s q^{*2}}\mathbf{J_s}\cdot d\overrightarrow{l} - \int_c^d \frac{2\pi}{\Phi_0}\frac{m^*}{n_s q^{*2}}\mathbf{J_s}\cdot d\overrightarrow{l} \tag{7.9}$$

Since the superconducting loop is made of superconducting material with thickness and wideness much larger than the London penetration depth, we can take the integration path deep inside the superconducting material where the current density $\mathbf{J_s}$ is negligible. Therefore the last two terms on the right side of Eqn. (7.9) can be omitted. And the integration of $\mathbf{A}$ around the closed contour is equal to the total flux Φ enclosed by the superconducting loop. Then we can get

$$\varphi_{bc} - \varphi_{ad} = \frac{2\pi\Phi}{\Phi_0} - 2\pi n. \tag{7.10}$$

Therefore we can see that the the gauge-invariant phase difference φ_{ad} and φ_{bc} across the two junctions are not independent but are interlocked together via the boundary requirement obtained above.

We can rewrite Eqn. 7.3

$$I = 2I_c\cos(\frac{\pi\Phi}{\Phi_0})\sin(\frac{\pi\Phi}{\Phi_0} + \varphi_{ad}). \tag{7.11}$$

In general, the superconducting loop has a finite inductance L, so we have to take into account the flux generated by the circulating current around loop $I_{cir} = (I_1 - I_2)/2$. Then the total flux threading the loop is given by

$$\begin{aligned}\Phi &= \Phi_{ext} + \Phi_L = \Phi_{ext} + LI_{cir} \\ &= \Phi_{ext} + LI_c\sin(\frac{\varphi_{ad} - \varphi_{bc}}{2})\cos(\frac{\varphi_{ad} + \varphi_{bc}}{2}) \end{aligned}\tag{7.12}$$

Then we can rewrite the total flux as a function of Φ_{ext} and φ_{ad}:

$$\Phi = \Phi_{ext} - LI_c \sin(\frac{\pi\Phi}{\Phi_0}) \cos(\frac{\pi\Phi}{\Phi_0} + \varphi_{ad}) \tag{7.13}$$

Even though here we consider the most ideal case by assuming the critical current in the two arms is identical, we still have to solve the Eqns. (7.11) and (7.13) self-consistently in order to determine the behavior of the SQUID [53].

Before we analyze the limiting cases, we first introduce the screening parameter β_L defined as

$$\beta_L \equiv \frac{2LI_c}{\Phi_0} \tag{7.14}$$

which defines the ratio between the magnetic flux generated by the maximum circulating current I_c and one half the quantum flux $\Phi_0/2$.

7.1.3 Screening effect in SQUID

In this section we are going to take a look at two limiting cases related to the screening effect due to the finite inductance L of the superconducting loop. Then we will discuss the more general case.

7.1.3.1 Negligible Screening effect with $\beta_L \ll 1$

In the case that β_L is far less than one, we can neglect the flux generated by the circulating current and can treat the external flux as the total flux threading the superconducting loop. At a given Φ_{ext}, we can obtain the maximum supercurrent of the SQUID by maximizing

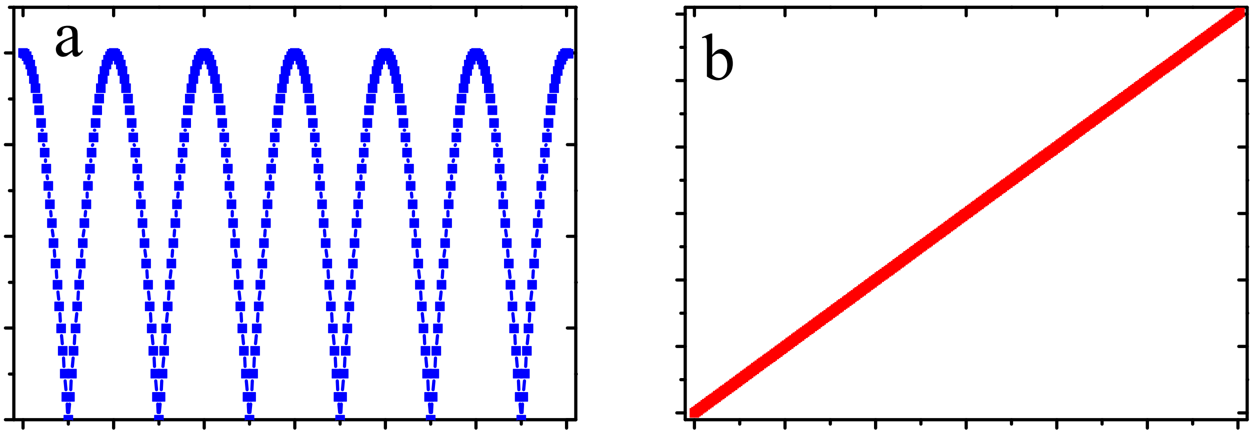

Figure 7.3: For a SQUID with two identical Josephson junctions in the limit $\beta_L \ll 1$, a) the maximum supercurrent I_s^{Max} versus the applied magnetic flux Φ_{ext}; b) the total flux versus the applied magnetic flux Φ_{ext}.

Eqn. 7.11 with respect to φ_{ad}. From condition $dI/d\varphi_{ad} = 0$, we can get

$$\cos(\frac{\pi\Phi}{\Phi_0} - n\pi + \varphi_{ad}) = 0 \tag{7.15}$$

In other words, we will have $\sin((\pi\Phi)/\Phi_0 - n\pi + \varphi_{ad}) = \pm 1$. Then we can find the maximum supercurrent of the SQUID

$$I_s^{Max} \simeq 2I_c \left|\cos(\frac{\pi\Phi}{\Phi_0})\right|. \tag{7.16}$$

Fig. 7.3 shows the periodic oscillation of the supercurrent as a function of the external flux.

7.1.3.2 Large Screening effect with $\beta_L \gg 1$

In the limit $\beta_L \gg 1$, it means $\Phi_0/(2LI_c) \to 0$. Then we can obtain from Eqn. 7.13

$$0 = \sin(\frac{\pi\Phi}{\Phi_0})\cos(\frac{\pi\Phi}{\Phi_0} + \varphi_{ad}) \tag{7.17}$$

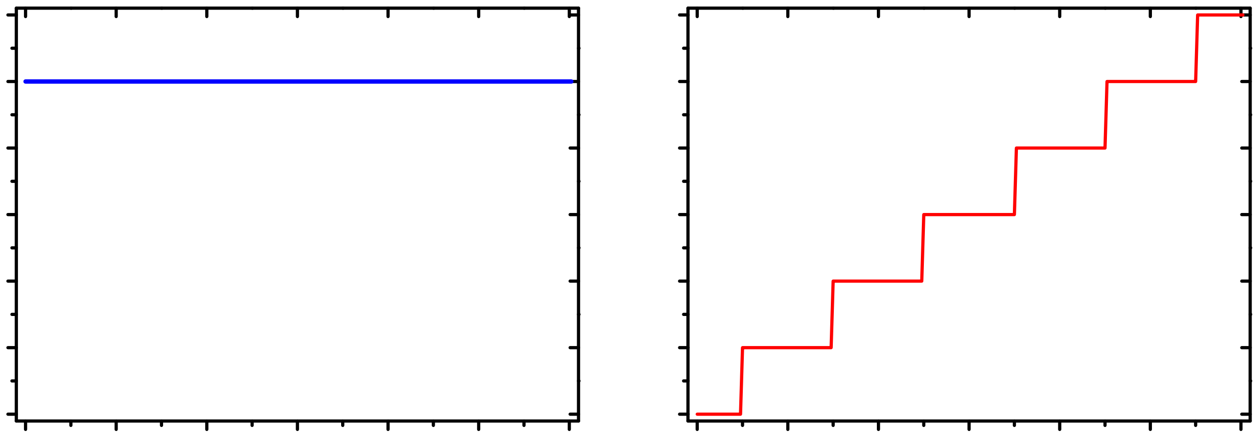

Figure 7.4: For a SQUID with two identical Josephson junctions in the limit $\beta_L \gg 1$, a) the supercurrent I_s versus the applied magnetic flux Φ_{ext}; b) the total flux versus the applied magnetic flux Φ_{ext}.

from which we can get

$$\sin(\frac{\pi\Phi}{\Phi_0}) = 0. \tag{7.18}$$

The above relation shows $\Phi = n\Phi_0$, which means that the total flux in the loop is quantized in Φ_0. The SQUID behaves more and more like but not identical to a single loop formed by a superconducting wire. And the critical current corresponding to this case is equal to $I_s = 2i_c$ and is independent of the magnetic field, as shown in Fig. 7.4

7.1.3.3 Finite screening effect

For any finite β_L, we have to solve Eqns. (7.11) and (7.13) self-consistently, which is far beyond our research scope. At the earlier time of the SQUID discovery, researchers [53, 69] already developed ways to deal with this problem. In Fig. 7.5, we present a schematic I_s versus Φ_{ext} plot. The depth of the modulation of the critical current is reduced due to the appreciable screening of the loop. But the period of the modulation is still one quantum flux Φ_0.

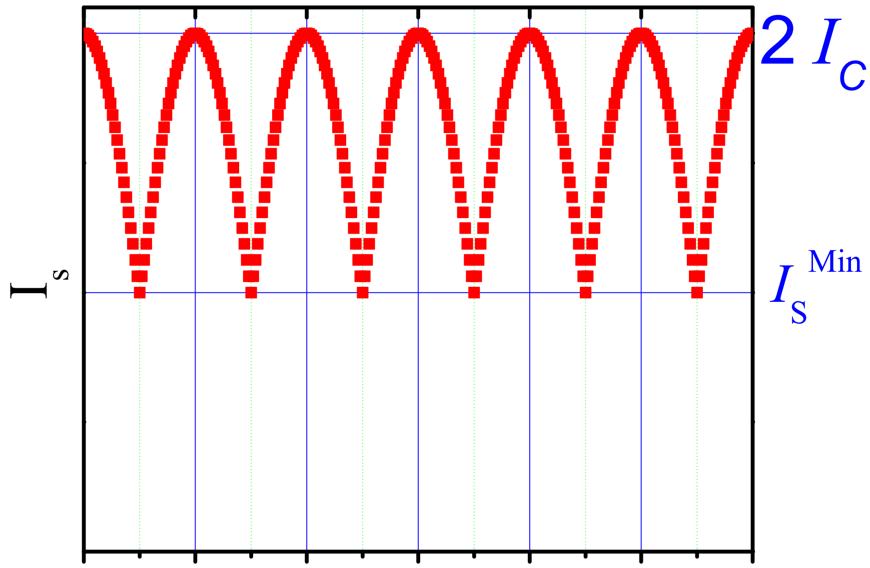

Figure 7.5: A schematic interference pattern for a SQUID with two identical Josephson junctions with finite β_L, the supercurrent I_s versus the applied magnetic flux Φ_{ext}

7.1.4 $\pi/2$ SQUID

If we replace the two traditional $0 - state$ Josephson junctions in the SQUID loop with two $\pi/2$ Josephson junctions, then we need to replace Eqn. 7.11 and Eqn. 7.13 with the following two:

$$I = -2I_{c1}\cos(2\frac{\pi\Phi}{\Phi_0})\sin(2\frac{\pi\Phi}{\Phi_0} + 2\varphi_{ad}). \tag{7.19}$$

$$\Phi = \Phi_{ext} + LI_{c1}\sin(2\frac{\pi\Phi}{\Phi_0})\cos(2\frac{\pi\Phi}{\Phi_0} + 2\varphi_{ad}). \tag{7.20}$$

Obviously the period of the critical current modulation by the external applied magnetic field flux will be half compared with Eqn. 7.11. In the case $\beta_L \ll 1$, we also can obtain the maximum supercurrent

$$I_s^{Max} \simeq 2I_{c1}\left|\cos(2\frac{\pi\Phi}{\Phi_0})\right|. \tag{7.21}$$

Fig. 7.6 shows the interference patten in the case $\beta_L \ll 1$.

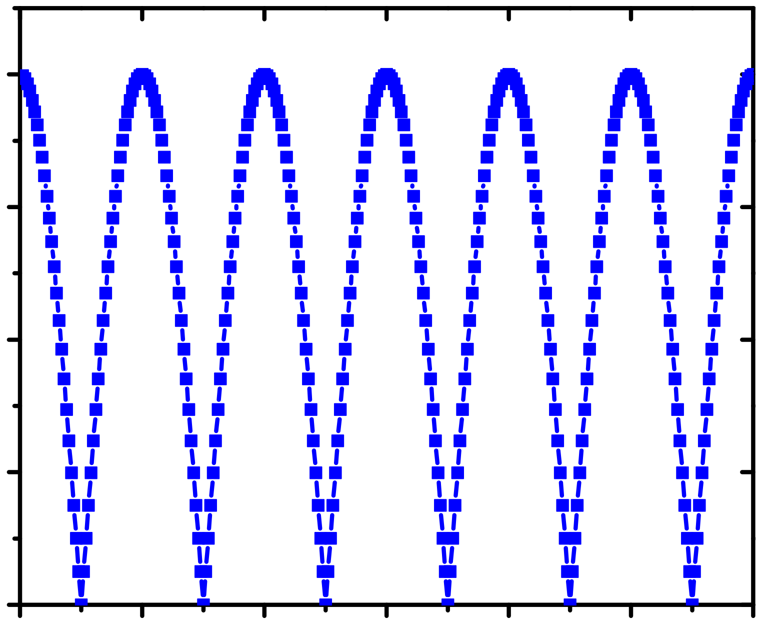

Figure 7.6: A schematic interference pattern for a SQUID with two identical $\pi/2$ Josephson junctions in the case $\beta_L \ll 1$

7.1.5 Four basic SQUID design parameters

There are basically four parameters which should be chosen to obtain a stable SQUID, as listed below. More detailed discussion about these parameters has to be involved with numerical simulations [66, 22, 43, 18].

1. Stewart-McCumber parameter β_c: In order to avoid the hysteretic I-V curve, this parameter has to be restricted to $\beta_c \leq 1$. Since our Josephson junctions do not involve any oxide layer, our S/N/S and S/F/S junctions never show any hysteretic I-V curve. Therefore we do not need to worry about this parameter too much.

2. Screening parameter β_L: In order to get higher modulation of the supercurrent in the SQUID loop, we would think $\beta_L = 0$ would be the perfect choice. And at the same time, it also makes sense that we need larger loop inductance L to increase the SQUID sensitivity. Most of the time, people will choose $\beta_L \simeq 1$. Let us assume we have a

square shaped SQUID loop with dimension $d = 10\mu m$. Then according to one empirical equation [7], we can estimate the inductance of our loop is $L = 1.25\mu_0 d \simeq 1.6\times10^{-11}H$. Finally we can see the constraint on our critical supercurrent $I_c < \Phi_0/(2L) = 64\mu A$

3. Josephson coupling energy E_J: The junction critical current should be much larger than the thermal noise current. Otherwise, the phase fluctuation within the junction will cause the loss of the phase coherence. Computer simulations shows the requirement to be $E_J = \Phi_0 I_0/(2\pi) \gtrsim 5k_BT$. In the case of liquid helium temperature, $I_c > (10\pi k_B T(4.2K))/\Phi_0 = 0.88\mu A$.

4. SQUID loop inductance L: The thermal energy k_BT causes a root mean square thermal noise flux in the loop $< \Phi_{th}^2 >^{1/2} = \sqrt{k_BTL}$. Then we definitely would like to keep this thermal noise flux much smaller than one quantum flux Φ_0. The constraint on the L is $L \lesssim \Phi_0^2/(4k_BT)$. At 4.2K, we can find out $L \leq 18nH$, which is satisfied automatically by a $10 \times 10\mu m$ SQUID loop.

From the above sections, we can see that the modulation period of the $\pi/2$ SQUID is half of the period of the traditional SQUID. As we stated in the beginning of the chapter, we should be able to tell whether our spin-triplet Josephson junctions in our SQUID are $\pi/2$ junctions or not, based on this period difference.

7.2 Calibration of flux coupling to S/N/S SQUID

Since it is the first time for us to design SQUIDs, to make SQUIDs and to measure them, we did not have much idea about the whole process. At the same time, we also need to make sure that the critical current of our Josephson junctions is within the design value range in order to make our SQUID workable. Therefore we spent some time in searching for the proper material to decrease the critical current of our spin-triplet ferromagnetic Josephson junctions, as discussed in Appendix 9.3.2. Then we designed new photomasks and fabricated some traditional SQUIDs made of S/N/S Josephson junctions.

Fig. 4.8 shows a SQUID sample under the optical microscope. The copper-colored fork-like features are the bottom multilayer under the SiO_x. The multilayer has the form Nb(150nm)/CuTi(x)/Nb(20nm)/Au(10nm). The silver-colored fork-like features correspond to the top leads of the form Nb(200nm)/Au(10nm). The top and bottom leads are insulated from each other by 120nm thick SiO_x. The middle straight line was used to generate the out-of-plane magnetic field. Initially we thought about winding up a pancake coil to generate a small out-plane magnetic field to modulate the external magnetic flux in our SQUID loops. Finally we figured out that a straight on-chip wire can do the same thing and provide adequate field in SQUID loops. The detailed sample fabrication process can be found in Chapter .

All the data in this chapter were acquired at 4.2K with the sample in a liquid-helium dewar. The contact lead configuration on real SQUID samples has been shown in Fig. 4.12 b) and c). The commercial SQUID was used in a current comparitor circuit as a null detector to get the traditional current-voltage (I-V) characteristic of the SQUID samples or to measure the flux-voltage curve. All samples still exhibit the standard I-V characteristic similar to an overdamped Josephson junction. In Fig. 7.8 a), we show several I-V plots without any hysteresis. The major difference from our traditional "Frauhofer pattern scan" is that we now replace the in-plane magnetic field with a much smaller out-of-plane field, which is perpendicular to our SQUID loop (i.e. perpendicular to the substrate). And this out-of-plane magnetic field is provided by the straight superconducting wire. After we take all I-V curves for each out-of-plane field, we can obtain a plot of I_c versus $I_{out-plane}$, where $I_{out-plane}$ is the scan current passing through that straight superconducting wire. Fig. 7.7 shows two standard plots of I_c versus $I_{out-plane}$ for two S/N/S SQUIDs on one of our samples. The only difference between the two SQUIDs is the diameters of Josephson junctions. Two Josephson junctions in one SQUID loop are $6\mu m$ in diameter. The two Josephson junctions in the other SQUID loop are $12\mu m$ in diameter. And the loop opening of these two SQUIDs are the same, $10\mu m \times 10\mu m$. Periodic I_c change with $I_{out-plane}$ is clearly observed in our SQUIDs. Then one periodicity of $I_{out-plane}$ corresponds to one quantum flux Φ_0. By the way, the screening effect is also demonstrated in Fig. 7.7. The SQUID with Josephson junctions of $12\mu m$ in diameter obviously shows more apparent screening effect compared with the SQUID with Josephson junctions of $6\mu m$ in diameter, due to the higher critical current, i.e. the ratio $(I_c^{max} - I_c^{min})/(I_c^{max})$ in Figure 7.7 b) is smaller than in Figure 7.7 a).

Since it usually takes a couple of hours to finish one scan of I_c versus $I_{out-plane}$, we usually biased the SQUID with a fixed current and measured the modulated voltage as a function of $I_{out-plane}$, which usually can be done within a few minutes. Fig. 7.8.b) shows the output voltage modulated by the external out-plane flux for fixed bias current, where we have already equated the calibrated periodicity of $I_{out-plane}$ to one quantum flux.

7.3 Characterization of spin-triplet S/F/S SQUID

After we calibrated our SQUID loop patten, we moved forward to make our real spin-triplet S/F/S SQUIDs. Now the bottom multilayer has the form [Nb(40)/Al(2.4)]$_3$/Nb(40)/Au(10) /Nb(20)/Cu(5)/Ni(1.5)/Cu(10) /Co(6)/Ru(0.6)/Co(6)/Cu(10) /Ni(1.5)/Cu(5)/Nb(5)

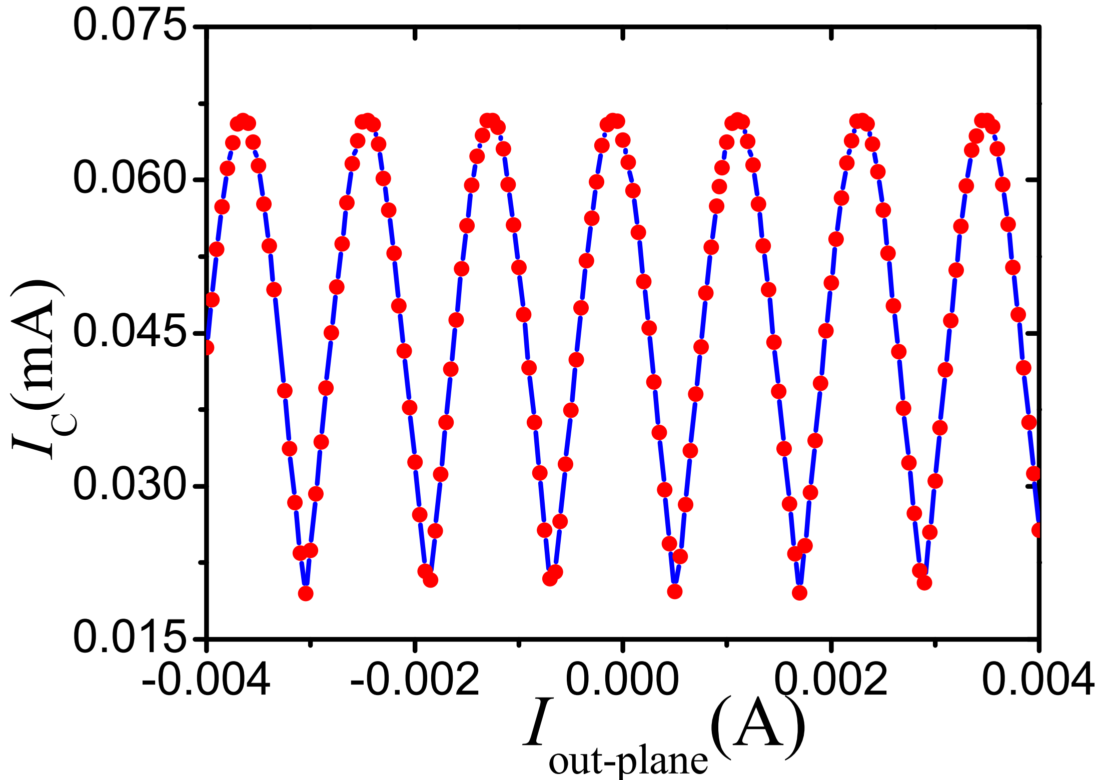

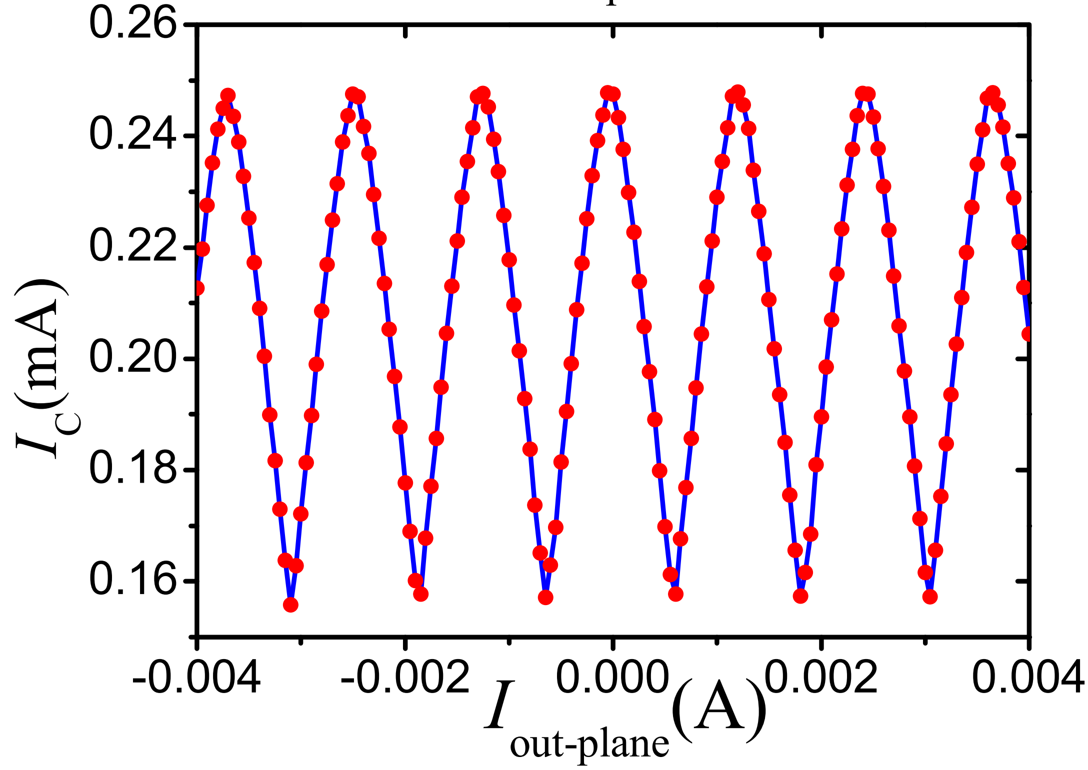

Figure 7.7: The maximum supercurrent I_c versus the out-of-plane magnetic field generation current $I_{out-plane}$ for two S/N/S SQUID. a) Two Josephson junctions in the SQUID loop are $6\mu m$ in diameter. b)Two Josephson junctions in the SQUID loop are $12\mu m$ in diameter.

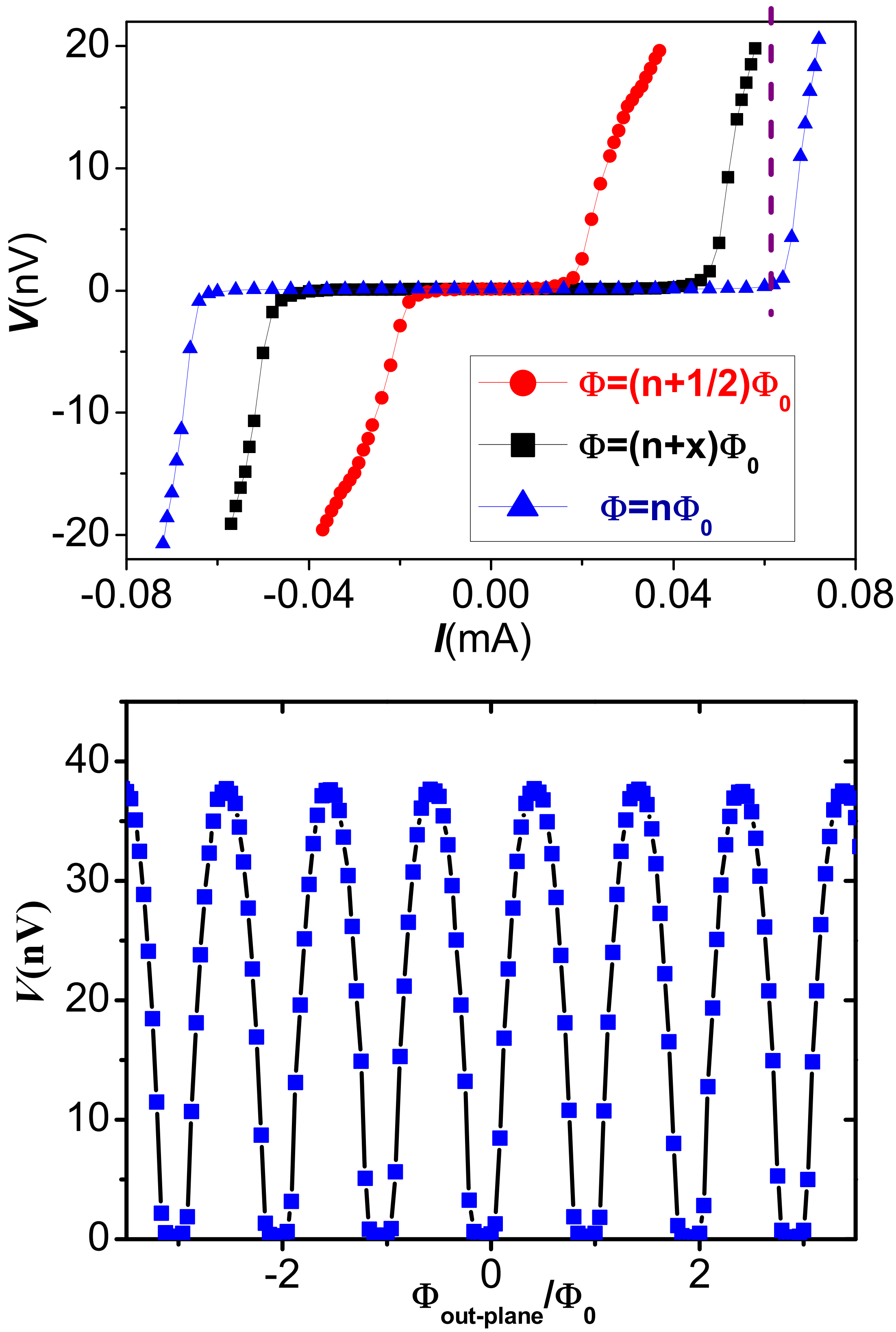

Figure 7.8: a) Current-voltage characteristics of the SQUID, corresponding to the different $\Phi_{out-plane}$. b)Output voltage modulated by the external out-of-plane flux for one bias current $60\mu A$.

/Au(10),where all thicknesses are in nm. The top leads are of the form TiCu(x)/Nb(200nm) /Au(10nm). The top and bottom leads are also insulated from each other by 120nm thick SiO_x. We also fabricated several Nb-based samples with the nearly identical structure in the same run. The only difference is that we replaced $[Nb(40)/Al(2.4)]_3/Nb(40)/Au(10)$ /Nb(20) portion with Nb(150) in the bottom multilayer, while keeping the rest exactly the same. Here the extra TiCu layer was used to reduce the critical current density in our junctions to satisfy the basic SQUID design rules.

We measured both Nb-based and Nb/Al multilayer-based samples, but none of our SQUIDs showed half quantum flux periodicity. Fig. 7.9 shows the output voltage modulated by the external out-plane flux both for one of our Nb/Al multilayer-based samples in the as-grown state and in the magnetized state. In the case of the magnetized state, we first applied a high enough in-plane magnetic field to fully magnetize the sample. Then we removed the high in-plane field and also pulled the quick-dipper above the liquid helium level to remove the trapped flux from the superconducting Nb layer. Usually before we scan the output voltage versus the external out-of-plane flux, we still scanned our traditional "Fraunhofer-pattern" by sweeping an in-plane magnetic field, as shown in Fig. 7.10. Since the peak I_c for the virgin state in Fig. 7.10.(a) locates at $H_{in-plane} = 0$, then we obtained the output voltage versus the external out-of-plane flux by biasing the SQUID with the peak I_c. In the case of the magnetized state, since the location corresponding the peak I_c is around $-30Oe$, we not only biased the SQUID with the peak I_c but also applied the $-30Oe$ in-plane magnetic field.

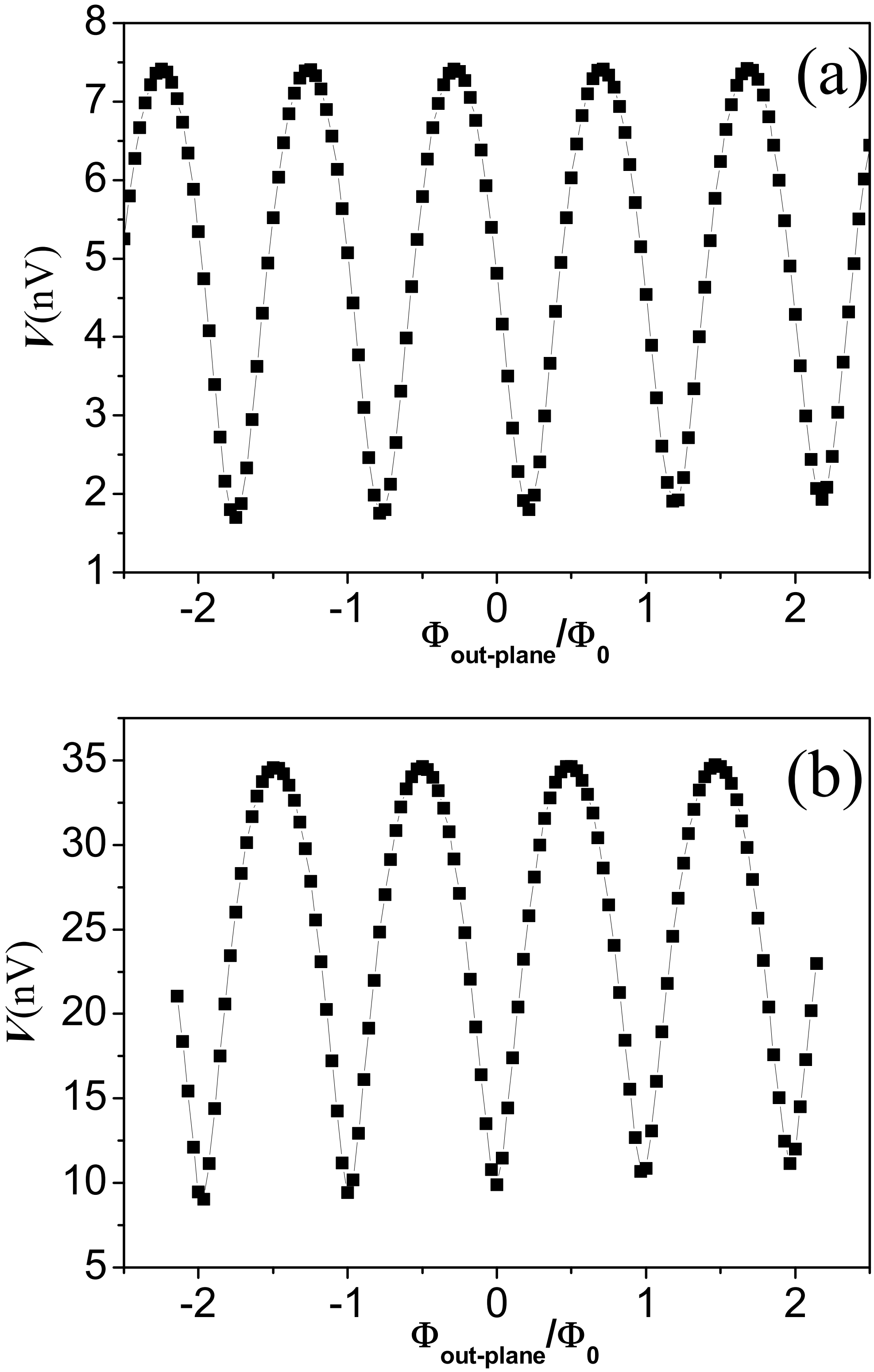

Figure 7.9: Output voltage modulated by the external out-of-plane flux for one bias current, a) in the as-grown state. b) after applying a high enough in-plane magnetic field to fully magnetize the SQUID.

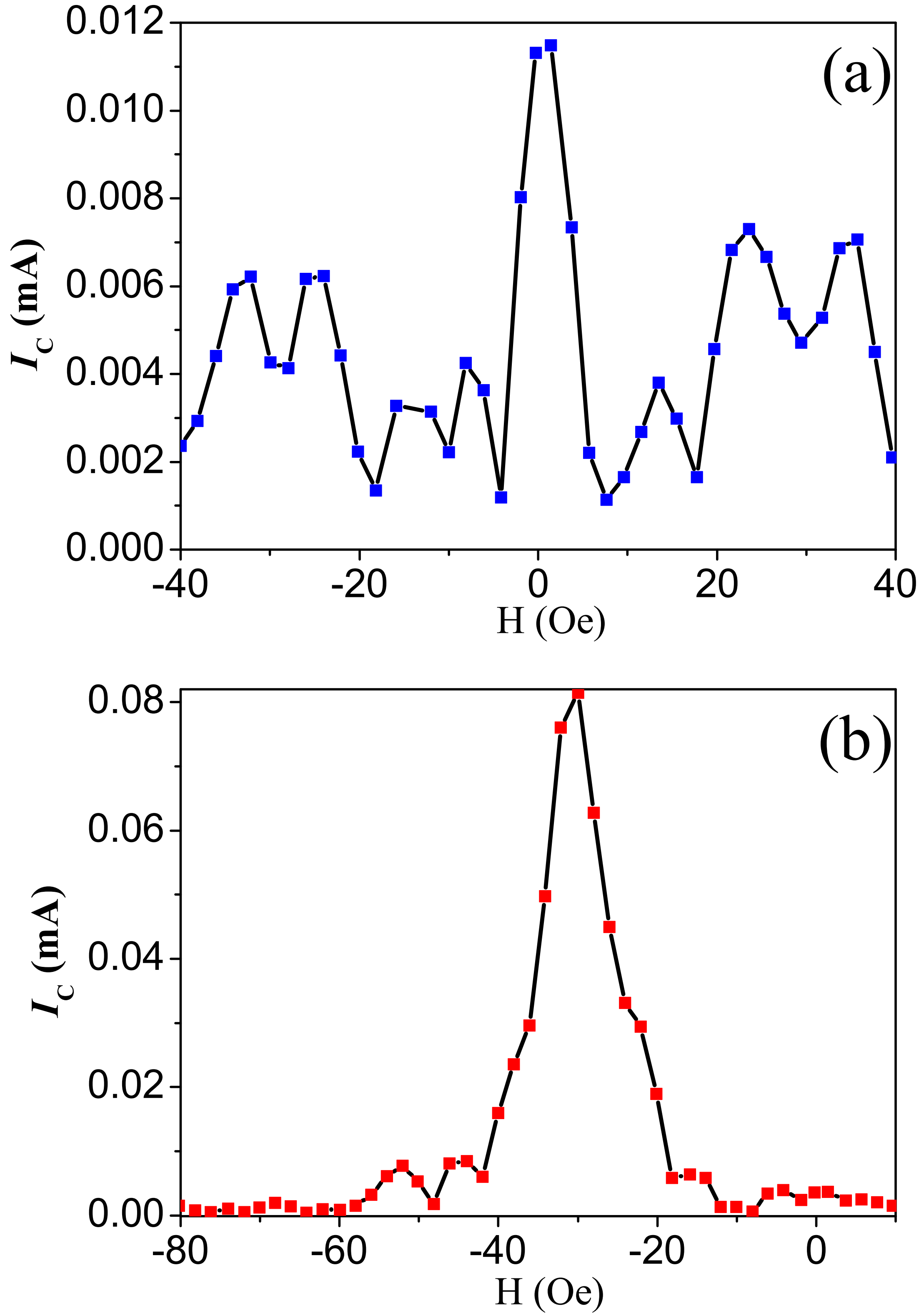

Figure 7.10: The critical current versus the in-plane magnetic field,a) in the as-grown state. b) after applying a high enough in-plane magnetic field to fully magnetize the SQUID.

7.4 Discussion of results

We can clearly see from Fig. 7.10 that we were able to get the enhanced critical current after magnetizing the sample which was one of the signatures of spin-triplet Josephson junctions. However, there was no evidence to demonstrate the half-quantum flux periodicity SQUID.

There are some possible explanations for the failure to observe $\pi/2$ state Josephson junction-SQUID.

First of all, the Zyuzin and Spivak model may not apply to our finite size junctions. Maybe small junctions are dominated by the largest sub-junction, which is 0 or π. Second maybe the experimental method might not be right.

Chapter 8

Conclusions and future perspective

8.1 Overview

The objective of the experiments carried out in this dissertation was to explore the phase information of Long-Ranged Spin-Triplet Correlations (LRSTC) by studying the ferromagnetic Josephson junctions. Our spin-triplet ferromagnetic Josephson junctions have been confirmed to be reproducible and reliable. Yet the phase information is really hard to measure directly, even though it was proposed at the beginning of the LRSTC theory development. Theorists found that the relative orientation of magnetizations of different magnetic layers can lead to different phases of josephson junctions, 0 or π states. Ferromagnetic multilayer Josephson junctions made by our group provide us one unique system to dig deep into this problem.

8.2 Summary of our work

The first indirect evidence observed by our group is the enhancement of the critical current of our Josephson junctions in the magnetized state. According to the theories, it is possible that 0 and π subjunctions in the as-grown state are distributed across a single junction and that the π phase is going to dominate the whole area of the single junction after we magnetize our sample. Therefore, the enhancement is highly possible since there is no more cancelation between 0 and π subjunctions in the magnetized state. Furthermore, according to the random walk model, the critical current of our junctions is proportional to the square root of the area of junctions, which totally contradicts the long-held knowledge on the critical current of traditional Josephson junctions. In order to test this random walk model, we redesigned new photomasks, made improvement on the sample process and wrote a new measurement program with an enhanced data acquisition algorithm. We indeed observed that the critical current of our Nb base samples follows sublinearly with area in the as-grown state. At the same time, the critical current of these samples scales linearly with the area in the magnetized state. This type of non-traditional area dependence of the critical current demonstrates the possible mixture of 0 and π subjunctions in the as-grown state.

While we were working towards improving the quality of our samples, we tried to replace our traditional Nb base with Nb/Al multilayer base. And we observed that the critical current of Nb/Al scales linearly with area both in the as-grown state and in the magnetized state. Zyuzin and Spivak proposed that a $\pi/2$ coupling could dominate across the whole junction due to the spatial fluctuations of the Josephson coupling between 0 and π states.

Since it is really interesting to find out whether a $\pi/2$ coupling is possible or not with these Nb/Al base junctions, we speculated that we could observe half quantum flux periodicity in a SQUID made of two $\pi/2$ Josephson junctions. In order to fullfill the basic requirement of SQUID design, we spent some time to find proper materials to reduce the critical current of our junction. Finally we settled down with TiCu. Then we designed new photomasks and developed new data acquisition programs. Yet the final results from our SQUID samples did not provide any evidence of the $\pi/2$ coupling. However, it cannot definitely be the final word of this problem.

8.3 Future work

Currently my colleague Eric Gingrich is working on smaller size junctions by applying electron beam lithography and trying to realize a single ferromagnetic domain across junctions. At the same time, he is also replacing our traditional SAF structure with new ferromagnetic layers with perpendicular magnetic anisotropy, which will further offer an extra channel over the control of the phase of our spin-triplet Josephson junctions. Then it will further deepen our understanding of the phase.

We are also collaborating with Prof. Dale J Van Harlingen's group at the University of Illinois at Urbana-Champaign. What we are working on is to observe the phase of our Junctions directly by using their setup. We already ordered a new photomask, fabricated the samples and sent them to Illinois. We hope that the results from their measurement will give a more definitive answer to the phase questions.

Chapter 9

Miscellaneous

9.1 Recipes for Photolithography

In order to form a metallized or insulation pattern on a wafer, there are usually two ways to do it. One is etching, if the materials you want to use can be etched. We can evaporate or sputter the desired film onto the wafer first, and etch away the undesired area with the proper protection from the pattern resist. But sometime the materials we try to take off can't be etched, or can only be wet etched, which isn't very precise for small features. Then we have to resort to the lift-off technique. In lift-off, we first pattern the resist, followed by the deposition of the desired materials onto the whole wafer. The resist is then dissolved away in a solvent, carrying the unwanted film with it. However, the normal positive resist profile presents a problem due to it's slope, which is mainly caused by the diffraction effects of the UV light. The deposition over this slope creates a continuous film making it difficult for the solvent to dissolve the resist (refer to figure 9.1). If we try to remove the resist, most likely the edges of the film will tear, or the edges of the film will have abrupt walls. In the worst cases, the whole pattern can be torn away. Therefore, it is pretty crucial for the deposited thin film structure to have a clean edge if we try to make contacts on top it. There are various ways to get proper undercut with proper negative sloped resist profile as discussed in Dr. Khaire's dissertation. For my work, I mainly applied two special techniques

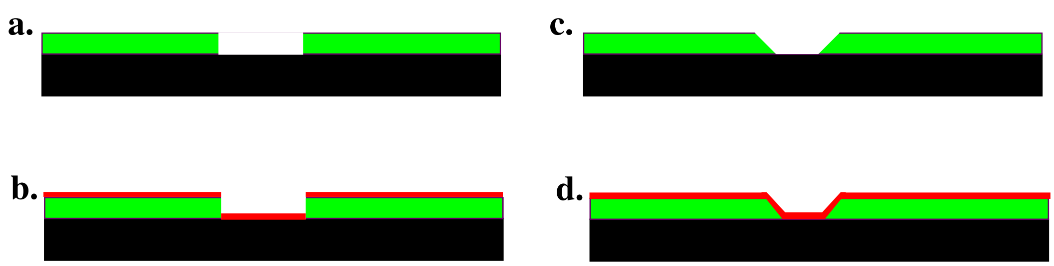

Figure 9.1: a) Ideal profile of developed positive resist. b.) deposition on top of the ideal resist pattern. c.) Schematic profile of developed positive resist with slopes. d.) A continuous film forming on top of the nonideal resist pattern

as shown in the following two sections.

9.1.1 Recipes for S1813

Usually it is impossible for a positive resist S1813 to get an ideal resist profile. Yet the following recipe can provide enough undercut. Please keep in mind that the undercut profile obtained using this method relies heavily on the contact between the substrate and the mask, which is really a serious problem for our case due to the resist buildup around the corners of the diced chips. Therefore we only apply this recipe to the lithography process for the top and bottom leads, since the desired features needed here are relatively large (above 10μm).

1. Clean chips carefully
2. Check for obvious defects and dust particles under the optical microscope
3. Spin coat S1813 resist at 5000 RPM for 40 sec.
4. Bake it at 105^oC on hotplate for 1.5 min or at 95^oC in oven for 30 to 45 minutes.
5. Expose chips under UV light with a mask for 10 sec.
6. Soak in chlorobenzene for 5 min

7. Blow away the chlorobenzene with N2 gas

8. Bake it at 95^oC on hotplate for 1 min to make sure no chlorobenzene residue remains

9. Develop in Microposit 352 for 30-45 sec and rinse it with DI water.

10. Dry chips with N2 gas

11. Remove the resist residue by low power Oxygen plasma for one minute by setting Oxygen pressure to 500mTorr and power to 100Watt

12. Check under the optical microscope to make sure the work is done properly and there is no water residue

Side notes: In order to get clear a view of dust particles, sometimes we need to switch between bright field and dark field modes of the optical microscope. And we take advantage of the differential interference contrast mode (DIC) to inspect the resist residue. DIC works on the principle of interferometry through polarized light, which sometimes can reveal otherwise invisible features. I used Oxygen plasma cleaning to replace our traditional ion milling. This worked very well and never gave me any trouble. The advantage is that it could increase the work efficiency by half a day to one day.

9.1.2 Recipes for AZ5214E

For our junction pillar definition part, we applied AZ5214E resist. AZ5214E is also a positive resist. However, it can be used to produce negative sloped resist profile through the tone reversal process described below. In Fig. 9.2, we show the three main steps involved in getting the well-defined pillars, photoresist definition, ion milling and SiOx deposition. It is

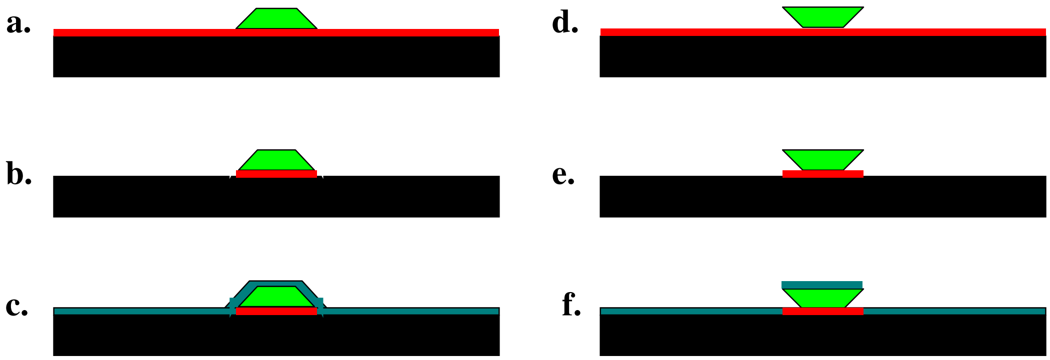

Figure 9.2: Left side corresponds to the case without the proper undercut, while the right side has the perfect undercut. a) and d) Developed photoresist on top of the film. b) and e) After ion milling away the desired film. c) and f) After SiOx deposition.

obvious that we also need well-defined undercut to guarantee the pillar definition success by comparing the left-side and right-side of Fig. 9.2.

1. Spin coat AZ 5214-E at 4000 RPM, 40 sec.

2. Bake on hotplate at 100^oC for 1 minute.

3. UV exposure for 3 sec. [In our case, the pillar area on the mask is transparent.]

4. Bake on hotplate at 120^oC for 1.5 minutes.[This is the reversal baking step, which is very crucial to get a well defined undercut.]

5. Flood expose the chips for 20 sec.

6. Develop in AZ Developer for 40 sec and rinse it with water.

7. Load chips into the ion milling sample holders in the cleanroom

8. Load sample holders into the ion mill chamber outside the cleanroom

9. Wait about 10 hours to reach the base pressure $3 - 4 \times 10^{-8}$Torr

10. Remove the desired film by ion milling

11. Deposit 100nm SiOx

12. Lift off

We still need to pay special attention to the final liftoff. Even though we try hard to have nice and reliable undercut to make out liftoff as easy as possible, it is still pretty hard to get rid of AZ5214E. It needs help from a special solvent, AZ Kwik Strip remover, recommended by AZ company. Usually, we merge our samples in AZ Kwik Strip remover for about 10 minutes on a hotplate at 100^oC. Then we help our liftoff with ultrasonics for 10 minutes. Finally, we rinse our samples with Acetone to clean away the AZ Kwik Strip remover, followed by IPA. The hardship involved here has been proved to be more likely related to the SiO_X deposition part.

With the above recipe, we can obtain very well defined pillars ranging from 3um to 48um in diameter. Similarly, the contact between the mask and chip affects the undercut outcome, especially when we work on diced chips.

9.2 Data collection and processing programs

In order to automate the data collection process, I developed various programs as shown below. All the program flowcharts are simplified to fit into one page, while keeping the essence of them. The most important thing to keep in mind is to pay attention to the persistent switch when changing the current in the superconducting coil, which is used to generate the in-plane magnetic field. It is crucial to minimize the possible current passing through the persistent switch when it is in the normal state. That is to say, whenever we try to change the current in the superconducting coil, it is extremely important to make sure that the current from the magnet power supply is very close to the current value in the superconducting coil set previously, before we open the persistent switch. Last but not least, we need to make sure the SQUID electronics is locked during the whole measurement process, when we use the low temperature SQUID comparator circuits to take data. Therefore, do not leave the measurement totally unattended.

9.3 S/I/S and S/N/S Josephson Junctions

As we pushed our area dependence spin-triplet project further and further, we really tried very hard to study the phase characteristics of the spin-triplet Josephson junction, as we discussed in previous chapters. At one point or another, we realized that we need to investigate the phase through studying SQUIDs. But there are several restrictions to make workable SQUIDs, which we discussed in the SQUIDs section. One of them is the circulating current around the SQUID loop. In order to detect the period of SQUID, we need to make sure the circulating current around our loop would not produce more than one flux quantum in the SQUID. And at the same time, we also need to maintain the size of our junctions to include enough magnetic domains to have enough phase fluctuation across the junctions. To achieve both of these requirements, we needed to reduce the critical current density in our junctions in a controlled way. We tried to tackle this problem through two ways as shown in the following sections.

9.3.1 S/I/S Josephson junctions

Since the discovery of Josephson effects, Josephson tunnel junctions always played an important role not only in basic research but also in applications. Researchers worked hard to improve the quality and reliability of the Nb based Josephson junctions [28, 49]. There are also researchers who made spin-singlet ferromagnetic tunnel Josephson junctions [75, 61] with ultrathin Al_2O_3 tunnel barriers.

Before we stepped into the unknown, we also fabricated basic S/I/S tunnel junctions. We first deposited 150nm Nb followed by 5nm Al. And we passively oxidized the Al in the sputtering chamber with different pure Oxygen pressure for 30 minutes. Then we pumped down the chamber to base pressure before we put another 20nm Nb and 10nm Au protection layers on top of the Al_2O_3 tunnel barrier. Then we finished our usual pillar definition process and the top Nb deposition. As we show in Fig. 9.3 and Fig. 9.4 , we got very good Josephson tunnel junctions. We compare our several characteristic parameters with [49] as shown in table 9.1.

Data source	O_2 Exposure time (Torr*S)	J_C (kA/cm^2)	$I_C R_N$ (mV)	AR $(\Omega * \mu m^2)$
Ours-1	18	2.8	0.7	24
Ours-2	180	1.8	1.50	83
Ours-3	1800	0.42	0.82	194
[49]	180	8.9	1.75	20

Table 9.1: Electrical parameters of our S/I/S junction and [49]

At first, we expected the ultrathin Al_2O_3 tunnel barrier could also work for our spin-triplet Josephson junctions. The $R_N I_C$ is around 1~2 μV for our traditional Ruthenium synthetic anti-ferromagnetic type spin-triplet junctions. The original plan was that the area-resistance product of our S/F/I/S with one layer of Al_2O_3 tunnel barrier inserted into our S/F/S structure could be increased several orders of magnitude, while we hoped that the critical current of S/F/I/S could be lowered a little bit. That is to say, we expected the $R_N I_C$ would be increased.

But we never obtained any tunnel Josephson junctions with observable superconducting portion on our I-V curves. Our expectation that $I_C R_N$ would increase in a S/F/I/S junction may have been a case of wishful thinking. Now let us assume that $R_N I_C$ is not changed. We found from our measurements that the area-resistance product of our S/F/I/S junctions increased by 5 orders of magnitude. This implies that the critical current of the S/F/I/S junctions would be decreased by the same 5 orders of magnitude, which means the critical current would go from the mA range to the nA range. Then we need to consider the

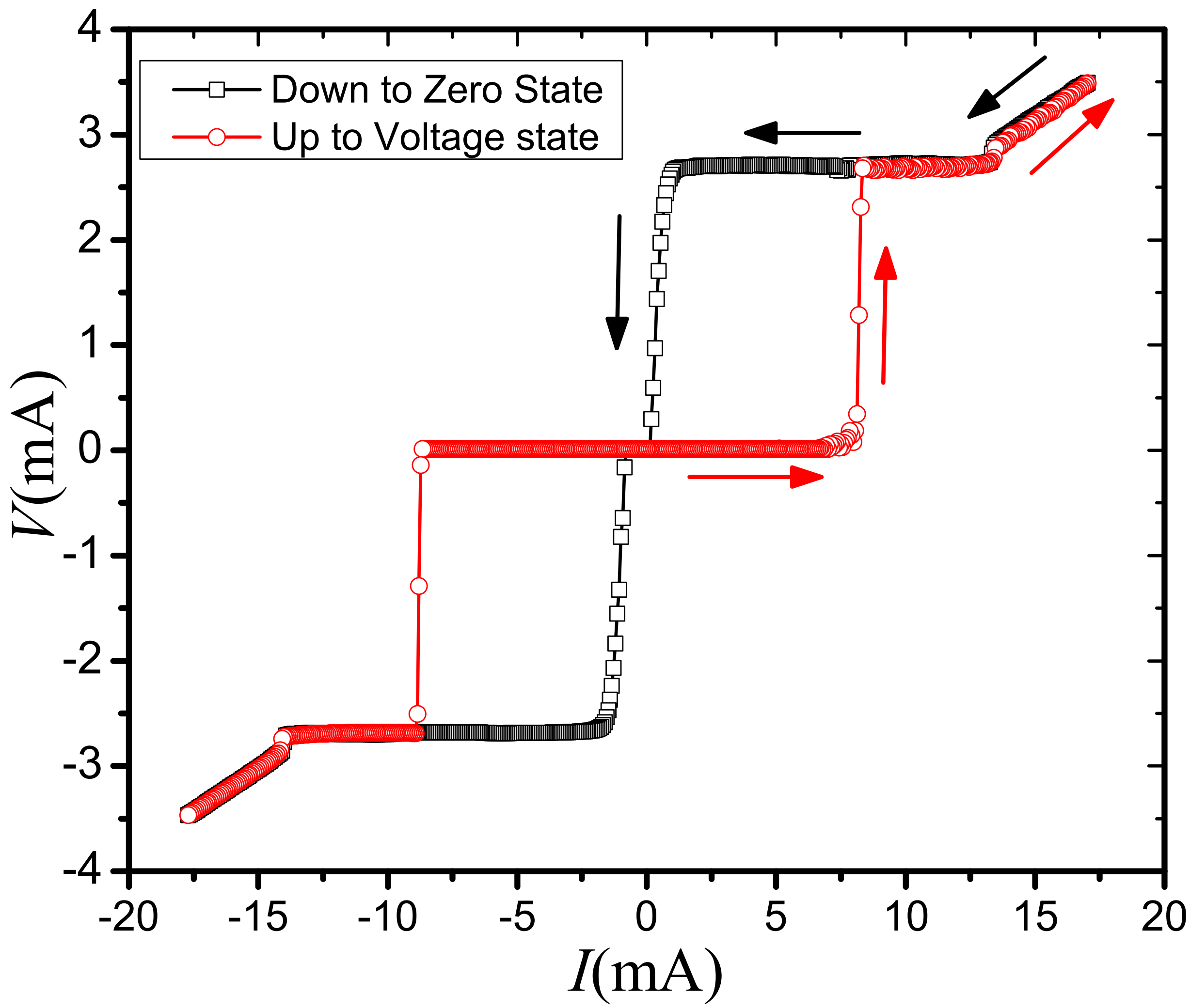

Figure 9.3: I-V curve for Josephson tunnel junction with passively oxidized Al_2O_3 tunnel barrier for sample "ours-2".

requirement that Josephson junction coupling energy should be greater than the thermal energy k_BT, i.e., $I_C > 2ek_BT/\hbar = 0.176\mu A \; at \; 4.2K$. This answered why we only observed resistive I-V characteristics. One comment on our pressure control is that the pressure readings for our samples were not very accurate because our pressure gauge is not well designed for the working region required by us.

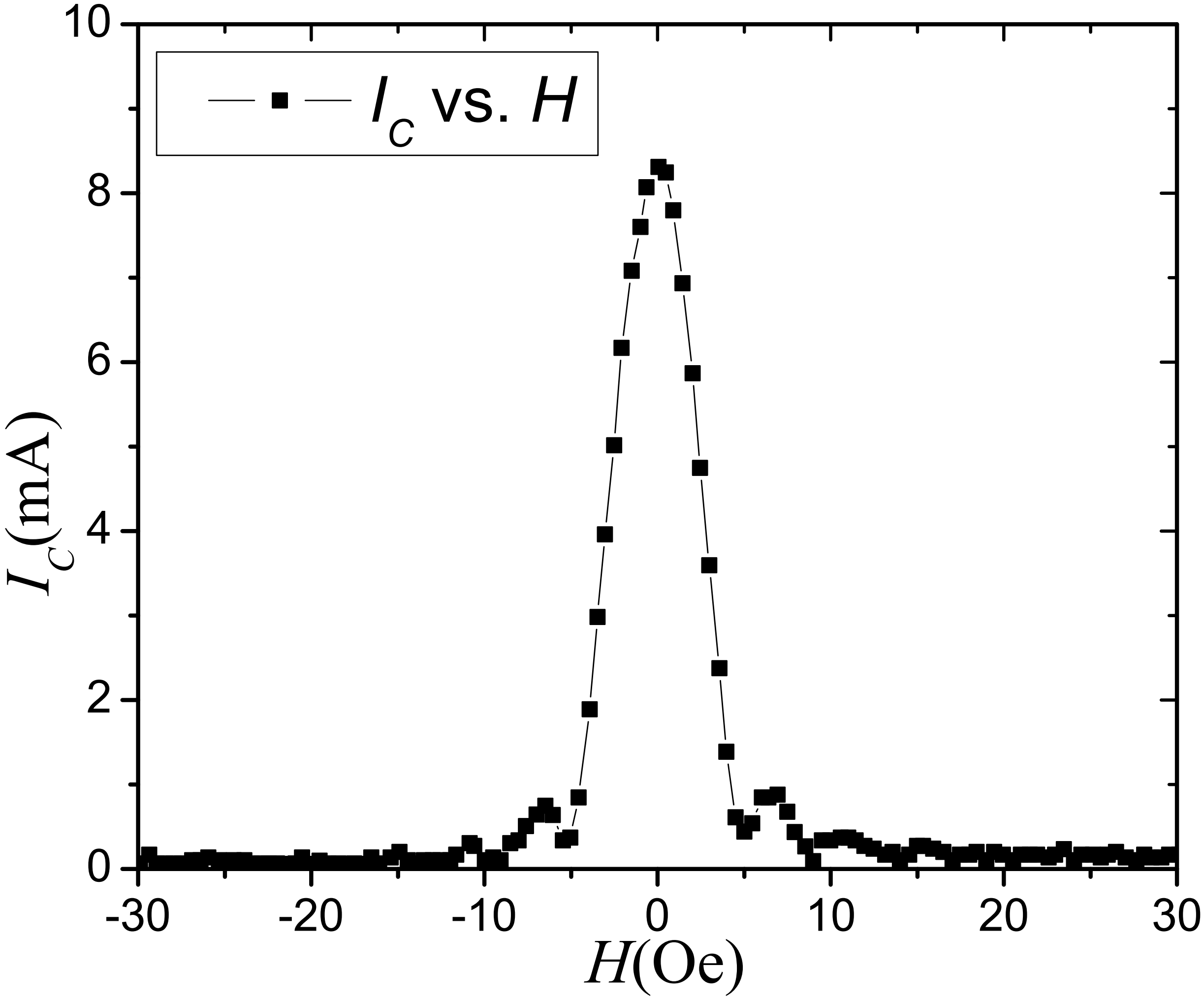

Figure 9.4: Fraunhofer pattern of Josephson tunnel junction with passively oxidized Al_2O_3 tunnel barrier for sample "ours-2".

9.3.2 S/N/S Josephson junctions

After several trials on S/F/I/S junctions, we noticed it might not be the good choice to use the Al_2O_3 tunnel barrier to damp the critical current for our spin-triplet junctions. Therefore, we moved to Josephson junctions with the normal-metal barrier [4]. At the same time we also gained one most obvious advantage by using the normal-metal barrier. That was we never need to worry about the damping problem of Josephson junctions compared with the traditional S/I/S junctions, because the normal barrier provided enough intrinsic shunt making S/N/S junctions nonhysteretic. We applied $Cu_{40}Ti_{60}$ as our normal-metal barrier. We first put down 150nm Nb followed by $Cu_{40}Ti_{60}$. Then we put another 20nm Nb and 10nm Au protection layers on top of the $CuTi$. Finally we finished our usual pillar definition process and the top Nb deposition. As we show in Fig. 9.5 and Fig. 9.6 , we got very good Josephson tunnel junctions. Yet we do not fully understand the center shift of some Fraunhofer patterns as shown in Fig. 9.6.b), even though we found no magnetic impurity in $Cu_{40}Ti_{60}$ target within the detection sensitivity of our EDX .

In order to estimate the normal metal coherence length ξ_n for $Cu_{40}Ti_{60}$ in $J_c = J_{c0}exp(-d/\xi_n)$, we also fabricated some Nb/$Cu_{40}Ti_{60}$/Nb junctions with different CuTi thickness. As we expected, the junction critical current densities decreased exponentially with the increasing thickness of CuTi thickness, as shown in Fig. 9.7. And we also found the coherence length ξ_n for $Cu_{40}Ti_{60}$ is about $3.2nm$. Compared with usual normal metal coherence length, ξ_n for $Cu_{40}Ti_{60}$ is pretty short, which might be due to the spin-orbit scattering from CuTi [30].

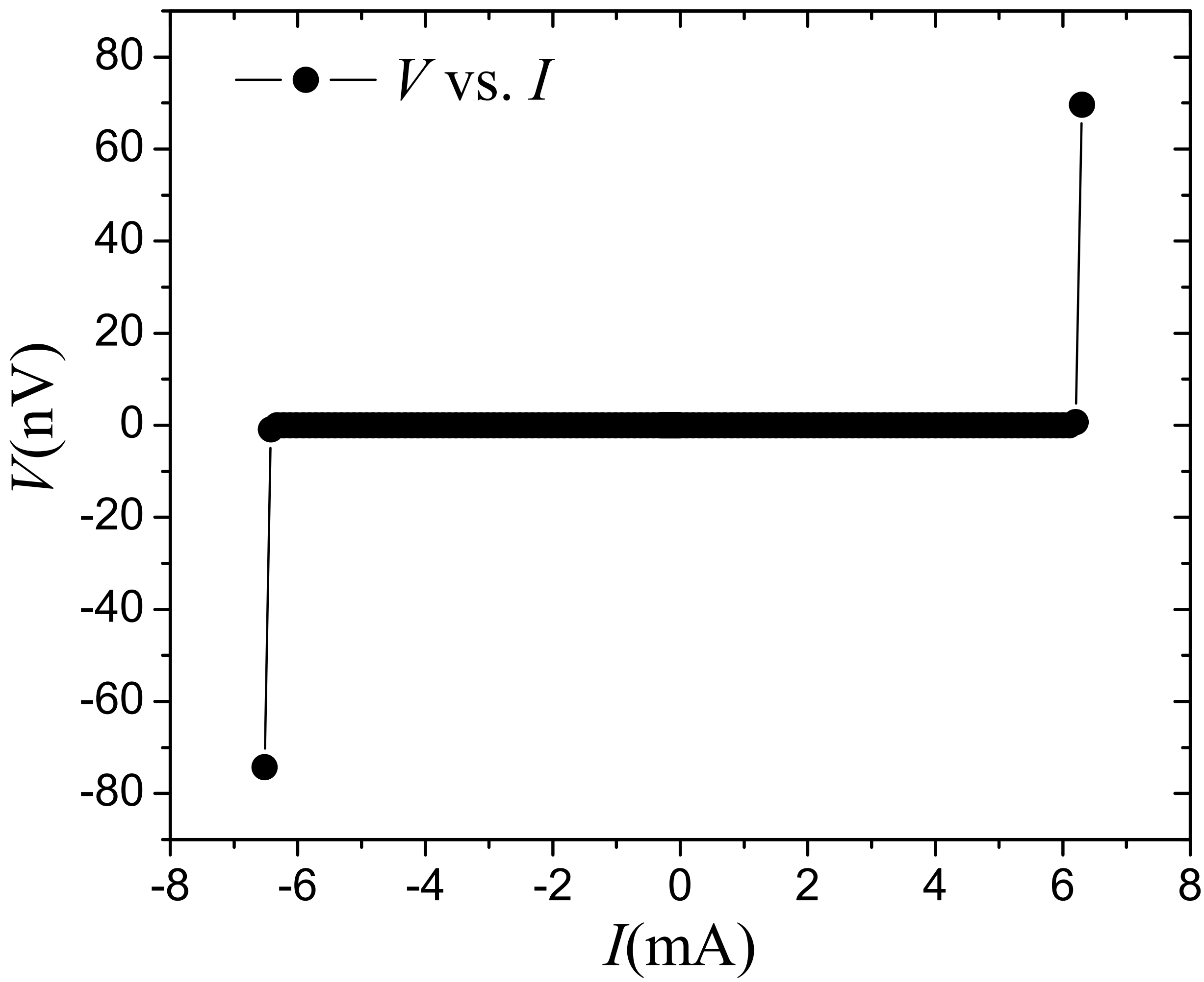

Figure 9.5: current-voltage curve of our Nb/$Cu_{40}Ti_{60}$/Nb Josephson junctions with thickness of $Cu_{40}Ti_{60}$ of 20nm.

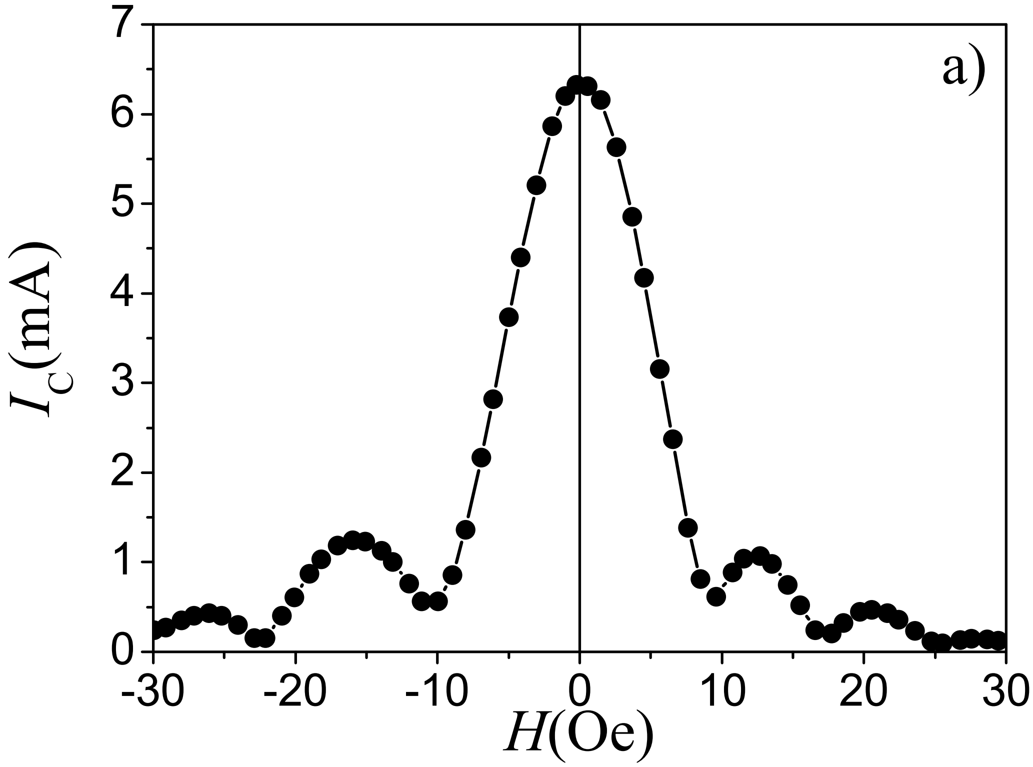

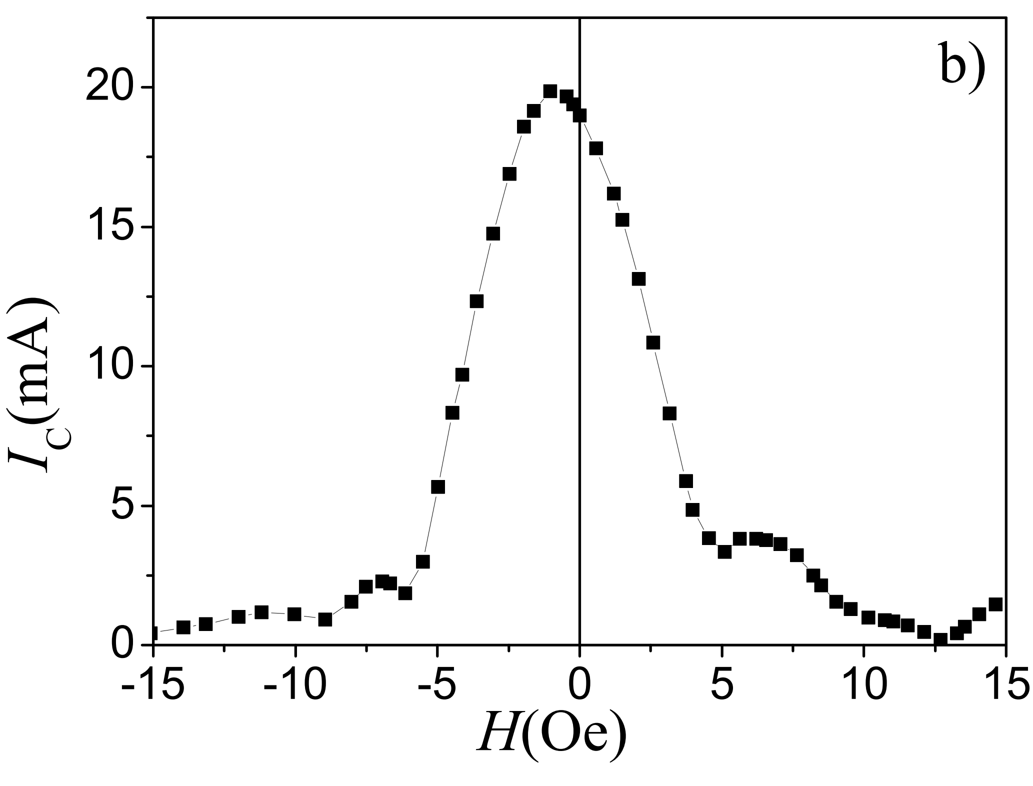

Figure 9.6: Two typical Fraunhofer patterns of Nb/$Cu_{40}Ti_{60}$/Nb Josephson junctions with thickness of $Cu_{40}Ti_{60}$ equal to 20nm.a) 12μm and b)24μm in diameter

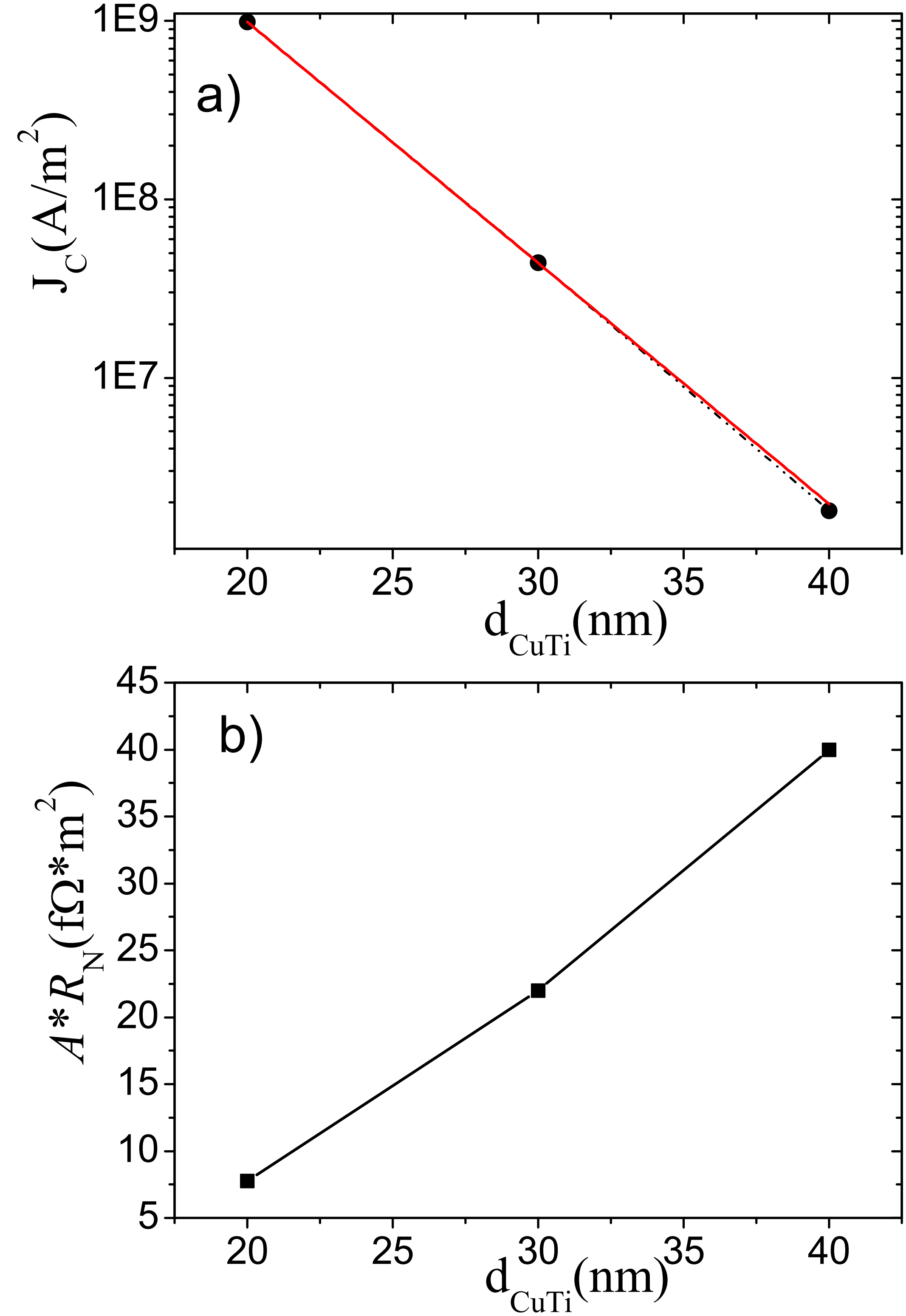

Figure 9.7: a)Junction critical current densities versus $Cu_{40}Ti_{60}$ thickness. The red line is exponential fit by $J_c = J_{c0}exp(-d/\xi_n)$, with $\xi_n = 3.2nm$; b)Product of area and junction resistance versus $Cu_{40}Ti_{60}$ thickness. And a linear fit gives a negative intercept, which we do not understand.

BIBLIOGRAPHY

BIBLIOGRAPHY

[1] P. W. Anderson and J.M. Rowell, Phys. Rev. Lett. **10**, 230 (1963).

[2] M. S. Anwar, F. Czeschka, M. Hesselberth, M. Porcu, and J. Aarts, Phys. Rev. B **82**, 100501 (2010).

[3] Y. Asano, Y. Sawa, Y. Tanaka, and A. A. Golubov, Phys. Rev. B **76**, 224525 (2007).

[4] B. Baek, P. Dresselhaus and S. Benz, IEEE Trans. Appl. Supercon. **16**, 1966 (2006).

[5] J. Bardeen, L. Cooper, and J. Schrieffer, Phys. Rev. **108**, 1175 (1957).

[6] A. Barone and G. Paterno, *Physics and Applications of the Josephson Effect*, John Wiley and Sons, Inc. (1982).

[7] Antonio Barone, *Principles and Applications of Superconducting Quantum Interference Devices* , World Scientific Publishing Company (1992).

[8] F.S. Bergeret, A.F. Volkov, and K.B. Efetov, Phys. Rev. Lett. **86**, 4096 (2001).

[9] F.S. Bergeret, A.F. Volkov, and K.B. Efetov, Phys. Rev. B **68**(6) 064513 (2003).

[10] F.S. Bergeret, A.F. Volkov, K.B. Efetov, Rev. Mod. Phys. **77**, 1321 (2005).

[11] Ya. M. Blanter and F.W.J. Hekking, Phys. Rev. B **69**, 024525 (2004).

[12] Y. Blum, A. Tsukernik, M. Karpovski, and A. Palevski, Phys. Rev. L **89**, 187004 (2002).

[13] K. Boden, W.P. Pratt, Jr., N.O. Birge, Phys. Rev. B **84**, 020510(2011).

[14] L. Bulaevskii, V. Kuzii, and A. Sobyanin, JETP Lett. **25**, 290 (1977).

[15] A. Buzdin , JETP Lett. **35**, 178 (1982).

[16] A. Buzdin , Rev. Mod. Phys. **7**, 935 (2005).

[17] T. Champel, T. Lofwander, and M. Eschrig, Phys. Rev. Lett. **100**, 077003 (2008).

[18] J. Clark, A.I. Braginski *The SQUID Handbook,Vol. 1* , Wiley-VCH, Weinheim (2004).

[19] L.N. Cooper, Phys. Rev. **104**, 1189 (1956).

[20] E.A. Demler, G.B. Arnold, and M.R. Beasley, Phys. Rev. B **55**, 15174 (1997).

[21] Deutscher G. and P.G. de Gennes, *Superconductivity*, edited by R.D. Parks Dekker, New York (1969).

[22] D. Drung, W. Jutzi,IEEE Trans. Magn. **21**, 330 (1985).

[23] M. Eschrig, J. Kopu, J. C. Cuevas, and G. Schön, Phys. Rev. Lett. **90**, 137003 (2003).

[24] M. Eschrig, Tomas Löfwander, Nature Physic **4**, 138 (2008).

[25] Y.V. Fominov, A.F. Volkov, and K.B. Efetov, Phys. Rev. B **75**, 104509 (2007)

[26] E.C. Gingrich, P. Quarterman, Y. Wang, R. Loloee, W. P. Pratt, Jr., N.O. Birge, Phys. Rev. B **86**, 224506(2012).

[27] V.L. Ginzburg and L.D. Landau, Zh. Eksp. Teor. Fiz. **20**, 1064 (1950).

[28] M. Gurvitch, M.A. Washington and H.A. Huggins, Appl. Phys. Lett. **42**, 472 (1983).

[29] W. Heisenberg, Z. Physik **49**, 619 (1928).

[30] B.J. Hickey, D. Greig and M. A. Howson, J. Phys. F:Met. Phys. **16**, L13 (1986).

[31] M. Houzet and A.I. Buzdin, Phys. Rev. B **76**, 060504(R) (2007).

[32] B. Josephson, Phys. Lett. **1**, 251 (1962).

[33] B. Josephson, Rev. Mod. Phys. **46**, 251 (1974).

[34] T.S. Khaire, M.A. Khasawneh, W.P. Pratt Jr. and N.O. Birge, Phys. Rev. Lett. **104**,137002 (2010).

[35] C. Klose, T.S. Khaire, Y. Wang, W.P. Pratt, Jr., N.O. Birge, B.J. McMorran, T.P. Ginley, J.A. Borchers, B.J. Kirby, B.B.Maranville, and J. Unguris, Phys. Rev. Lett. **108**, 127002(2012).

[36] A. Kadigrobov, R.I. Shekhter, and M. Jonson, Europhys. Lett. **54**(3), 394 (2001).

[37] H. Kamerlingh-Onnes, Comm. Phys. Lab. Univ. Leiden, **122** and **124**, (1911).

[38] M. Kemmler, M. Weides, M. Weiler, M. Opel, S.T.B. Goennenwein, A.S. Vasenko, A.A. Golubov, H. Kohlstedt, D. Koelle, R. Kleiner and E. Goldobin, Phys. Rev. B **81**, 054522 (2010).

[39] R.S. Keizer, S.T.B. Goennenwein, T.M. Klapwijk, G. Miao, G. Xiao, and A. Gupta, Nature (London) **439**, 825 (2006).

[40] T.S. Khaire, W.P. Pratt Jr. and N.O. Birge, Phys. Rev. B **79**, 094523 (2009).

[41] M.A. Khasawneh, T.S. Khaire, C. Klose, W.P. Pratt Jr. and N.O. Birge, Supercond. Sci. Technol. **24**, 024005 (2011).

[42] T. Kontos, M. Aprili, J. Lesueur, and X. Grison, Phys. Rev. Lett. **86(2)**, 304 (2001).

[43] D. Kölle, R. Kleiner, F. Ludwig, E. Dantsker and J. Clarke, Rev. Mod. Phys. Rev. Lett. **71**, 631 (1999).

[44] I. Kulik, JETP Lett. **2** 84 (1965).

[45] L. Liebermann, J. Clinton, D.M. Edwards, and J. Mathon, Phys. Rev. Lett. **25**, 232 (1970).

[46] H. London and F. London, Proc. Roy. Sos. (London) A**149**, 71 (1935), Physica **2**, 341 (1935).

[47] W.L. McMillan, Phys. Rev. **175**, 559 (1968).

[48] D.E. McCumber, J. Appl. Phys. **39**, 3113 (1968).

[49] R.E. Miller, W.H. Mallison, A.W. Kleinsasser, K.A. Dellin and E.M. Macedo, Appl. Phys. Lett. **63**, 1423 (1993).

[50] Th. Mühge, N.N. Garif'yanov, Yu.V. Goryunov, G.G. Khaliullin, L.R. Tagirov, K. Westerholt, I.A. Garifullin, and H. Zabel, Phys. Rev. Lett. **77**, 1857 (1996).

[51] Th. Mühge, N.N. Garif'yanov, Yu.V. Goryunov, K. Theis-Bröhl, K. Westerholt, I.A. Garifullin, and H. Zabel, Physica C **296**, 325 (1998).

[52] V. Oboznov, V. Bol'ginov, A. Feofanov, V. Ryazanov, and A. Buzdin, Phys. Rev. Lett. **96**, 197003 (2006).

[53] R. De Bruyn Ouboter et A. Th. A. M. De Waele, Rev. Phys. Appl. (Paris) **5**, 25 (1970).

[54] V. Ryazanov, V. Oboznov, A. Rusanov, A. Veretennikov, A. Golubov, and J. Aarts, Phys. Rev. Lett. **86**, 2427 (2001).

[55] J. Robinson, S. Piano, G. Burnell, C. Bell and M. Blamire, Phys. Rev. Lett. **97**, 177003 (2006).

[56] J. Robinson, S. Piano, G. Burnell, C. Bell, and M. G. Blamire, Phys. Rev. B **76**, 094522 (2007).

[57] J.W.A. Robinson, J.D.S. Witt and M.G. Blamire, Science **329**, 59 (2010).

[58] H. Sellier, C. Baraduc, F. Lefloch and R. Calemczuk , Phys. Rev. B **68**, 054531 (2003).

[59] J.C. Slater, Phys. Rev. **49**, 537,981 (1936).

[60] I. Sosnin, H. Cho, V.T. Petrashov, and A.F. Volkov, Phys. Rev. Lett. **96**, 157002 (2006).

[61] D. Sprungmann, K. Westerholt, H. Zabel, M. Weides and H. Kohlstedt, J. Phys. D: Appl. Phys. **42**, 075005 (2009).

[62] D. Sprungmann, K. Westerholt, H. Zabel, M. Weides and H. Kohlstedt, Phys. Rev. B **82**, 060505 (2010).

[63] W. C. Stewart, Appl. Phys. Lett **12**, 3277 (1968).

[64] E.C. Stoner, Phil. Mag. [7] **15**, 1080 (1933).

[65] C. Strunk, C. Sürgers, U. Paschen, and H. v. Löhneysen, Phys. Rev. B **49**, 4053 (1994).

[66] C.D. Tesche,J. Clarke, J. Low Temp. Phys. **27**, 301(1977).

[67] C. D. Thomas and M. P. Ulmer and J. B. Ketterson, J. Appl. Phys. **(**84) 364(1998).

[68] L. Trifunovic and Z. Radović, Phys. Rev. B **82**, 020505(R) (2010).

[69] Tsang W.-T. and T. Van Duzer, J. Appl. Phys. **46**, 4573 (1975).

[70] A. Volkov, F. Bergeret, and K. Efetov, Phys. Rev. Lett. **90**, 117006 (2003)

[71] A. F. Volkov, A. Anishchanka, and K. B. Efetov, Phys. Rev. B **73**, 104412 (2006).

[72] F. Volkov and K. B. Efetov, Phys. Rev. B **78**, 024519 (2008).

[73] Y. Wang, W.P. Pratt, Jr., N.O. Birge, Phys. Rev. B **85**, 214522(2012).

[74] Y. Wang, W.P. Pratt, Jr., N.O. Birge, J. Phys.: Conf. Ser.**400**, 022131(2012).

[75] M. Weides, K. Tillmann, H. Kohlstedt, Physica C **437-438**, 349 (2006).

[76] P. Weiss, J. Phys. **6**, 661 (1907).

[77] A. Zyuzin and B. Spivak, Phys. Rev. B **61**, 5902 (2000).